Effect of Patient Specific Parameters on Degenerative Shoulder Diseases

THÈSE N^O 6588 (2015)

PRÉSENTÉE LE 30 OCTOBRE 2015
À LA FACULTÉ DES SCIENCES ET TECHNIQUES DE L'INGÉNIEUR
LABORATOIRE DE BIOMÉCANIQUE EN ORTHOPÉDIE EPFL-CHUV-DAL
PROGRAMME DOCTORAL EN MÉCANIQUE

ÉCOLE POLYTECHNIQUE FÉDÉRALE DE LAUSANNE

POUR L'OBTENTION DU GRADE DE DOCTEUR ÈS SCIENCES

PAR

Christoph Anselm ENGELHARDT

acceptée sur proposition du jury:

Prof. I. Botsis, président du jury
Prof. D. Pioletti, Dr A. Terrier, directeurs de thèse
Dr A. Farron, rapporteur
Dr Ph. Müllhaupt, rapporteur
Prof. D. Veeger, rapporteur

EPFL

ÉCOLE POLYTECHNIQUE
FÉDÉRALE DE LAUSANNE

Suisse
2015

Discontent is the first step to progress.

Acknowledgements

In the first place I would like to thank my thesis director Prof. Dominique Pioletti and supervisor Alexandre Terrier for giving me the opportunity to do this PhD project within their laboratory. They were always available for discussions on my work, gave constructive critique and guidance when needed.

I would like to thank the members of my PhD jury Prof. John Botsis, Prof. Dirkjan Veeger, Prof. Alain Farron and Philippe Müllhaupt for undertaking the time consuming effort to examine and evaluate my work.

Of course, this work would not have been possible without the support of many people. First to mention are my parents Rudolf and Maria Engelhardt, who always supported me on my personal and educational pathway by every means possible. Thanks to the motivation given by my older sister Evi Balet and my friends Philip Lenz and Christopher Hauke, I applied at the doctoral school at EPFL. At the LBO, I want to especially thank my desk neighbours Xabier Larrea, Valérie Parvex and Valérie Malfroy Camine for sharing all the ups and downs of daily PhD life. I would like to further thank the shoulder team in the clapier, Patricia Scheuber, Julien Ston and Antoine Dewarrat for constructive discussion and a great working atmosphere. Further thanks go to Caroline Fernandes Sieger for the after lunch walks, which always were a great source of inspiration.

In the context of musculoskeletal modelling, I want to thank David Ingram for his great commitment to the project and for giving me insight into modelling techniques.

Joël Cugnoni gave me great support in the field of continuum mechanics and finite element methods. Thanks a lot for the motivating meetings. Further I would like to thank Arne Vogel for his introduction to subroutine development, which eased my first steps in Fortran programming.

The experimental data provided in this work could not have been produced without the volunteers for MRI scans Xabier Larrea, Julien Ston, Adeliya Latypova and Ulrike Kettenberger. Medical advice and support for these measurements from Fabio Becce, Jean Baptiste Ledoux and Nicolas Place was worth gold.

I am more than happy that I was accompanied during the last year of my PhD by my girlfriend Christina Steinbach. She gave me all the support she could, even when that meant to leave me alone. She further gives me a clear perspective for my future plans.

Lausanne, 2015   C. E.

i

Abstract

Osteoarthritis and rotator cuff tears are two common and wide spread shoulder diseases leading to significant restrictions in the daily life of the affected. The pathogenesis is not fully understood yet. A chronic process triggered by multiple causes is assumed including inflammation, metabolic disturbances, and mechanical contributions. Several studies described as mechanical cause a statistically important impact of the scapula shape. The appearance of osteoarthritis and rotator cuff tears could be linked with specific anatomic parameters. The aim of this thesis was to improve the understanding of the mechanical contribution to the development of osteoarthritis and rotator cuff tears by the means of computational modelling.

In this work, we focused on the lateral extension of the acromion and the glenoid inclination. Three numerical shoulder models were developed to analyse these two parameters. A musculoskeletal model was used to evaluate muscle and joint reaction forces acting on the glenohumeral joint. The underlying algorithm calculated joint torques for a given movement based on an inverse dynamics approach and solved the undetermined problem of muscle coordination with a nullspace optimization routine. The calculated joint forces were then used as input for a finite element cartilage model. Cartilage was modelled as incompressible hyperelastic material characterized with experimental data. The model provided values for cartilage strain and humeral head translations. The humeral head translation and supraspinatus force were used in a third model of the supraspinatus tendon. The constitutive equations for tendon tissue were derived from an anisotropic hyperelastic strain energy potential. Material parameters were identified in both fibre direction and the transverse plane. The elasticity tensor was approximated using a forward differentiation algorithm. Using the finite element method, tendon strains and tendon impingement were evaluated. The biomechanical variables cartilage strain, subacromial space, and tendon strain were analysed for different anatomic configurations. All models were validated with available clinical data.

The biomechanical variables were more sensitive to changes of the acromion length than to changes of the glenoid inclination. The numerical study could explain the statistical association for osteoarthritis for short acromion by an increase in cartilage strains. A long acromion increased superior humeral head translation, which is associated to tendon impingement and related tears. We also observed increasing tendon strains close to the tendon insertion for a short acromion. Clinical studies did not correlate tendon tears to a short acromion. However, the clinical studies did not distinguish between the different types of tendon tears. At this point, further clinical studies would be necessary to clarify the numerical results. A better understanding about physiologic anatomic parameters could help to improve the treatment

Abstract

of osteoarthritis and rotator cuff tears. Prosthesis design and positioning during total shoulder arthroplasty, tendon repair techniques, and conservative treatment could be improved to compensate negative effects of excessive anatomic parameters.

Keywords: Osteoarthritis, Rotator Cuff, Anatomic Parameters, Numerical Shoulder Model

Zusammenfassung

Osteoathrose und Rupturen der Rotatorenmanschette sind häufig auftretende Erkrankungen der Schulter, die zu beträchtlichen Einschränkungen im alltäglichen Leben der Betroffenen führen. Die Pathogenese beider Krankheitsbilder ist bis heute nicht vollständig geklärt. Es wird vermutet, dass ein multikausaler chronischer Prozess, der neben Entzündungen und Stoffwechselstörungen auch von biomechanischen Faktoren ausgelöst werden kann, die Ursache ist. In diesem Zusammenhang beschrieben mehrere Studien die Rolle der Form des Schulterblattes als möglichen biomechanischen Faktor. Das Auftreten von Osteoathrose und Rupturen der Supraspinatussehne konnte mit anatomischen Parametern korreliert werden. Das Ziel dieser Dissertation war es, den mechanischen Einfluss auf die Entstehung von Osteoathrose und Rupturen der Rotatorenmanschette besser zu verstehen und mit numerischen Schultermodellen genauer zu untersuchen.

Um den Einfluss von Acromium Länge und Glenoid Inklination auf die Biomechanik der Schulter zu untersuchen, wurden drei numerische Schultermodelle entwickelt. Mit Hilfe eines muskuloskeletalen Modells konnten Muskel- und Gelenkkräfte berechnet werden. Der verwendete Algorithmus ermittelte die Gelenksmomente mit Hilfe des Ansatzes der inversen Dynamik und löste anschliessend das Problem der Muskelkoordination durch eine Nullspace Optimierung. Das muskuloskeletale Modell erlaubte es die Kräfte in Abhängigkeit der anatomischen Parameter zu ermitteln. Die erhaltenen Gelenkskräfte wurden in einem Finite Elemente Modell des glenohumeralen Knorpels verwendet. Der Knorpel wurde als inkompressibles hyperelastisches Material simuliert, charakterisiert mit experimentellen Daten. Die Knorpeldeformierung und die Verschiebung des Humeruskopfes wurden berechnet. In einem dritten Modell wurden die Supraspinatus Kräfte und die Bewegung des Humeruskopfes verwendet um Belastungen in der Supraspinatussehne zu analysieren. Die konstitutiven Gleichungen um das Materialverhalten der Sehne zu beschreiben wurden von einem hyperelastischen anisotropen Formänderungsenergiepotentials abgeleitet. Die Materialparameter wurden sowohl in Faserrichtung als auch in der transversen Ebene mit Hilfe experimenteller Daten identifiziert. Der Elastizitätstensor wurde approximiert basierend auf einem finite Differenzen Algorithmus. Mit Hilfe der finiten Elemente Methode wurde Sehnenverzerrungen berechnet und ein eventueller Kontakt zwischen Sehne und Acromium. Die biomechanischen Variablen Knorpeldehnung, subacromialer Raum und Sehnendehnung wurden für verschiedene anatomische Konfigurationen berechnet. Alle numerischen Modelle wurden mit verfügbaren experimentellen Daten validiert.

Zusammenfassung

Die biomechanischen Variablen reagierten sensibler auf Änderungen der Acromiumlänge als auf Änderungen der Glenoidinklination. Der statistische Zusammenhang zwischen Osteoarthrose und kurzem Acromium, konnte durch erhöhte Knorpelbelastungen erklärt werden. Ein langes Acromium ergab erhöhte superiore Humerus Translationen, was mit dem Impingement-Syndrom und entsprechenden Rupturen der Supraspinatussehne einhergehen kann. Allerdings erhöhte sich die Sehnenbelastung im Falle einen kurzen Acromiums. Klinische Studien berichteten bisher nicht über statistische Korrelationen zwischen kurzem Acromium und Rupturen der Supraspinatussehne. Jedoch unterschieden die vorliegenden Studien nicht zwischen den verschiedenen Typen von Sehnenrupturen. An dieser Stelle wären weitere klinische Studien notwendig, um die numerischen Ergebnisse zu erklären. Bessere Kenntnisse über den Einfluss von biomechanischen Faktoren bzw. physiologischen Knochengeometrien könnten in Zukunft helfen Therapien für Osteoathrose und Rupturen der Rotatorenmanschette zu verbessern. Prothesen Design, Prothesen Positionierung bei Atroplastien, Sehnenreparatur Techniken und konservative Behandlungsmethoden könnten gezielt eingesetzt werden um den schädigenden Einfluss von auffälligen Knochengeometrien zu minimieren.

Stichwörter: Osteoathrose, Supraspinatus Ruptur, Anatomische Parameter, Schultermodell

Résumé

L'arthrose et la déchirure de la coiffe des rotateurs sont deux pathologies fréquentes de l'épaule, qui conduisent à des limitations significatives dans la vie quotidienne des affectés. La genèse de ces pathologies n'est pas encore comprise mais l'on considère généralement qu'il s'agit d'un processus chronique aux causes multiples. En effet, aux côté de l'inflammation et du métabolisme, la biomécanique de l'articulation pourrait jouer un rôle. Plusieurs études ont décrit l'influence de la morphologie de la scapula sur l'apparition de l'arthrose et la déchirure de la coiffe des rotateurs à l'aide de paramètres anatomiques. L'objectif de cette thèse était de proposer une explication mécanique pour ces observations avec une étude biomécanique numérique.

Dans ce travail, le focus était sur l'effet de la longeur de l'acromion et l'inclinaison de la glène. Trois modèles numériques de l'épaule ont été développées pour analyser ces deux paramètres. Un modèle musculo-squelettique a été utilisé pour évaluer les forces musculaires ainsi que les forces de réaction dans l'articulation. L'algorithme sous-jacent utilisait une approche de dynamique inverse pour calculer les moments de force dans l'articulation pour un mouvement donné, puis résolvait le problème indéterminé de la coordination musculaire à l'aide d'une optimisation du nullspace. Ce modèle musculo-squelettique pouvait de plus s'adapter aux différents paramètres anatomiques. Les forces dans l'articulation obtenues à l'aide de ce modèle ont ensuite été introduites dans un modèle à éléments finis du cartilage. Le cartilage a été modélisé avec une loi constitutive hyperelastique et incompressible characterisé à l'aide de données expérimentales. Le modèle calculait la déformation du cartilage et les translations de la tête humérale. Enfin, les translations de la tête humérale, ainsi que la force dans le supraspinatus obtenue avec le modèle musculo-squelettique, ont été utilisées dans un troisième modèle du tendon du supraspinatus. Les équations constitutives ont été dérivées depuis un potentiel d'énergie de déformation anisotrope et hyperélastique. Les paramètres des matériaux ont été identifiés dans la direction de fibre et le plan transverse avec des données expérimentales. Le tenseur d'élasticité a été approximé avec un algorithme basé sur des différences finies. Le modèle du tendon a permis de calculer la déformation du tendon et évaluer le conflit sous-acromial. Les variables biomécaniques déformation du cartilage, espaces sous-acromiale et la déformation du tendon ont été analysés pour des configurations anatomiques différents. Les modèles ont été validé avec des données cliniques à disposition.

Les variables biomécaniques étaient plus sensibles au changement de la longeur de l'acromion qu' au changement de l'inclinaison de la glène. Les résultats pourraient expliquer le risque accru d'arthrose pour les acromions courts par une augmentation de la déformation du

Résumé

cartilage. Un acromion long a pour conséquence une translation supérieur de la tête humerale, qui est associé avec un conflit sous-acromial et des déchirures associées. En revanche, on a également observé une augmentation de la déformation du tendon pour un acromion court. Les études cliniques n'ont pas reporté de déchirure pour un acromion court. Par contre, ces études ne faisaient pas la distinction entre les différentes types de déchirure. Des études complémentaires seront donc nécessaires pour clarifier ces résultats numériques. La connaissance de ces paramètres physiologiques géométriques pourrait aider à améliorer les traitements de l'athrose et des déchirures de la coiffe des rotateurs. Le design et le positionnement des prothèses lors des arthroplasties, des techniques de réparation du tendon, et les traitements conservateurs pourraient être modifiés pour compenser les effets négatifs de paramètres anatomiques anormaux.

Mots clefs : osteoarthritis, déchirure de la coiffe, paramètres anatomiques, modèle de l'epaule

Contents

Contents

List of Figures

List of Tables

1 Introduction

1.1 Research Context

The musculoskeletal system is probably the element of our body, with which we identify ourself the most. It gives shape to our body with bones determining height and stature, and muscles contouring the skin. It provides a protective structure and a supporting framework for our vital organs with a series of specially shaped bones and connective tissues. It allows body motion with articulations flexibly connecting bones through ligaments and cartilages. Muscles and their tendons spanning these joints allow us to actively interact with our environment. This gives us the impression of control over our body while most other systems in the body work self-dependently and beyond our control.

The upper limb is the part of the musculoskeletal system, where our mental focus usually lies. The hand, the grasping organ of humans and their primate relatives, plays a key role in our interaction with our environment. Some scientists even assume, the upper limb had a key role in the development of modern human beings, after it was freed for other tasks than locomotion through a bipedal posture. The upper limb participates in almost all works effected with bare hands or any kind of tools. It is also an important communication channel starting from simple pointing to gestures or even complex sign languages. In our modern society, all interaction with machines, electronic devices and telecommunication passes through interfaces designed for the use by hands.

The any time available flawless operation of the upper limb is important in our daily lives. Any kind of dysfunction of the upper limb leads immediately to great limitations and loss of quality of life. Like all systems in the human body, the musculoskeletal is also affected by debilitating diseases with symptoms ranging from light discomfort to functional failure. All components are affected by their specific pathologies, often influencing each other or even triggered by other metabolic or neurological dysfunctions in the body. For the upper limb, it is the shoulder which is the most often affected by pain and mobility restrictions. Musculoskeletal shoulder disorders are the third most common cause for orthopaedic consultation in primary care [Mitchell et al. 2005] with a lifetime prevalence up to 70 % increasing for the elderly

population [Luime et al. 2004]. Despite the frequent occurrence, the pathogenesis of the common shoulder conditions are widely unknown. Research in this field motivated by social, economic, and medical factors covers amongst others physiological, metabolic, as well as biomechanical factors on which this work will focus on.

From a mechanical point of view, the active stabilization by the rotator cuff muscles is the shoulder's unique characteristic. In contrast to other joints, the shoulder joint is not guided nor hold by an embracing bony joint socket or pre-stressed ligaments. This allows on the one hand a great range of motion, but requires an accurate interplay of all muscles and a simultaneous motion of all segments of the shoulder girdle on the other hand to provide sufficient stability [Veeger and van der Helm 2007]. The compromise between mobility and stability leads to a number of special shoulder disorders that can not be observed in other joints: the inborn instability increases the risk of injury, which can trigger further degenerative processes. In case of the shoulder joint, the two leading degenerative diseases are osteoarthritis and rotator cuff tears.

Osteoarthritis is the degeneration and loss of articular cartilage, in case of the shoulder on the glenoid cavity or the humeral head, until bone gets exposed and damaged in advanced irreparable states [Vincent 2004]. Beside inflammatory processes that alter cartilage tissue properties, frequent overloading is supposed to trigger the cartilage degeneration. Such increased pressures can occur when the compressive force in the articulation reaches un-physiological values, or when the contact area between humeral head and glenoid cavity is reduced for example during excessive humeral head translations. At the same time, mini-mizing activities and rest seem to be as harmful for the cartilaginous tissues: they do not contain blood vessels and rely on nutrient supply from the joint fluid through diffusion. The repetitive compression of the spongy cartilage at every movement provides this essential fluid exchange. Further, cartilage seems to possess its own repair mechanism, that need mechanical stimulation for its activation. A key point in osteoarthritis research is consequently the right dosage of cartilage loading to maintain health without wearing out the articular surfaces [Eyre 2004, Buckwalter and Martin 2006, Helmick et al. 2008, Egloff et al. 2012]. The reasons why unphysiological over or under loading of the shoulder joint occurs remain unknown.

Rotator cuff tears usually start in the supraspinatus tendon with a fraying of the intact tendon close to its insertion on the humeral head. Symptomatic or asymptomatic in initial states, the tear usually increases over time accompanied by arising or worsening symptoms until the tear goes through and through [Tempelhof et al. 1999]. Again besides inflammatory processes, repeated overloading of the tendon by overhead movements, throwing or weightlifting is supposed to initiate the degenerative process. The repetitive overloading might cause micro trauma that then release inflammatory mediators, which locally alter the material properties of the tissue [Nho et al. 2008].

For both scenarios, osteoarthritis and rotator cuff tears, causal therapies are not available yet. Orthopaedics and physiotherapists are restricted to symptomatic treatments to reduce pain

and preserve mobility. To develop causal treatments, a deep understanding of the underlying pathological process and its triggers is necessary. This is in the case of musculoskeletal disorders a complicated task: it is difficult to access the affected joint without invasive effort. In the case of osteoarthritis, it is difficult to observe the degeneration. We can only state the degeneration in an already affected joint by medical imaging or when opening the joint during surgery. Although it is well accepted in recent research, that joint load plays a key role, we can only suppose afterwards if the trigger has been excessive or inadequate cartilage loading. With the technical means we have at disposal today, it is still not possible to measure loads in a healthy joint in vivo. The same reasoning applies for rotator cuff tendon tears: we can only state the tearing during examinations and assume the causes, but it is not possible in practice to observe the pathological process. As we can not measure muscle forces in vivo, the overloading of the tendon remains one hypothesis beside others.

One approach to fill the gap between shoulder disorders and unknown mechanical causes is the usage of joint models. First models appeared in the 19th century, when scientists built marionette like models of human joints using wooden bones spanned by cables representing the muscles [Mollier 1899, Shiino 1913]. With the invention of computers and the continuous increase in computing power, more and more numerical models of human articulations came up [Prinold et al. 2013]. Today these models play an important role in the analysis of musculoskeletal systems and related disorders. The existing models can be classified into two categories: First, the musculoskeletal models which are used for kinematic analysis and muscle force estimation. They usually consist of rigid bones connected by spherical joints spanned by varying number of muscles. This kind of models can cover single joints up to the whole human skeleton. The second type of models focuses on tissue deformation or damage under loadings. In the context of articular biomechanics the tissues of interest are bone, cartilage, ligaments, tendons, and muscles. The model must thus include a constitutive law for the tissue of interest. The stress distribution inside the tissue can be computed with the finite element method. The key problem of all models, physical or numerical, is the validation of the obtained results. As quoted previously, the estimated quantities can usually not be directly measured. If a direct measurement is possible, the results are usually patient specific and might not be applicable in general. A validation strategy can be to develop patient specific models that can be validated with corresponding patient specific experimental data. When working with generic models, validation can be achieved with statistically significant experimental data, which requires multiple repetitions and accordingly large sample sizes. Both approaches are costly and time consuming. The validation process should further be seen as an ongoing process: numerical results should always be tested against new experimental and clinical findings.

In this work, numerical modelling will be used to analyse recent clinical observations. It was observed that the individual anatomy of the shoulder bones is statistically linked to the appearance of degenerative shoulder diseases. The lateral extension of the acromion and the glenoid inclination have shown to play an important role in the individual tendency of developing osteoarthritis or rotator cuff tears in the glenohumeral joint [Hughes et al. 2003, Nyffeler et al. 2006, Moor et al. 2013]. However, the cited studies have only an observatory

character. The work presented here aims to analyse the suggested link between patient-specific anatomic characteristics and the appearance of degenerative shoulder disorders from a biomechanical point of view. To do this, three numerical models of the upper limb were developed to analyse the influence of patient-specific parameters on muscle and joint reaction forces, cartilage strains, and supraspinatus tendon strains.

1.2   State of the Art

The section provides an overview of existing scientific studies that are related to this thesis. The first section will briefly introduce the human shoulder from an anatomical point of view without any claim to completeness. Only the important aspects for the understanding of this work will be introduced, taken, if not marked otherwise, from Gray [2000], Schünke et al. [2007], and Netter [2015]. The second and third section will introduce the reader to the two most common orthopaedic shoulder conditions, glenohumeral osteoarthritis and rotator cuff tears. Then, an overview of numerical shoulder models is given before concluding the chapter with the presentation of the thesis goals.

1.2.1   Human Shoulder

The human shoulder is referred to as the complex formed by the three bones clavicle, scapula and humerus (Figure 1.1), their connecting articulations (Figure 1.1), and the spanning muscles (Figure 1.2, Figure 1.3).

The clavicle is a S-curved long bone. It is positioned between the superior end of the sternum and the acromion of the scapula passing over the first rib, where it can clearly be seen by the bulge it creates on the skin. On the medial side, the clavicle is attached to the sternum through the sternoclavicular joint, a freely movable synovial articulation. On the lateral side, the scapula is attached through the acromioclavicular joint, which allows the scapula to slide on the thoracic wall. The bone acts like a cross beam, that attaches the upper limb to the thorax and transmits impacts from the arm to the trunk skeleton. Its length and shape determine the shoulder-width of a person and the position of the shoulder blade. It further covers and protects the nerve cord that supplies the arm.

The scapula is flat triangular shaped bone positioned posterolaterally on the rib cage. On the lateral tip of the triangle, a flat socket can be spotted: the glenoid cavity. This structure is the articular support for the humerus on the scapula. It forms the glenohumeral joint with the humeral head. The glenoid cavity is encompassed by two bony processes: the acromion and the coracoid process. The acromion forms the summit of the shoulder. At the lateral side, it is a L-shaped flat structure that overhangs the glenoid cavity on the posterior-superior side. The coracoid process is a similar L-shaped structure on the anterior-superior side of the glenoid cavity. Both processes provide attachment sites for muscles spanning from the trunk to the scapula or from the scapula to the humerus.
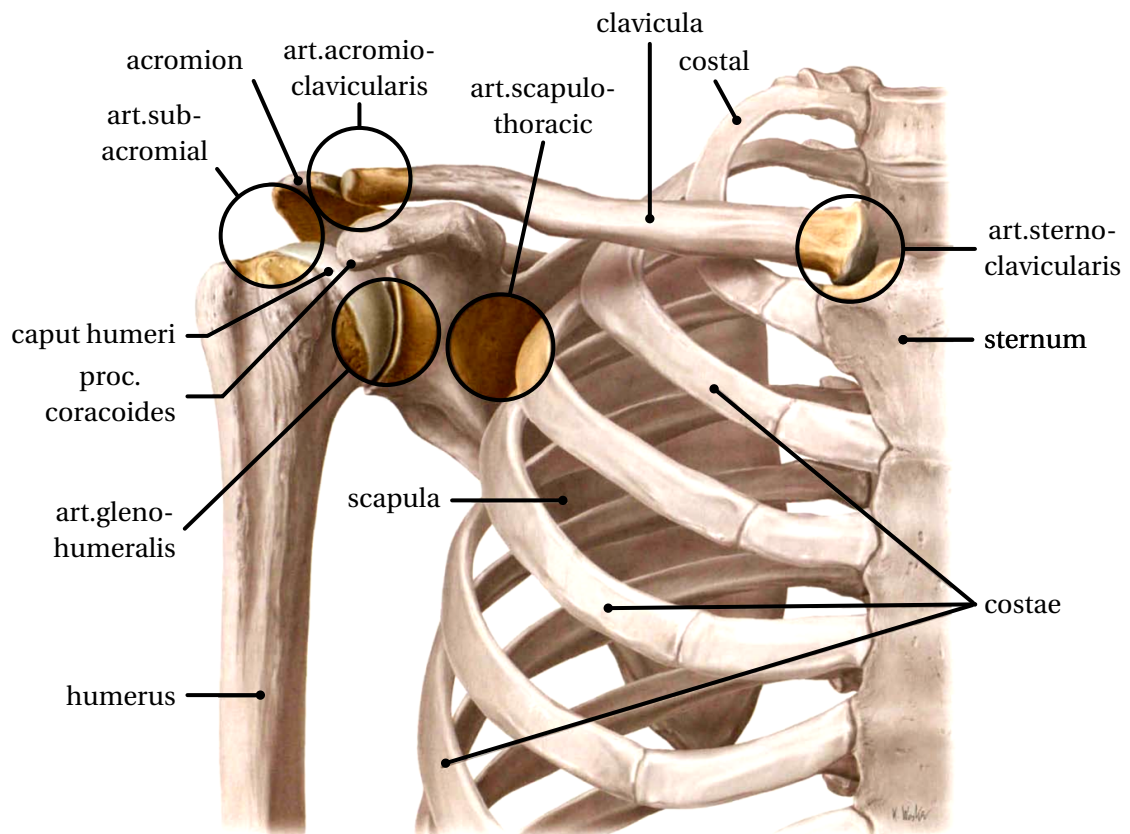
Figure 1.1 – Illustration of the upper limb skeleton including the three bones forming the shoulder: clavicle, scapula, and humerus [Schünke et al. 2007].

The humerus forms the bony foundation of the upper arm. It is a long bone connecting the shoulder blade with the forearm bones radius and ulna. On its superior end, it consists of a rounded almost spherical head and two short processes, called tubercles, which provide attachment sites for the rotator cuff muscles. In the middle part, the bone is cylindrical turning into a more prismatic cross section on its inferior end. There it forms the radial and coronoid fossa, which receive the medial ends of ulna and radius to form the elbow joint.

The articulations between the presented bones are the shoulder joints. When referring to "the" shoulder joint, the glenohumeral joint is usually meant. It establishes the contact between humerus and scapula (Figure 1.1). The spherical humeral head surface is in contact with the oval glenoid cavity. The glenoid cavity has a flat concave shape, slimmer at the cranial side and broader at the caudal side. On average the glenoid cavity is retroverted by 7.4°. In the sagital plane, the glenoid cavity measures 25 mm, in the frontal plane 35 mm. The contact surface with the humeral head is covered with a cartilage layer of approximately 4 mm thickness. Compared to the humeral head, the contact surface on the glenoid is much smaller and less curved: only 25 to 30 % of the humeral head cartilage surface is in contact with the glenoid cartilage in any position of the arm [Murray et al. 2013]. The joint socket does not enclose

the joint head. This setting allows on the one hand a great range of motion, but requires on the other hand further physical structures for guidance and stabilization of the glenohumeral joint. The scapula floating on the thorax further extends the range of motion to more than 60% of a sphere [Engin and Chen 1986]. Additional the humerus can be axially rotated at any position. The full working area of the hand is determined by adding elbow flexion and forearm pronation.

The glenohumeral joint is enveloped with a surrounding joint capsule. The capsule contains several fibrous structures from which several ligaments arise: the coracohumeral ligament, superior, inferior, and middle ligaments. All ligaments are considered with stabilizing functions. To perform the stabilizing task, passive structures need to be stretched beyond their rest length. Loose at the arm's rest position, the ligaments and capsule only exert forces at extreme arm rotations or humeral head translations larger than 5 mm [Blasier et al. 1997, Veeger and van der Helm 2007, Massimini et al. 2012]. The contribution to midrange stability is thus considered to be small. This consideration is further encouraged by the fact, that the passive structures can not prevent joint dislocation [Yu 2004].

The stabilization of the glenohumeral joint must thus happen through active muscular control. The predestined group of muscles is the rotator cuff (Figure 1.2) consisting of subscapularis, supraspinatus, infraspinatus and teres minor. The subscapularis is situated between scapula and thorax, spanning from the scapula's margo medialis to the minor tubercle on the humeral head. The supraspinatus lies in the scapula fossa and inserts on the anterior edge of the greater tubercle on the humeral head. Infraspinatus is positioned on the lateral side of the scapula spanning from the margo medialis to the posterior edge of the greater tubercle on the humeral head. Teres minor lies below the infraspinatus muscle with its origin on the margo lateralis and its insertion below the greater tubercle. At the insertional end of the muscles, there are short tendons wrapping around the humeral head before they merge with the joint capsule and insert onto the bony structure [Matava et al. 2005]. The positioning of the rotator cuff muscle allows effectively to redirect the glenohumeral joint reaction force onto the glenoid cavity: their half circle arrangement around the glenoid cavity combined with small moment arms pulls the humeral head into the glenoid cavity without exerting large contra productive moments [Veeger and van der Helm 2007]. Active control requires beside the actors some kind of feedback system. Although some studies report the existence of enervation and receptors in ligaments, capsule, and laprum that might perform this task, the nerval control of the glenohumeral stabilization is still controversial. Despite the stabilizing function, the rotator cuff muscle also contribute to abduction, internal and external rotation of the shoulder.

In contrast to the rotator cuff, the other muscles spanning the glenohumeral joint have rather large moment arms. The great range of motion of the glenohumeral joint combined with the large moment arms require large shortening ranges [Veeger and van der Helm 2007]. Anatomic studies reported much longer fascicle length for the shoulder muscles compared to the lower limb [Langenderfer et al. 2004]. This architecture guarantees a long active force trajectory to
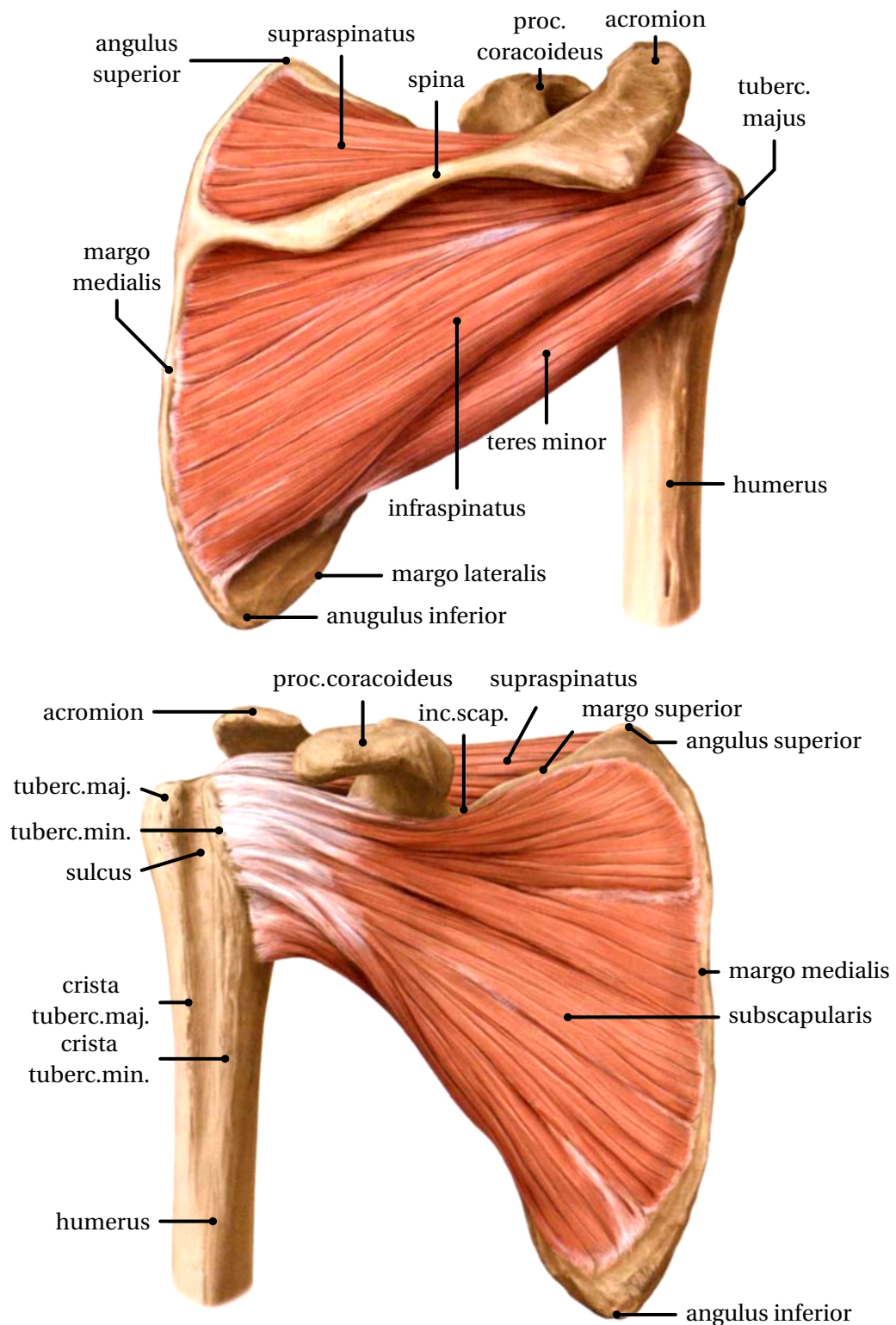
Figure 1.2 – Stabilisers of the shoulder: the rotator cuff muscles. Posterior (top) and anterior (bottom) view [Schünke et al. 2007].

cover the full motion range of the shoulder and contributes to better muscular endurance [Breteler et al. 1999].

The largest shoulder muscle is the deltoid muscle (Figure 1.3). It enrols around the glenohumeral joint and gives the shoulder its rounded contour. The muscles consists of three distinguishable bundles, that are named after their relative position (or origin site): anterior deltoid (clavicular deltoid), middle deltoid (acromial deltoid), and posterior deltoid (spinal deltoid). From this broad attachment, the deltoid converges to a narrow insertion site on the lateral aspect of the humeral shaft. The deltoid's main function is to elevate the arm during abduction movements in the frontal plane. It was also found to play an important role in the precise and rapid positioning of the glenohumeral joint during arm and hand manipulation [Potau et al. 2009]. Due to the wrapping of the deltoid around the humeral head, it also contributes to the stabilisation of the glenohumeral joint.

1.2.2 Glenohumeral Osteoarthritis

Also known as degenerative joint disease, osteoarthritis leads to an abnormal degradation of articular cartilage and subchondral bone. The diagnosis for osteoarthritis is based on the clinical symptoms of sharp or burning pain, and loss of mobility in the affected joint. The suspected diagnosis can be confirmed on medical imaging, where a narrowing of the joint space can be observed. In advanced stages of this non-inflammatory process, one can further observe the destruction of the cartilage layers, wear patterns, subchondral bone sclerosis and the presence of osteophytes (Figure 1.4) [Buckwalter and Martin 2006].

The causes for this debilitating disease are often unknown, and is referred to as primary osteoarthritis. It can also appear as a (long-term) consequence of injuries or infections, or as a secondary effect of hereditary, inflammatory, metabolic, or neurological diseases, which is referred to as secondary osteoarthritis [Buckwalter and Martin 2006].

In both cases, the disease is supposed to originate from a dysbalance in the joint's homeostasis: the joint's natural repair mechanisms can not keep up with the occurring joint wear [Brandt et al. 2009, Egloff et al. 2012]. The conclusion that joint overuse is a main cause for osteoarthritis suggests itself and is supported by several studies, which accredit a higher osteoarthritis risk to workers with physically demanding tasks and athletes with joint exposure to impacts or torsional loads [Buckwalter and Martin 2006]. Surprisingly, the degree of activity is not the major risk factor for osteoarthritis from a statistical point of view but age. A second self-evident conclusion, that osteoarthritis is the normal wear and tear of ageing, can however not stand to critical examination. This would favour a sedentary lifestyle as prevention for osteoarthritis, but such a lifestyle has shown to deteriorate joint function and increases the risk for disability [Penninx et al. 2001, Booth et al. 2012, Lee et al. 2015]. In contrast, regular physical activity was shown to have preventive effects in animal studies and clinical trials [Valderrabano and Steiger 2011]. Exercise is further recommended by all clinical guidelines for the management of osteoarthritis [Bennell and Hinman 2011]. Strengthening and aerobic
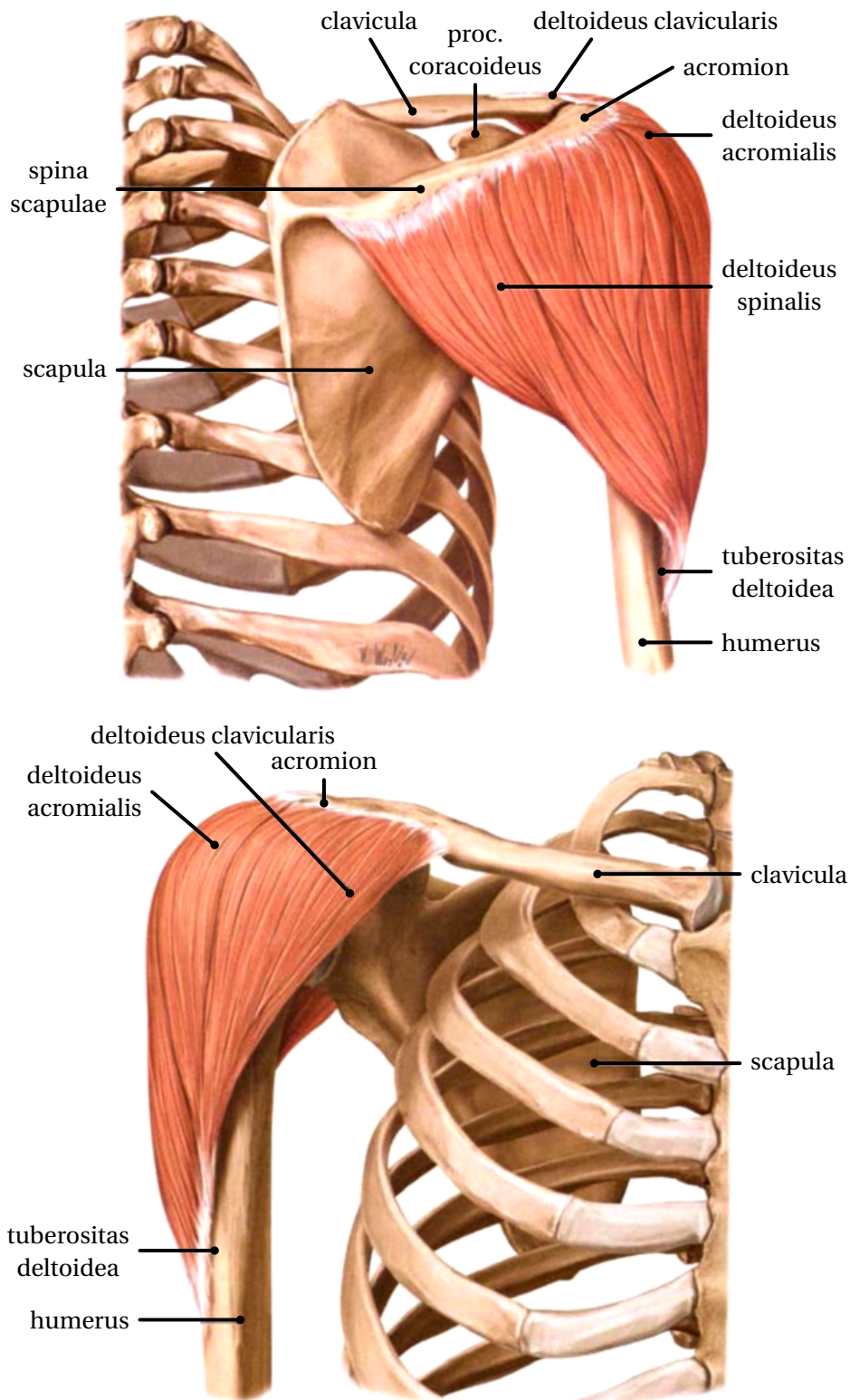
Figure 1.3 – The largest shoulder muscle is the deltoid muscle, which gives the shoulder its rounded form. Posterior (top) and anterior (bottom) view [Schünke et al. 2007].

exercises do beneficially effect the joint health in general through improved muscular balance and coordination leading to better joint alignment and dynamic stability [Valderrabano and Steiger 2011]. On the cartilage level, the tissue, not containing blood vessels, relies on nutrient supply through diffusion. Repetitive compression acts as a pumping mechanism to provide sufficient fluid exchange with the nutrient providing joint liquid. In vitro studies observed further a higher production of cartilage matrix proteins in mechanically stimulated cartilage [Grad et al. 2011], and found out further that a certain loading level is necessary to activate this response [Carver and Heath 1999]. In vitro studies also showed that a lack of mechanical stimulation lead to similar degenerative tissue responses [Jurvelin et al. 1986, Vanwanseele et al. 2002], which has been confirmed by animal studies that compared sedentary animals to animals with normal daily activity [Otterness et al. 1998]. At first glance, these findings seem to be contradictory, but they do underline the nowadays well accepted important role of regular joint motion. However the right dosage is still discussed and might be individually adapted [Brand 2005].

The glenohumeral joint is indeed not as often affected as other joints [Millett et al. 2008], but patients are considerably restricted in their daily activities through the loss of shoulder function. As pointed out in the previous paragraph, joint loads need to stay within a physiological range to avoid excessive wear, maintain cartilage supply and stimulate remodelling and repair mechanisms [Brand 2005]. As glenohumeral joint load and stability is mainly generated by the shoulder muscles, muscular function plays an important role in glenohumeral osteoarthritis research.
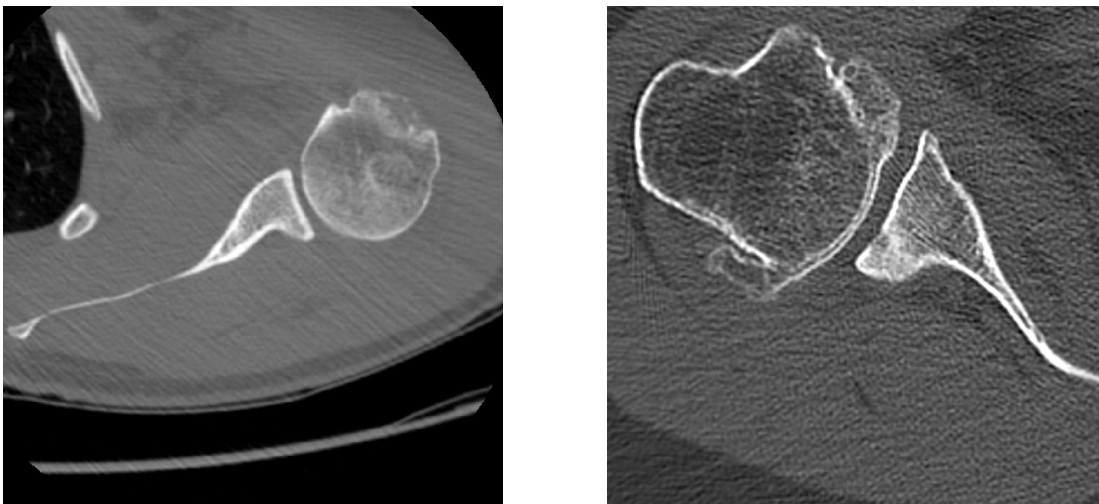
Figure 1.4 – On the left hand side, a CT image of a healthy glenohumeral joint. On the right hand side, a CT image of an osteoarthritic shoulder: the joint surface on the humeral head is flattened, on the glenoid even worn out with a biconcave pattern. On the humeral head bone, bone cysts can be seen beside the articular surface. Image source: CHUV.

Muscular imbalance, muscle weakness and muscle atrophy are in the main focus. These scenarios might be triggered by several causes. A life-style lacking physical activity might lead to a loss of muscular mass and coordinative capabilities in general. Previous injuries with immobilisation can induce atrophy of single muscle fibres. Injuries and diseases of the neural system might disturb the action potential of a whole muscle unit. Once a muscle is weakened, it does not only fatigue faster, but also slows down in voluntary and reflex motor control. If these protective mechanisms are disturbed, excessive joint motion and instability with unphysiological peak joint forces can occur [Slemenda et al. 1997, Grimaldi et al. 2009, Valderrabano and Steiger 2011].

This hypothesis is supported by studies, that could diagnose muscle weakness before the appearance of symptomatic osteoarthritis [Slemenda et al. 1997]. Furthermore, glenohumeral osteoarthritis often comes along with unsymmetrical wear patterns on the glenoid cavity, which suggests a misalignment of the joint. These wear patterns may reoccur after total shoulder arthroplasty. Following the previous argumentation, this would mean that muscular function has not been improved and that the same pathological movement patterns, previously destroying the natural joint, now wear out the prosthesis.

Putting all these findings together, therapeutic guidelines include nowadays physiotherapeutic treatment combined with analgetic and anti inflammatory therapies. Although this approach has shown to effectively reduce symptoms, it is unsatisfying in the sense that it is not a causal therapy and can thus not stop the disease nor reverse the degeneration. In advanced stages, the total joint arthroplasty is still the only option to relieve the patient from pain and restore joint mobility.

1.2.3 Rotator Cuff Tears

Tears of this group of muscles are another very common cause for shoulder pain [Williams et al. 2004]. Athletes with intense over-head activity, workers exposed to hard physical labour, and the elderly are most often affected. Within the rotator cuff, the supraspinatus tendon is the one most often affected [American Academy of Orthopaedic Surgeons 2014]. The cause for the tear can be acute after a physical impact, a chronic degeneration, or a combination of both.

Acute tears of a healthy tendon can only occur in case of a severe accident, p.e. falling on the outstretched arm. The injury can come along with a dislocation of the shoulder or an acromioclavicular separation. If the tendon is weakened due to an existing degradation process, little load is needed to tear the tendon, such as a lift or an overhead movement.

Chronic tears are the result of a degenerative process. Reasons for the degeneration might be frequent overloading of the tendon, muscular imbalance, or uncoordinated movements. On the other hand, cadaveric studies found with age increasing numbers of tears in asymptomatic individuals, concluding that rotator cuff tears are part of the natural ageing process [Nho et al.

2008]. Whatever the reason for the degeneration is, the underlying suspected mechanism is similar to cartilage degeneration: repetitive microtrauma, that cannot be compensated by the tendon's repair mechanisms, lead to a chronic state of subliminal inflammation. The mechanical properties of the tissue get locally altered, which leads to an overall weakening of the tendon [Nho et al. 2008].

The chronic tear usually starts at the insertion on the humeral head with a fraying of the tendon (Figure 1.5). The initial tear is often asymptomatic. In most cases, the tear will enlarge over time accompanied by arising or worsening symptoms [Tempelhof et al. 1999]. The symptoms include shoulder pain, reduced mobility, and reduced shoulder strength especially for abduction and overhead work. The two latter symptoms can also be observed in the case of asymptomatic tears [McCabe et al. 2005, Kim 2009]. In advanced stages of the tear, the affected muscle usually starts to degenerate, which can be seen on medical imaging. With further loss of muscular mass and force, the glenohumeral joint stiffens more and more up to a complete stiffening called frozen shoulder.

In patients with an acromion shaped in such a way, that the space between acromion and humeral head is narrow, a second site is predisposed for tears [Michener et al. 2003]. The tendon sliding underneath the acromion might rub against the bony structure. The constant mechanical stimulus can irritate the tendon tissue, which leads to inflammation in a chronic case. The inflammation again is made responsible for local alterations of the mechanical tissue properties. If the soft tissues underneath the acromion swells due to the inflammation, the situation worsens by further limiting the subacromial space. Besides the anatomical shape of the acromion, bony spurs on the acromion or osteoarthritic spurs on the acromioclavicular joint can also cause subacromial irritation of the tendon [Fongemie et al. 1998].

In both cases of chronic tears at the insertion and subacromial impingement, a dysbalance of the shoulder muscles is discussed. In the first case, muscular imbalance might lead to an
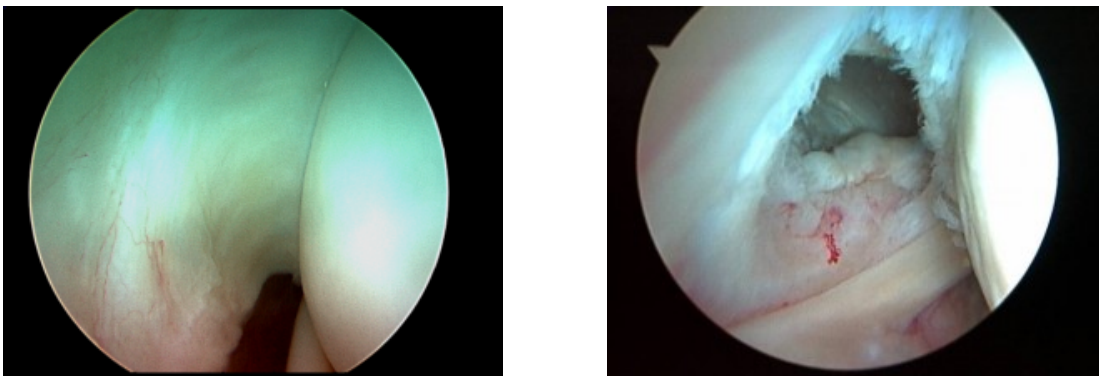
Figure 1.5 – Endoscopic images of the supraspinatus tendon insertion: on the left hand side an intact insertion is shown, on the right hand side the tendon insertion is torn. The fraying out of the tendon can clearly be seen. Image source: http://www.howardluksmd.com

overuse of the supraspinatus tendon, when the muscle is activated to compensate or counteract an other muscle. In the case of impingement, a misalignment of the glenohumeral joint with a superior shift of the humeral head can unnaturally narrow the subacromial space. Scapula motion might also contribute to the impingement: an insufficient scapulohumeral rhythm has been identified as risk factor [Kibler 1998]. Another study observed decreased anterior scapula tilting on the symptomatic side in patients with unilateral shoulder impingement syndrome [Hébert et al. 2002].

As there is no evidence, that patients benefit more from a surgical treatment than a non-surgical treatment, the recent clinical guideline is to try out a conservative treatment approach first [Seida et al. 2010]. The success of physiotherapeutic approaches lies in the general improvement of the biomechanical situation: improved muscle strength, coordination and resulting joint alignment can relieve the torn tendon.

1.2.4 Anatomic Parameters and Shoulder Diseases

In both cases of osteoarthritis and rotator cuff tears the main triggering factor is supposed to be repetitive mechanical loading: high enough to initiate damage and frequent enough to prevent complete healing of the initiated damage. While earlier studies focused on lifestyle and general health factors, recent studies analysed the influence of anatomical patient-specific characteristics. The shape of the anatomic structure determines amongst others the muscle's line of actions and the lever ratios between muscles. These individual changes require individual muscle coordination patterns during movements. Tendon loadings and joint reaction forces are thus individual. Assuming that there is an optimum geometric configuration for the shoulder, the risk for degenerative shoulder diseases increases, the further the individual anatomy differs from the optimal geometry.

To record and evaluate geometric shapes engaged in shoulder mechanics, several anatomic parameters have been proposed. A first study in 2003 analysed the glenoid inclination and its effect on rotator cuff tears. Increased glenoid inclination was associated to tears of the supraspinatus tendon. In 2006, Nyffeler et al. analysed the shape of the acromion [Nyffeler et al. 2006]. The study introduced an anatomical parameter called acromion index, which described the distance between the glenoid plane and the lateral edge of the acromion normalized by the distance between the glenoid plane and the lateral aspect of the humeral head. The study found out that patients suffering from rotator cuff tears had statistically significant increased acromion indexes [Nyffeler et al. 2006]. Another study adopted the acromion index and could conclude that patients with a small acromion index had a higher risk to develop osteoarthritis in the glenohumeral joint [Kircher et al. 2009]. Moor et al. introduced in 2013 another anatomic parameter that described the acromion cover as a combination of glenoid inclination and acromion length: the critical shoulder angle [Moor et al. 2013]. The parameter described the angle between the glenoid plane and a line pointing from the inferior tip of the glenoid to the lateral aspect of the acromion. The critical shoulder angle could be categorized

into three value ranges. Patients without shoulder pathologies had an average critical shoulder angle of 33°. Patients suffering from osteoarthritis had a decreased critical shoulder angle of 28°in average, while patients suffering from rotator cuff tears had an increased critical shoulder angle of 38°.

1.2.5 Musculoskeletal Shoulder Models

Studies of the human musculoskeletal system can be traced back into the ancient Greek era. The "corpus hippocraticum" (~500 B.C.) is a first collection of medical texts including descriptions of articulations and bone fractures. Leonardo da Vinci's cadaveric studies in the 16th century were another milestone in studies of the musculoskeletal system. He did not only make detailed drawings and descriptions of the anatomy, but also studied the mechanical function of the skeleton and the interplay with muscles. He can thus be seen as the originator of modern biomechanics. It took until the 19th century that dissection studies were complemented with the use of musculoskeletal models. First models of the shoulder appeared at the end of the 19th century [Mollier 1899, Shiino 1913]. These models with wooden bones were spanned with cables to actuate them.

Numerical models using the same idea of muscle cables appeared in the second half of the 20th century. The works of Engin et al. carried out in the 1980s were the first which aimed to develop a mathematical model of the shoulder for simulation purposes [Engin 1980, Engin and Chen 1986, Engin and Tumer 1989]. Several principles were introduced that are still used by a various number of musculoskeletal models today. The shoulder complex was modelled as a kinematic chain linked with ideal spherical joints. The motion range of the joints was restricted by cones. The cone tip was placed at the rotational centre of the joint and the following segment was constrained to stay within in the cone.

The first shoulder model which took into account dynamic effects was the Swedish model developed in the 1990s [Högfors et al. 1987; 1991, Karlsson and Peterson 1992]. This kinematic model introduced the use of a set of coordinates to describe clavicle and scapula motion in reference to the humerus. The first complete dynamic shoulder model in the sense of classical mechanics was published in 1994 which is nowadays known as the Delft Shoulder and Elbow Model [van der Helm 1994]. Through an inverse dynamics approach, the model could estimate muscle forces and joint reaction forces for the glenohumeral, the scapulothoracic and the acromioclavicular joint during dynamic movements. The scapulothoracic contact was implemented as a constraint on the scapula to slide on an ellipsoidal surface representing the ribcage. The joint reaction force of the glenohumeral joint was constrained to point from the rotation centre towards the glenoid cavity to ensure the stability of the glenohumeral joint. The work of van der Helm and Veenbaas [1991] was also the first to study the effect of the placement of origin and insertion points of the cable muscles, especially in the case of muscles with broad attachment sites. The Delft model can be seen as the ancestor of subsequent published musculoskeletal shoulder models. Many of its attributes can be found in more

recent models. More modern developments often focus on a more complete representation of the anatomy, new approaches to describe shoulder kinematics, improving the modelling of muscles or new algorithms to solve the muscle force estimation problem.

For example in 1997, Garner and Pandy published a complete dataset of the upper limb derived from the Visible Human Project. It included the anatomic description of the bony kinematic chain and 42 muscles segments spanning from thorax to the hand. Muscle contraction parameters were derived from geometric measurements on the muscle macro and micro structure. The dataset has been used to implement a shoulder model for the analysis of the properties of the muscle-tendon unit. [Garner and Pandy 1997; 2000; 2003]

Other well known models of the shoulder complex are the shoulder model in the AnyBody Modelling System and the SimTK Opensim Shoulder Model [Lindsay 2001, Damsgaard et al. 2006, Holzbaur et al. 2005, Delp et al. 2007]. Both models have been progressively developed further and have been used for different purposes ranging from solving the muscle force coordination problem up to predicting surgery outcome. Reviews of further musculoskeletal shoulder models can be found in literature [Yang et al. 2010, Prinold et al. 2013].

Parallel to the development of the numerical models, algorithms and methods have been developed and customized to approach the specific problems of musculoskeletal shoulder models. These include amongst others the computation of muscle forces and joint reaction forces. Like other musculoskeletal systems, the upper limb is spanned by more muscles than its number of degrees of freedom. This overactuation results in an infinite amount of muscle force combinations to produce the same movement. Methods to solve this problem are called coordination strategies [Erdemir et al. 2007]. A common approach is as follows: the motion of interest is discretised over a desired time frame. The required torques and accelerations in the joints can be obtained by using an inverse dynamic model of the shoulder complex. At each timepoint, an optimization problem is defined to compute the muscle forces that result in the needed joint torque. The optimization is usually defined as the minimisation problem of a cost function based on a physiological hypothesis. The most common cost function is the minimisation of mean square muscle stresses, which is the sum of the squared muscle forces divided by the physiological cross sectional areas [van der Helm 1994]. Cost functions can be based on other mechanical (p.e. forces) or metabolic (p.e. oxygen consumption) or energy quantities. The optimisation must further respect the constraints given by the skeletal kinematics and the used muscle model such as glenohumeral stability and maximum muscle forces. The optimisation problem can be solved using p.e. nullspace optimisation, which is a quadratic programming method taking advantage of the relationship between muscle forces and joint torques [Praagman et al. 2006, Aeberhard et al. 2009, Terrier et al. 2010].

A second approach is the tracking of experimentally measured muscle activation. This method requires, in case of deep muscles technical difficult, experimentally measured EMG data. It further requires a suitable muscle model and the identification of its parameters to link the electric activation with the generated muscle force. The obtained forces can then be used

in forward dynamic models to predict movements [Langenderfer et al. 2005], or in inverse dynamic models to minimise the difference between the estimated and the measured muscle activity [Terrier et al. 2007]. Although EMG tracking methods were proofed to better estimate the activity of stabilizing muscles [Engelhardt et al. 2015], inverse dynamics approaches provide the greater flexibility as they do not depend on experimental data.

1.2.6 Tissue Models

While musculoskeletal shoulder models were mainly developed to analyse shoulder kinematics and compute muscle forces, the main goal of tissue models is the analysis of material strains and stresses. In biomechanics, the focus lies on the modelling of bone, cartilage, ligaments, tendons, and muscles.

When modelling biological tissues with finite elements, the used constitutive law has an important impact on the results. This equation provides the link between tissue deformation and stress response. In the case of biological materials, this equation is nonlinear. Biological tissues possess further a complex composition on a microstructural level which yields to a even more complex stress response under mechanical load. This includes the spatial variation of material properties called inhomogeneity, p.e. in bone induced by varying density. A direction dependent stress response called anisotropy can be found in fibrous tissues such as tendon and muscle. Tissues that contain high quantities of water as cartilage, show a load rate dependent stress response called viscoelasticity. Constitutive equations are available in literature that can describe the complex behaviour of biological soft tissue within a mathematical and physical consistent framework [Holzapfel and Ogden 2006, Miller and Nielsen 2010, Maurel 2014]. On the other hand, the choice for a constitutive law does not only depend on its capacity to precisely describe the material behaviour, but also on the feasibility to identify its parameters. It can be said in general, that the more deformation effects are covered by the constitutive equation, the more parameters have to be determined. And that's where the crux lies. The more parameters to identify, the more experimental test are necessary, which can be an expensive and time consuming task. Further, each test has to be carried out several times, to cover the natural property variation in biological materials. In case of animal samples, this problem might be statistically approached by increasing the number of samples. Where as in the case of human tissue samples, it is usually difficult to obtain even small numbers of samples. Further, the mechanical characterisation of soft tissues can usually not be done in vivo. Property alterations due to conservation are to be limited. For experimental testing with long duration conservative measures might be necessary even during the testing. All these challenges lead to the fact, that despite the availability of constitutive laws with a high level of detail, the choice for a material model is restricted.

Only one numerical shoulder model could be found in literature that analysed the articular contact of the glenohumeral joint [Buchler et al. 2002]. Cartilage layers were modelled with a hyperelastic Neohookean constitutive law. The stress distribution in the scapula was analysed.

However, the model only considered the muscle forces of the rotator cuff muscles. Another shoulder model analysed humeral head translations and contact pressure after total shoulder arthroplasty [Terrier et al. 2007; 2008; 2010]. Numerical models for the articular contact of the knee have successfully been modelled with complex cartilage models including poroelastic and fluid flow effects [Kazemi et al. 2013]. However, only few models consider the subchondral bone.

Two studies could be found that analysed tendon strains in the shoulder [Wakabayashi et al. 2003, Sano et al. 2006]. Both works focused on the supraspinatus tendon and the pathological case of partial thickness tears. The models replicated the transition from tendon to bone tissue via cartilaginous tissues. However, all tissues were approximated as linear elastic material and the model was limited to a 2D analysis. The three dimensional deformation state was thus not replicated.

The 3D modelling of the muscle-tendon complex around the shoulder was achieved by a finite element model which aimed to measure muscle moment arms for the deltoid and rotator cuff muscles [Webb et al. 2014]. Muscles and tendons were simulated as hyperelastic transverse isotropic materials that wrapped around the bone structure and considering tissue interaction. The model did not take into account muscle force variations during movements: the muscle activations were kept constant. Findings about strain-stress distributions in the muscle were not published.

1.3   Structure of the Thesis

The influence of anatomic parameters on shoulder pathologies is not only a proof that the mechanical environment of a joint is essential for its homeostasis, but also provides a tool to evaluate a patient's risk for the development of shoulder disorders. Knowledge about the individual anatomy can thus not only help to customize treatment approaches. It can also be used as indicator for preventive physiotherapy or lifestyle accommodations. The studies cited had only observatory character. The goal of this thesis is to adopt these findings and find a mechanical explanation for these observations with the means of numerical modelling. To do this, three numerical models were developed to analyse the effect of anatomic parameters on the glenohumeral joint:

The first model was a musculoskeletal model of the upper limb with the purpose to compute the muscle forces of the shoulder spanning muscles and the resultant glenohumeral joint reaction forces (Figure 1.6). Based on MRI images of a healthy young volunteer, the model contained thorax, clavicle, scapula and humerus spanned by 42 muscle segments. Muscle contraction parameters were taken from literature [Garner and Pandy 2000]. Input data were the dynamic kinematics of the movement of interest. The muscle force estimation solved the undetermined problem of muscle force distribution using a nullspace optimization algorithm. The model provided thus muscle forces, muscle moment arms, joint torques and joint reaction forces. The model had further the flexibility to vary anatomic parameters.

The second model was a finite element model of the glenohumeral joint. The glenohumeral joint reaction force computed in the first part was used as input to evaluate the articular contact resulting from the reaction force (Figure 1.6). The model contained scapula, humerus and the associated cartilage layers. Cartilage was modelled as hyperelastic incompressible material forming a frictionless joint contact. The translation of the humeral head on the glenoid cavity was allowed. The results of the contact model were the humeral head translations, the size, shape and migration of the cartilage contact zone, contact pressure and cartilage deformation. By applying anatomic parameter dependent joint reaction forces, the anatomic parameter can be correlated with cartilage loadings, and thus risk factors for osteoarthritis can be derived.

The third model focused on the supraspinatus tendon. The supraspinatus muscle forces and humeral head translations obtained in the first and second model were further used in this finite element model of the supraspinatus insertion on the humeral head (Figure 1.6). The tendon was modelled with an anisotropic hyperelastic constitutive law whose parameters were identified by a fitting to experimental data. The model was able to predict tendon deformation close to the insertion, where tears frequently occur, as well as tendon impingement between the humeral head and the scapula acromion. Changes in tendon loading can then be correlated to changes in anatomic parameters to evaluate its influence on causing supraspinatus tendon damage.

In the last part of the work, these three numerical models were used for a parametric study on the acromion length and the glenoid inclination (Figure 1.6). The goal was to find correlations between the anatomic variations and shoulder muscle forces, joint reaction forces, cartilage strains, humeral head migration, and tendon strains.
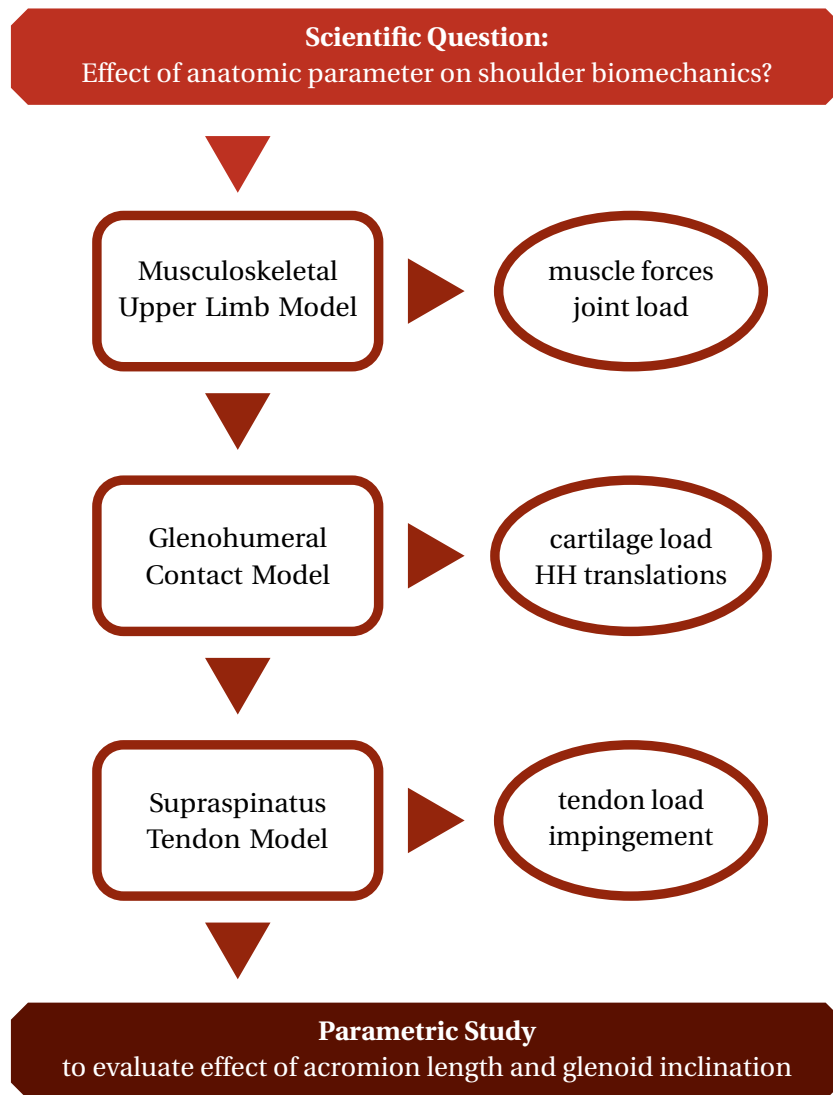
Figure 1.6 – General structure of the project showing the scientific question (top), the work flow through three numerical models (left column) and the model's result (right column), and the final parametric study (bottom).

1.B Bibliography

Bibliography

Aeberhard M., Michellod Y., Müllhaupt P., Terrier A., Pioletti D. P., and Gillet. D.: Dynamical biomechanical model of the shoulder: Null space based optimization of the overactuated system. *ROBIO 2008 IEEE International Conference*, pages 67–73, 2009.

American Academy of Orthopaedic Surgeons, August 2014. URL http://orthoinfo.aaos.org/topic.cfm?topic=a00064. "Most tears occur in the supraspinatus muscle and tendon, . . . If you fall down on your outstretched arm or lift something too heavy with a jerking motion, you can tear your rotator cuff.".

Bennell K. L. and Hinman R. S.: A review of the clinical evidence for exercise in osteoarthritis of the hip and knee. *Journal of Science and Medicine in Sport*, 14(1):4–9, 2011.

Blasier R. B., Soslowsky L. J., Malicky D. M., and Palmer M. L.: Posterior glenohumeral subluxation: active and passive stabilization in a biomechanical model. *Journal of Bone and Joint Surgery—American*, 79:433–440, 1997.

Booth F. W., Roberts C. K., and Laye M. J.: Lack of exercise is a major cause of chronic diseases. *Comprehensive Physiology*, 2(2):1143–1211, 2012.

Brand R. A.: Joint contact stress: a reasonable surrogate for biological processes? *The Iowa orthopaedic journal*, 25:82–94, 2005.

Brandt K. D., Dieppe P., and Radin E.: Etiopathogenesis of osteoarthritis. *Medical Clinics of North America*, 93(1):1–24, 2009.

Breteler M. D. K., Spoor C. W., and der Helm F. C. T. V.: Measuring muscle and joint geometry parameters of a shoulder for modeling purposes. *Journal of Biomechanics*, 32(11):1191–1197, 1999.

Buchler P., Ramaniraka N. A., Rakotomanana L. R., Iannotti J. P., and Farron A.: A finite element model of the shoulder: application to the comparison of normal and osteoarthritic joints. *Clin. Biomech.*, 17(9-10):630–639, 2002.

Buckwalter J. A. and Martin J. A.: Osteoarthritis. *Advanced Drug Delivery Reviews*, 58(2):150–167, 2006.

Carver S. E. and Heath C. A.: Increasing extracellular matrix production in regenerating cartilage with intermittent physiological pressure. *Biotechnology and Bioengineering*, 62(2):166–174, 1999.

Damsgaard M., Rasmussen J., Christensen S. T., Surma E., and de Zee M.: Analysis of musculoskeletal systems in the anybody modeling system. *Simulation Modelling Practice and Theory*, 14(8):1100–1111, 2006.

Delp S. L., Anderson F. C., Arnold A. S., Loan P., Habib A., John C. T., Guendelman E., and Thelen D. G.: Opensim: Open-source software to create and analyse dynamic simulations of movement. *IEEE Transactions on Biomedical Engineering*, 54(11):1940–1950, 2007.

Egloff C., Hügle T., and Valderrabano V.: Biomechanics and pathomechanisms of osteoarthritis. *Swiss Med Wkly*, 142:w13583, 2012.

Engelhardt C., Camine V. M., Ingram D., Muellhaupt P., Farron A., Pioletti D., and Terrier A.: Comparison of an EMG-based and a stress-based method to predict shoulder muscle forces. *Comput Methods Biomech Biomed Engin*, 18(12):1272–1279, 2015.

Engin A.: On the biomechanics of the shoulder complex. *Journal of Biomechanics*, 13(7): 575–581,583–590, 1980.

Engin A. E. and Chen S. M.: Statistical data base for the biomechanical properties of the human shoulder complex - I: kinematics of the shoulder complex. *Journal of Biomechanical Engineering*, 108:215–221, 1986.

Engin A. E. and Tumer S. T.: Three-dimensional kinematic modelling of the human shoulder complex - part I: Physical model and determination of joint sinus cones. *Journal of Biomechanical Engineering*, 111(2):107–112, 1989.

Erdemir A., McLean S., Herzog W., and van den Bogert A. J.: Model-based estimation of muscle forces exerted during movements. *Clin. Biomech.*, 22(2):131–154, 2007.

Eyre D. R.: Collagens and cartilage matrix homeostasis. *Clinical Orthopaedics and Related Research*, (427 SUPPL.):118–122, 2004.

Fongemie A. E., Buss D. D., and Rolnick S. J.: Management of shoulder impingement syndrome and rotator cuff tears. *American Family Physician*, 57(4):667–674, 1998.

Garner B. A. and Pandy M. G.: A kinematic model of the upper limb based on thevisible human project (vhp) image dataset. *Comput Methods Biomech Biomed Engin*, 2:107–124, 1997.

Garner B. A. and Pandy M. G.: Musculoskeletal model of the upper limb based on the visible human male dataset. *Comput Methods Biomech Biomed Engin*, 4:93–126, 2000.

Garner B. A. and Pandy M. G.: Estimation of musculotendon properties in the human upper limb. *Annals of Biomedical Engineering*, 31:207–220, 2003.

Grad S., Eglin D., Alini M., and Stoddart M. J.: Physical stimulation of chondrogenic cells in vitro: A review. *Clinical Orthopaedics and Related Research*, 469(10):2764–2772, 2011.

Gray H.: *Anatomy of the human body*. Lea & Febiger, 2000.

Grimaldi A., Richardson C., Durbridge G., Donnelly W., Darnell R., and Hides J.: The association between degenerative hip joint pathology and size of the gluteus maximus and tensor fascia lata muscles. *Manual Therapy*, 14(6):611–617, 2009. cited By 33.

Hébert L., Moffet H., McFadyen B., and Dionne C.: Scapular behavior in shoulder impinge-ment syndrome. *Archives of Physical Medicine and Rehabilitation*, 83(1):60–69, 2002.

Helmick C. G., Felson D. T., Lawrence R. C., Gabriel S., Hirsch R., Kwoh C. K., Liang M. H., Kremers H. M., Mayes M. D., Merkel P. A., Pillemer S. R., Reveille J. D., and Stone J. H.: Estimates of the prevalence of arthritis and other rheumatic conditions in the United States. part I. *Arthritis and Rheumatism*, 58(1):15–25, 2008.

Högfors C., Peterson B., and Herberts P.: Biomechanical model of the human shoulder - I. elements. *Journal of Biomechanics*, 20(2):157–166, 1987.

Högfors C., Peterson B., Sigholm G., and Herberts P.: Biomechanical model of the human shoulder - II: the shoulder ryrthm. *Journal of Biomechanics*, 24(8):699–709, 1991.

Holzapfel G. and Ogden R.: *Mechanics of biological tissue.* Springer, 2006.

Holzbaur K. R., Murray W. M., and Delp S. L.: A model of the upper extremity for simulating musculoskeletal surgery and analyzing neuromuscular control. *Ann Biomedical Engineering*, 33(6):829–840, 2005.

Hughes R. E., Bryant C. R., and Hall J. M.: Glenoid inclination is associated with full-thickness rotator cuff tears. *Clin Orthop Relat Res*, 407:86–91, 2003.

Jurvelin J., Kiviranta I., Tammi M., and Helminen J. H.: Softening of canine articular cartilage after immobilization of the knee joint. *Clinical orthopaedics and related research*, (207): 246–252, 1986.

Karlsson D. and Peterson B.: Towards a model for force predictions in the human shoulder. *Journal of Biomechanics*, 25(2):189–199, 1992.

Kazemi M., Dabiri Y., and Li L.: Recent advances in computational mechanics of the human knee joint. *Computational and Mathematical Methods in Medicine*, Article number 718423, 2013.

Kibler W. B.: The role of the scapula in athletic shoulder function. *American Journal of Sports Medicine*, 26(2):325–337, 1998.

Kim S. Y.: *Supraspinatus Musculotendinous Architecture: A Cadaveric and In Vivo Ultrasound Investigation of the Normal and Pathological Muscle.* PhD thesis, University of Toronto, 2009.

Kircher J., Morhard M., Gavriilidis I., Magosch P., Lichtenberg S., and Habermeyer P.: Is there an association between a low acromion index and osteoarthritis of the shoulder? *International Orthopaedics*, (7):1005–1010, 2009.

Langenderfer J., Jerabek S. A., Thangamani V. B., Kuhn J. E., and Hughes R. E.: Musculoskeletal parameters of muscles crossing the shoulder and elbow and the effect of sarcomere length sample size on estimation of optimal muscle length. *Clin. Biomech.*, 19:664–670, 2004.

Langenderfer J. E., LaScalza S., Mell A., Carpenter J. E., Kuhn J. E., and Hughes R. E.: An EMG-driven model of the upper extremity and estimation of long head biceps force. *Comp. in Bio. and Med.*, 35(1):25–39, 2005.

Lee J., Chang R. W., Ehrlich-Jones L., Kwoh C. K., Nevitt M., Semanik P. A., Sharma L., Sohn M.-W., Song J., and Dunlop D. D.: Sedentary behavior and physical function: Objective evidence from the osteoarthritis initiative. *Arthritis Care and Research*, 67(3):366–373, 2015.

Lindsay N.: Modelling of the shoulder mechanism. a report describing the development of a three-dimensional biomechanical model of the human shoulder complex. *Technical Report 106, Institute of Mechanical Engineering, Aalborg University*, 2001.

Luime J. J., Koes B. W., Hendriksen I. J. M., Burdorf A., Verhagen A. P., Miedema H. S., and Verhaar J. A. N.: Prevalence and incidence of shoulder pain in the general population; a systematic review. *Scand J Rheumatol*, 33(2):73–81, 2004.

Massimini D., Boyer P., Papannagari R., Gill T., Warner J., and Li G.: In-vivo glenohumeral translation and ligament elongation during abduction and abduction with internal and external rotation. *Journal of Orthopaedic Surgery and Research*, 7(1):1–9, 2012.

Matava M. J., Purcell D. B., and Rudzki J. R.: Partial-thickness rotator cuff tears. *Am J Sports Med*, 33(9):1405–1417, 2005.

Maurel W.: *Biomechanical Models for Soft Tissue Simulation*. Springer, 2014.

McCabe R. A., Nicholas S. J., Montgomery K. D., Finneran J. J., and McHugh M. P.: The effect of rotator cuff tear size on shoulder strength and range of motion. *J Orthop Sports Phys Ther*, 35(3):130–135, 2005.

Michener L., McClure P., and Karduna A.: Anatomical and biomechanical mechanisms of subacromial impingement syndrome. *Clinical Biomechanics*, 18(5):369–379, 2003.

Miller K. and Nielsen P., editors.: *Computational Biomechanics for Medicine*. Springer, 2010.

Millett P. J., Gobezie R., and Boykin R. E.: Shoulder osteoarthritis: Diagnosis and management. *American Family Physician*, 78(5):605–612, 2008.

Mitchell C., Adebajo A., Hay E., and Carr A.: Shoulder pain: diagnosis and management in primary care. *BMJ*, 331(7525):1124–1128, 2005.

Mollier S.: *Ueber die Statik und Mechanik des menschlichen Schultergürtels unter normalen und pathologischen Verhältnissen: mit 7 Tabellen*. Fischer, 1899. URL http://books.google.ch/books?id=o8u2QAAACAAJ.

Moor B. K., Bouaicha S., Rothenfluh D. A., Sukthankar A., and Gerber C.: Is there an association between the individual anatomy of the scapula and the development of rotator cuff tears or osteoarthritis of the glenohumeral joint? A radiological study of the critical shoulder angle. *Bone and Joint Journal*, 95 B(7):935–941, 2013.

Murray I. R., Goudie E. B., Petrigliano F. A., and Robinson C. M.: Functional anatomy and biomechanics of shoulder stability in the athlete. *Clinics in Sports Medicine*, 32(4):607–624, 2013.

Netter F. H.: *Atlas of Human Anatomy.* Elsevier, 2015. ISBN 978-3-437-41605-7.

Nho S. J., Yadav H., Shindle M. K., and MacGillivray J. D.: Rotator cuff degeneration: Etiology and pathogenesis. *Am J Sports Med*, 36(5):987–993, 2008.

Nyffeler R. W., Werner C. M., Sukthankar A., Schmid M. R., and Gerber C.: Association of a large lateral extension of the acromion with rotator cuff tears. *The Journal of Bone & Joint Surgery*, 88(4):800–805, 2006.

Otterness I. G., Eskra J. D., Bliven M. L., Shay A. K., Pelletier J.-P., and Milici A. J.: Exercise protects against articular cartilage degeneration in the hamster. *Arthritis and Rheumatism*, 41(11):2068–2076, 1998.

Penninx B. W. J. H., Messier S. P., Rejeski W. J., Williamson J. D., DiBari M., Cavazzini C., Applegate W. B., and Pahor M.: Physical exercise and the prevention of disability in activities of daily living in older persons with osteoarthritis. *Archives of Internal Medicine*, 161(19): 2309–2316, 2001.

Potau J. M., Bardina X., Ciurana N., Camprubí D., Pastor J. F., de Paz F., and Barbosa M.: Quantitative analysis of the deltoid and rotator cuff muscles in humans and great apes. *International Journal of Primatology*, 30(5):697–708, 2009.

Praagman M., Chadwick E., van der Helm F., and Veeger H.: The relationship between two different mechanical cost functions and muscle oxygen consumption. *Journal of Biomechanics*, 39(4):758 – 765, 2006.

Prinold J. A., Masjedi M., Johnson G. R., and Bull A. M. J.: Musculoskeletal shouldermodels: A technical review and proposals for research foci, proceedings of the institution of mechanical engineers. *Journal of Engineering in Medicine*, 227:1041–1057, 2013.

Sano H., Wakabayashi I., and Itoi E.: Stress distribution in the supraspinatus tendon with partial-thickness tears: An analysis using two-dimensional finite element model. *Journal of Shoulder and Elbow Surgery*, 15(1):100 – 105, 2006.

Schünke M., Schulte E., and Schumacher U.: *Prometheus - LernAtlas der Anatomie: Allgemeine Anatomie und Bewegungssystem.* Thieme, 2007. ISBN 978-3131395221.

Seida J. C., LeBlanc C., Schouten J. R., Mousavi S. S., Hartling L., Vandermeer B., Tjosvold L., and Sheps D. M.: Systematic review: Nonoperative and operative treatments for rotator cuff tears. *Ann Intern Med*, 153(4):246–255, 2010.

Shiino K.: Schultergelenkbewegungen und schultermuskelarbeit. *Arch. Anat. Physiol., Suppl. Anat.*, pages 1–88, 1913.

Slemenda C., Brandt K. D., Heilman D. K., Mazzuca S., Braunstein E. M., Katz B. P., and Wolinsky F. D.: Quadriceps weakness and osteoarthritis of the knee. *Annals of Internal Medicine*, 127(2):97–104, 1997.

Tempelhof S., Rupp S., and Seil R.: Age-related prevalence of rotator cuff tears in asymptomatic shoulders. *J Shoulder Elbow Surg*, 8(4):296 – 299, 1999.

Terrier A., Reist A., Vogel A., and Farron A.: Effect of supraspinatus deficiency on humerus translation and glenohumeral contact force during abduction. *Clin. Biomech.*, 22(6):645–651, 2007.

Terrier A., Vogel A., Farron A., and Capezzali M.: An algorithm to allow humerus translation in the indeterminate problem of shoulder abduction. *Med Eng Physics*, 30(6):710–716, 2008.

Terrier A., Aeberhard M., Michellod Y., Müllhaupt P., Gillet D., Farron A., and Pioletti D.: A musculoskeletal shoulder model based on pseudo-inverse and nullspace optimization. *Med Eng Physics*, 32:1050–1056, 2010.

Valderrabano V. and Steiger C.: Treatment and prevention of osteoarthritis through exercise and sports. *Journal of Aging Research*, Article number 374653, 2011.

van der Helm F. C. T.: A finite element musculoskeletal model of the shoulder mechanism. *J Biomech*, 27(5):551–569, 1994.

van der Helm F. C. T. and Veenbaas R.: Modelling the mechanical effect of muscles with large attachment sites: Application to the shoulder mechanism. *Journal of Biomechanics*, 24(12): 1151–1163, 1991.

Vanwanseele, Eckstein F., Knecht H., Stüssi E., and Spaepen A.: Knee cartilage of spinal cord-injured patients displays progressive thinning in the absence of normal joint loading and movement. *Arthritis and Rheumatism*, 46(8):2073–2078, 2002.

Veeger H. E. J. and van der Helm F. C. T.: Shoulder function: The perfect compromise between mobility and stability. *J Biomech*, 40(10):2119–2129, 2007.

Vincent T.: *Osteoarthritis*. Oxford University Press, 2nd edition, 2004.

Wakabayashi I., Itoi E., Sano H., Shibuya Y., Sashi R., Minagawa H., and Kobayashi M.: Mechanical environment of the supraspinatus tendon: a two-dimensional finite element model analysis. *Journal of Shoulder and Elbow Surgery*, 12(6):612–617, 2003.

Webb J., Blemker S., and Delp S.: 3D finite element models of shoulder muscles for computing lines of actions and moment arms. *Computer Methods in Biomechanics and Biomedical Engineering*, 17(8):829–837, 2014.

Williams G. R., Rockwood C. A., Bigliani L. U., Iannotti J. P., and Stanwood W.: Rotator cuff tears: Why do we repair them? *J Bone Joint Surg Am*, 86(12):2764–2776, 2004.

Yang J., Feng X., Kim J. H., and Rajulu S.: Review of biomechanical models of the human shoulder complex. *I. J. H. F. M. S.*, 1(3):271–293, 2010.

Yu D.: Shoulder pain in hemiplegia. *Physical Medicine and Rehabilitation Clinics of North America*, 15(3):683–697, 2004.

2 Musculoskeletal Upper Limb Model

On the following pages the reader finds two major works that have been performed in the context of muscle force estimation. A first section deals with the comparison of two widely used approaches to the muscle coordination problem: EMG tracking and optimisation following predefined criteria. For the comparison, a finite element model of the glenohumeral joint has been used. Although this model included a shoulder after total shoulder athroplasty and six muscles only, it has been chosen due to its ability to predict humeral head translations. For the further project course, a more complete model of the shoulder girdle was needed which led to the development of the upper limb model presented in the second part of this chapter. The upper limb model contained the whole shoulder complex from thorax to forearm spanned by 42 muscle segments. For the solving of the muscle coordination problem it was decided to use an optimisation algorithm to be independent on EMG data. The chapter finishes with an outlook on possible future works to overcome certain limitations of the developed model.

2.1   Comparison of Muscle Force Estimation Methods

This section has been published in Computer Methods in Biomechanical and Biomedical Engineering under the title "Comparison of an EMG-based and a stress-based method to predict shoulder muscle forces" [Engelhardt et al. 2015].

2.1.1   Introduction

The obvious difficulty in measuring muscle forces in vivo led to the development of several musculoskeletal shoulder models to predict these forces and analyse the glenohumeral joint kinematics [Erdemir et al. 2007, Yang et al. 2010]. Because of the redundant biomechanical system, the equations of equilibrium have to be extended with further criteria. Two approaches can be often found in literature: EMG-based methods [Langenderfer et al. 2005, Terrier et al. 2007, Nikooyan et al. 2012] and stress-based methods [Karlsson and Peterson 1992, van der

Helm 1994b, Buchanan and Shreeve 1996, Lin et al. 2004, Charlton and Johnson 2006, Terrier et al. 2010].

EMG-based methods require the recording of the electric muscle activity. This measurement is technically difficult, especially for deep muscles, such as the rotator cuff muscles. The post-processing of the raw data can also be rather difficult. Further, the link between muscle activity and muscle force requires assumptions with unknown parameters. EMG measurements are then used by forward dynamic models to predict the movement [Langenderfer et al. 2005] or by inverse models to minimise the difference between estimated and measured muscular activity [Terrier et al. 2007]. The clear advantage of EMG-based methods is however to replicate as close as possible the muscular activity, while its main drawback is the dependency to experimental data. This method is therefore limited to movements with available EMG data.

The stress-based method is independent of any experimental data. It minimises a cost function based on a physiological hypothesis. Different cost functions have already been proposed [Erdemir et al. 2007]. Variations of the sum of the muscle stresses are most commonly used. The method requires an inverse method to estimate the solution space for a specific movement. Within this solution space, optimisation techniques are applied to minimise the cost function. This optimisation is usually constrained by physiological criteria, such as the minimum and maximum muscle forces, or joint stability criteria [van der Helm 1994b, Happee and van der Helm 1995]. The main advantage of this method is its applicability to arbitrary movements. Its main drawback is the difficulty in correctly prediction the observed co-contraction of antagonist muscle [Cholewicki et al. 1995, Gagnon et al. 2001].

Although several stress-based models were validated using EMG measurements [Erdemir et al. 2007], none of them used this EMG-data to predict muscle forces. Therefore, the goal of this work, was to implement an EMG and a stress-based method within the same musculoskeletal shoulder model and to compare their predictions of muscle forces, glenohumeral reaction force, and humeral head translations.

2.1.2 Methods

An EMG-based and a stress-based method were implemented into the same musculoskeletal shoulder model. The work was based on a 3D model of the glenohumeral joint [Terrier et al. 2007]. The resulting muscle forces, glenohumeral joint load and humeral head translations were compared.

Musculoskeletal Shoulder Model

The musculoskeletal shoulder model [Terrier et al. 2007] was based on cadaveric computer tomography (CT) scans of a shoulder without any sign of pathology. The model represented the glenohumeral joint after total shoulder arthroplasty (TSA). The glenohumeral joint was replaced by an Aequalis prosthesis (Tornier Inc., Edina, MN). The metallic humeral head

sphere had a radius of 24 mm. The radius of the articular surface of the polyethylene glenoid implant was 30 mm. The model included the scapula, the humerus and ten active muscle units. The subscapularis (SC), supraspinatus (SS), infraspinatus combined with teres minor (IS), middle deltoid (MD), anterior deltoid (AD) and posterior deltoid (PD). The SC and IS were divided into three sections. The origins of the three sections were evenly distributed on the attachment zones on the scapula. The muscles were separated into a passive and an active part. The passive parts wrapped around the anatomic structure and the active parts generated the active muscle force. Bones were assumed rigid. The humeral metallic component of the prosthesis was also assumed rigid. The polyethylene glenoid implant was modelled as a linear elastic material with a Young's modulus of 500 MPa and a Poisson ratio of 0.4. The articular contact between glenoid implant and humeral head sphere was assumed as frictionless sliding contact.

We simulated a quasi-static movement of abduction in the scapula-plane from a rest position to 150° of elevation. The rotations of humerus and scapula were implemented as recorded by an experimental study [McClure et al. 2001]. The translation of the humeral head on the glenoid fossa was allowed. It was only constrained by the muscles, which wrapped around the bony structures. Sliding contacts were considered between between muscles and bones. The arm weight was set to 3.75 kg, which corresponds to 5 % bodyweight of a 75 kg person.

The muscle forces must satisfy the mechanical equilibrium of moments:

$$\sum \boldsymbol{r}_m \times \boldsymbol{f}_m + \sum \boldsymbol{r}_e \times \boldsymbol{f}_e = \boldsymbol{0} \tag{2.1}$$

where $\boldsymbol{r}_m$ is the muscle moment arm , $\boldsymbol{f}_m$ is the muscle force, $\boldsymbol{f}_e$ is an external force and $\boldsymbol{r}_e$ the corresponding moment arms. Here, the arm weight was the only external load. The summation was done over the 10 muscle units. The left part of equation 2.1 can be rewritten

$$\sum \boldsymbol{r}_m \times \boldsymbol{f}_m = \boldsymbol{R}\boldsymbol{f} = \boldsymbol{q} \tag{2.2}$$

where $\boldsymbol{R}$ is the muscle moment arm matrix, the vector $\boldsymbol{f}$ contains the scalar values of all muscle forces and the vector $\boldsymbol{q}$ represents the resulting moment. The indeterminacy of the vectorial equation 2.1 was solved by the EMG-based and stress-based methods.

EMG-based method

The EMG-based method solved the indeterminacy of the mechanical equilibrium with experimentally measured EMG signals [Kronberg et al. 1990]. The EMG measurements were obtained from 5 healthy subjects in static positions at choosen degrees of abduction. Bipolar

surface electrodes were used for the deltoid muscles and fine wire electrodes for underlying rotator cuff muscles. EMG signals were filtered, rectified and normalized [Kronberg et al. 1990], which is considered as a reasonable approach for use in static simulations [Lloyd and Besier 2003]. We used a Hill type muscle model to link muscle activation $\bar{a}_m$ and muscle force F_m [Zajac 1989]:

$$F_m = k\bar{a}_m f_m(l_m) PCSA \tag{2.3}$$

where k is the Fick constant, $f_m(l_m)$ the isometric force-length relationship and $PCSA$ the physiological cross sectional area of the muscle. The activation $\bar{a}_m$ can vary between 0 (no activation) and 1 (maximum activation). The $f_m(l_m)$ and $PCSA$ were taken from literature [Langenderfer et al. 2004]. In general the experimentally measured muscle activities did not lead to muscle forces that fulfilled the mechanical equilibrium given in equation 2.1. The following minimisation algorithm was implemented, to estimate muscle activities a_m that stabilize the joint while staying as close as possible to the experimentally measured activity $\bar{a}_m$:

$$\min G(a_m) \text{ with: } G(a_m) = \sum_{m=1}^{M} (a_m - \bar{a}_m)^2 \tag{2.4}$$

The minimisation problem was constrained by the mechanical equilibrium in equation 2.1 and positive muscle activation:

$$0 < a_m < 1 \tag{2.5}$$

Stress-based method

The stress-based method used a pseudo-inverse null space optimisation algorithm [Terrier et al. 2010, Ingram et al. 2012]. The cost function g_1 was the sum of square muscle stresses.

$$\min g_1(\boldsymbol{f}) \text{ with: } g_1(\boldsymbol{f}) = \sqrt{\frac{1}{n}\sum_{i=0}^{n}\left(\frac{f_i}{ACSA_i}\right)^2} \tag{2.6}$$

where $ACSA_i$ is the anatomical cross sectional area of the i-th muscle. The optimisation problem was constrained by the physiological criteria that muscles can only a provide contractile force, which was limited by a maximum value:

$$0 < f_i < f_i^{max}(PCSA_i, l_i) \tag{2.7}$$

This constrained indeterminate problem was solved in two steps. First, the cost function g_1 was minimised using Lagrange multipliers:

$$g_1(\boldsymbol{f}, \lambda) = \boldsymbol{f}^T \boldsymbol{E} \boldsymbol{f} - \lambda(\boldsymbol{R}\boldsymbol{f} - \boldsymbol{q}) \tag{2.8}$$

The matrix $\boldsymbol{E}$ was diagonal and contained the values of the anatomical cross sectional areas ACSA. The Lagrange optimisation leaded to the muscle forces $\boldsymbol{f}$

$$\boldsymbol{f} = \boldsymbol{E}^{-1}\boldsymbol{R}^T(\boldsymbol{R}\boldsymbol{E}^{-1}\boldsymbol{R}^T)^{-1}\boldsymbol{q} = \boldsymbol{R}^+\boldsymbol{q} \tag{2.9}$$

In a second step, we reduced the possible solution space to the physiological constraints from equation 2.7. This was done by an optimisation in the null space $\boldsymbol{N}$ of the matrix $\boldsymbol{R}$:

$$g_2(\boldsymbol{\mu}) = \frac{1}{2}\boldsymbol{\mu}^T(\boldsymbol{N}^T\boldsymbol{E}\boldsymbol{N})\boldsymbol{\mu} + (\boldsymbol{f}^T\boldsymbol{E}\boldsymbol{N})^T\boldsymbol{\mu} \tag{2.10}$$

where μ is a design parameter. Finally the muscle forces were:

$$\boldsymbol{f} = \boldsymbol{R}^+\boldsymbol{q} + \boldsymbol{N}\boldsymbol{\mu} \tag{2.11}$$

Implementation

The musculoskeletal shoulder model and the two muscle force estimation methods were implemented in the finite element software Abaqus® (Dassault Systèmes Simulia Corp., Providence, RI, USA). The implicit solver was used. The active contractile part of the muscle was modelled with a user defined element [Terrier et al. 2007]. This user defined element included 2 nodes per muscle unit. The element was implemented in an Abaqus user element subroutine UEL. The subroutine was called by the implicit solver at each iteration of the Newton-Raphson

algorithm. For both EMG-based and stress-based methods, the subroutine determined the contribution of the muscle element to the global stiffness matrix of the finite element method:

$$K^{MN} = -\frac{df^M}{du^N} \tag{2.12}$$

where f^M is the contribution to the residual force vector and u^N are the nodal displacements of the user element. The nodal forces and the contribution to the global stiffness matrix were then returned to the solver.

The estimation of muscle forces with the EMG-based and stress-based method was implemented in this subroutine. The subroutine provided all variables required by both methods during the movement: the position of the arm, the lines of action and the moment arms of the muscles. The lines of action of the muscles were calculated using the displacement of the pair of points associated to each muscle [Terrier et al. 2007]. The wrapping of the muscles around bony structures was taken into account in the line of action calculus. The moment arm was determined by a cross product of two vectors. The first vector was defined from the centre of the humeral head to the muscle's insertion point. The second vector was defined from the muscle's insertion point into the direction of the line of action.

The EMG-based method required experimental muscle activations $\bar{a}$ for any elevation angle. The activation was interpolated with cubic splines fitted on the experimental data. This was implemented in the fortran subroutine by using the PPPACK library [DeBoor 2001]. The minimisation problem defined in equation 2.4 was solved using the DQED library [Hanson 1986]. The obtained muscle activities were then used to calculate muscle forces using equation 2.3.

The stress-based method required a null-space algorithm of constrained quadratic programming. The pseudo-inverse of the moment arm matrix $\mathbb{R}^+$ in equation 2.9 was obtained from the moment arms. The LAPACK [Anderson et al. 1999] and BLAS [Blackford et al. 2001] libraries were used for all vector and matrix operations. The null space of $\mathbb{R}^+$ was computed by a singular value decomposition. The algorithm was based on the divide and conquer approach. The constrained optimisation problem defined in equation 2.10 was solved with the QPC solver included in the GALAHAD library [Gould et al. 2003].

2.1.3   Results

The forces of the rotator cuff muscles IS, SC, and SS were significantly lower in the stress-based method compared to the EMG-based method (Fig. 2.1.1-3). At an abduction angle of 90°, the forces of SC, SS and IS were half the magnitude for the stress-based method compared to EMG-based method. For both methods, the force of the MD increased during the elevation up to 80° and decreased afterwards (Fig. 2.1.4). For the stress-based method the force of the
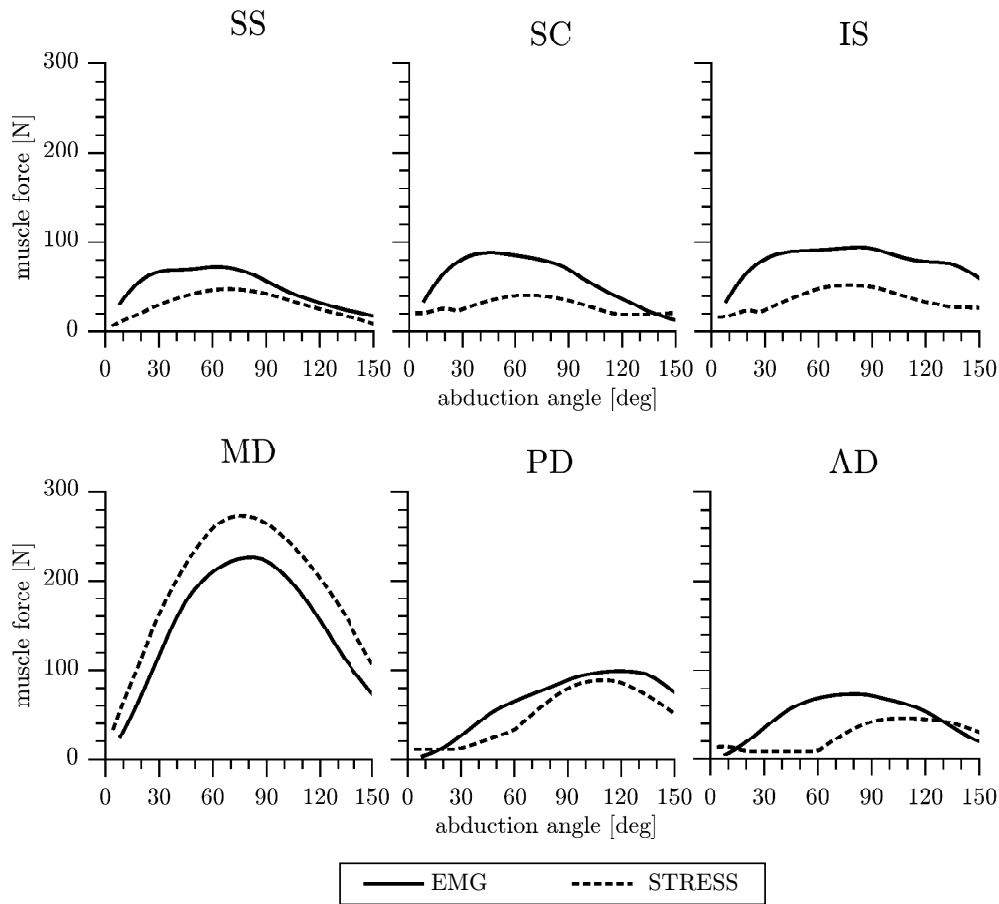
Figure 2.1 – Predicted forces for rotator cuff muscles SS, SC, IS and deltoid muscles MD, PD and AD during an abduction movement for the EMG-based and the stress-based method.

MD was higher during the whole movement. Maximum MD force was at 18 % higher for the stress-based method compared to the EMG-based method. In the stress-based method, PD and AD were inactive at the beginning of the abduction movement (Fig. 2.1.5 and 2.1.6). The stress-based method predicted lower forces for PD and AD than the EMG-based method.

For both methods, the glenohumeral load (Fig. 2.2.1) increased during the elevation up to about 90 degrees and decreased thereafter. Maximum values of 65% BW (stress-based) and 75% BW (EMG-based) were observed at 92° (stress-based) and 87° (EMG-based) abduction respectively.

The stress-based method predicted a more eccentric articular contact than the EMG-based method. The contact area was 59 mm^2 for the stress-based method and 62 mm^2 for the EMG-based method at 90° abduction (Fig. 2.3). The contact pressure reached 17 MPa with the stress-based method and 18 MPa with the EMG-based method.
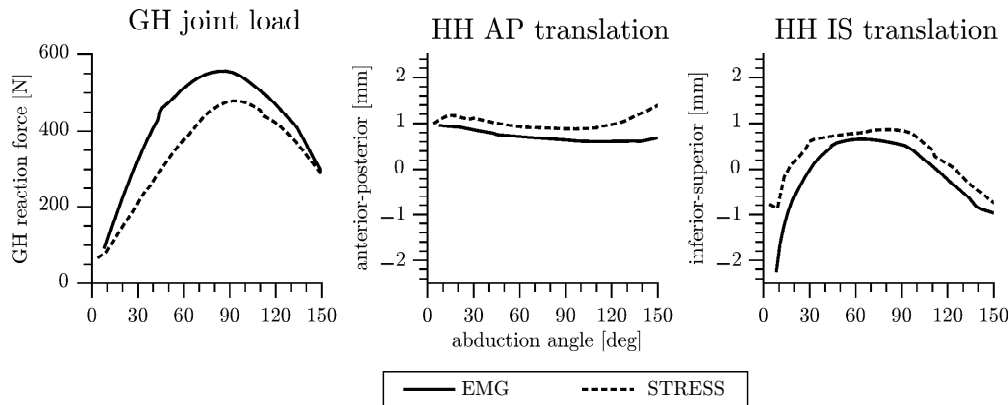
Figure 2.2 – Glenohumeral joint load, anterior-posterior and inferior-superior humeral head translations estimated with the EMG-based and the stress-based method.
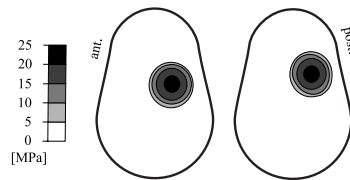
Figure 2.3 – Glenohumeral contact pressure at 90° of abduction for the EMG-based (left) and the stress-based (right) method.

In both methods, the humeral head was situated in a posterior position on the glenoid implant during the whole movement (Fig. 2.2.2). In both methods, we observed a translation from an initial inferior position to a superior position from 0° to 90° of abduction (Fig. 2.2.3). After 90° abduction, the humeral head descended again. For the stress-based method, the humeral head was in a more eccentric position throughout the whole movement compared to the EMG-based method.

2.1.4 Discussion

In this study, two widely used muscle force estimation methods were implemented and compared. The EMG-based method is using experimental EMG data as reference. The stress-based method is using a constrained optimisation algorithm related to a stress-based hypothesis. Both methods were implemented within the same musculoskeletal shoulder model, to allow a direct comparison of muscle forces and joint stability during an abduction movement. Both method predicted the same tendencies, but the co-contraction of rotator cuff muscles was underestimated in the stress-based method, decreasing their stabilizing action compared to the EMG-based method.

The stress-based method minimised rotator cuff activity as these muscles have less contribution to the abduction movement than the deltoid muscles. In contrast, the MD, who has the largest moment arm for an abduction movement, was favoured by the stress-based method. The AD and PD had negative moment arms at the beginning of the abduction and were therefore not activated until they became agonists. The underestimation of rotator cuff activity explained mainly the reduced joint loading. Both models showed a superior-posterior shift of the humeral head, but it was exaggerated by the stress-based method. This was related to both reduced rotator cuff activity and higher MD force, which pulled the humeral head in the superior-posterior direction. Consequently, the articular contact was also situated in a more superior-posterior position in the stress-based method.

Several stress-based methods are reported [Erdemir et al. 2007]. In the Delft shoulder model [van der Helm 1994a], the forces of SS, SC, IS, MD, AD and PD were smaller than in the present study. Nevertheless, the evolution of muscle forces during the abduction showed similar pattern. In the stress-based model of Yanagawa et al. [2008], the SS was active throughout the whole movement. Its force was in the same range as our stress-based prediction. Their SC force rose after 75° abduction while our methods predicted decreasing SC force in the second half of the abduction movement. Their IS force was twice as high as our stress-based method. Their MD force was 80 N higher than our stress-based method. Another study calculated muscle forces for glenohumeral abduction up to 80° glenohumeral elevation [Favre et al. 2012]. The muscle forces were evaluated with an iterative algorithm according to their ability to counteract external loads. Rotator cuff activity was regulated by a stability criteria. Rotator cuff activity was higher than in our stress-based method. The MD force was in the same range as our results. In contrast the AD force was much lower in our simulations. The PD force peaks at the end of the movement were not observed in our stress-based model.

Most shoulder models predicted a maximum muscle and joint reaction force when the arm is in an horizontal position, corresponding to the maximum torque produced by the arm weight. This prediction seems however to be contradicted by recent in vivo measurements [Bergmann et al. 2011]. Since then, other models have predicted this continuous increase [Favre et al. 2009].

Only few experimental in-vivo studies measured the humeral head translation. These studies used radiography [Poppen and Walker 1976], open MRI [Graichen et al. 2000], CT fluroscopy [Nishinaka et al. 2008] or MRI fluroscopy techniques [Massimini et al. 2012]. Most studies reported an initial inferior position of the humeral head followed by an upward migration during the first phase of abduction and a downward displacement of the humeral head during the second phase of abduction [Poppen and Walker 1976, Graichen et al. 2000, Massimini et al. 2012]. Only Nishinaka et al. [2008] reported a continuous upward migration during the whole movement. For anterior-posterior translation, Poppen and Walker [1976], Graichen et al. [2000] and Massimini et al. [2012] reported an initial anterior position followed by a posterior migration. After 90° abduction the humeral head moved forward again [Poppen and

Walker 1976, Graichen et al. 2000]. Our numerical results are consistent with these in-vivo measurements.

The only other musculoskeletal model that considered humeral head translation [Favre et al. 2012] uncoupled humeral head translation from muscle force estimation. Although this model did not continuously update the muscle action lines and moment arms associated to humeral head translation, it also predicted an upward migration of the humeral head followed by a descent in the second half of the abduction movement. This study also reported lower anterior-posterior translations than superior-inferior translations.

The strength of the present paper was to compare two different methods of muscle force prediction within the same musculoskeletal model. The following limitations are still to be discussed. The EMG data was measured on 5 healthy volunteers [Kronberg et al. 1990], but used in a model representing a shoulder joint after TSA. Nevertheless this data was choosen, because EMG measurements on patients after TSA usually show pathologic muscle activation patterns caused by longterm course of disease. Further the EMG data was not used to explicitly predict muscle forces, but rather to replicate patterns of muscular activity. The EMG-based method was then only compared to one constraint optimization method using a stress-based cost function. The choice between force and stress-based cost functions seems however to have little influence on the results [van der Helm 1994b, Buchanan and Shreeve 1996]. No additional stability criteria was implemented within the two method proposed here, as it is done in other models [van der Helm 1994b, Favre et al. 2009, Engelhardt et al. 2012]. Actually, the present model allows the translation of the humeral head, and naturally guarantees its stability through the compressive wrapping of the muscles. To reduce the degree of indeterminacy, only 6 muscles were included in the model, divided into 10 muscle units. The choice included the deltoid muscles, as they are the main actors for the abduction movement, and the rotator cuff muscles, which are the main stabilizers of the glenohumeral joint. But even if more muscles are included into the muscle, the middle deltoid will still have the greated moment arm to perform the abduction movement and will therefore be favored by the stress-based method. The EMG-based method may show different results: in this work the contribution of other muscles are not considered.

In conclusion, although both the EMG-based and stress-based methods predicted muscle forces in the same range, the analysis of shoulder prostheses might be limited especially with stress-based models. The unique framework presented here might be helpful to further improve stress-based models by adjusting the activity of stabilizing rotator cuff muscle.

2.2 An Upper Limb Model for Muscle Force Estimation

2.2.1 Introduction

The shoulder plays a crucial role in all activities of arm and hand. To investigate its functionality, several musculoskeletal models of the shoulder and the upper limb have been developed [Erdemir et al. 2007]. Amongst others the Delft Shoulder and Elbow Model [van der Helm 1994b], the Swedish Model [Högfors et al. 1987], the Visible Human Project Model [Garner and Pandy 1997; 2000], the AnyBody Model [Damsgaard et al. 2006] and the Opensim Model [Holzbaur et al. 2005].

All models mentioned in the paragraph above were developed with the objective to solve the muscle coordination problem of the shoulder for a given movement. Calculating muscle and joint reaction forces of the shoulder is a complicated task due to the complex kinematics of the underlying skeletal system, the mechanical overactuation and the elaborated muscle geometry [Erdemir et al. 2007, Ingram 2015]. To approach the problem in a manageable way, three simplifications are usually applied.

First, the bones of the skeletal system are rigid bodies and are linked through ideal ball-and-socket joints. This hypothesis does not only simplify the mechanical system to a kinematic chain but also allows the use of inverse dynamic methods. Without taking into account the unknown joint translations, the motion of the skeletal system can be planned in advance [Maurel 1999]. However, a certain error by not respecting changes in moment arms due to joint translation is implied. Further, instability problems of joints such as luxations during movements can not be simulated. One way to evaluate the glenohumeral stability anyway, is to analyse the direction of glenohumeral reaction forces. As long as the reaction force points onto the glenoid surface, the joint is considered to be stable [van der Helm 1994b].

The second common simplification is to reduce the number of muscles included in the model. The number of muscle compartments varies from six [Terrier et al. 2007] to 50 [Holzbaur et al. 2005]. The implementable number of muscles depends on the level of detail and the computational cost of the used muscle model. Thus a common trend is to use simple geometric muscle models to be able to add as much muscles as possible to the musculoskeletal model [Erdemir et al. 2007].

This part of the work deals with the improvement of an existing musculoskeletal shoulder model, which has been developed at the Automatic Control Laboratory at EPFL [Ingram 2015]. It was based on the Visible Human Project data [Garner and Pandy 1997; 2000]. The original model included thorax, clavicle, scapula and humerus spanned by 16 muscles. In a first step, it has been rebuild based on in vivo MRI images of a young healthy volunteer. The model has been extended by the forearm, ulna and radius, and the muscles spanning from scapula and humerus to the forearm bones. Then, muscle origin and insertion areas were interpolated with spline curves, on which origin and insertion points of the muscle cables were evenly distributed. This technique allowed to represent muscle segments with more than one muscle

cable. Finally, a stability constraint of the glenohumeral joint was implemented to ensure that glenohumeral reaction forces do not provoke a luxation of the joint. For validation purposes, we further recorded simultaneously arm kinematics and electric muscle activity (EMG) of the same volunteer during movements.

The effect of adding the forearm to the model, varying the number of muscle cables and the stability constraint on the muscle force estimation were evaluated during simulated abduction up to 120 degrees. The calculated forces were compared to the measured EMG data.

2.2.2 Extension of Existing Shoulder Model

New Anatomic Database

The anatomic database used in this work was based on in vivo MRI scans of a 27 years old male volunteer showing no sign of shoulder pathology. We developed a custom MRI protocol consisting of two three-dimensional T1-weighted sequences on a 3 Tesla MRI scanner. The first sequence was a gradient-recalled echo VIBE (TR/TE, 12.2/4.8 ms) and covered the glenohumeral joint with an isotropic resolution of 0.6 mm. The second sequence was a turbo spin-echo SPACE (TR/TE, 600/9.1ms) and covered the whole right hemithorax with an isotropic spatial resolution of 0.9 mm. We co-registered the two sequences with Amira (FEI Visualization Sciences Group).

The thorax, clavicle, scapula and humerus were reconstructed out of the MRI data. The image segmentation was performed manually using Amira. The resulting triangular surfaces were imported into Geomagic (3D Systems, USA) for surface optimization and smoothing. The CAD software Solidworks (Dassault Systèmes, France) was used to convert the surfaces into 3D bodies. The 3D bodies were superposed to the MRI images for visual verification.

The original shoulder model [Ingram 2015] was rebuild using the new anatomic dataset and following the instructions from Garner and Pandy [1997; 2000]. In the following it is referred to as "Shoulder Model".

Adding the Forearm

The original model has been extended by the forearm. As ulna and radius were not completely shown on the MRI data, their dimensions was estimated using anthropological data [Pearsall and Reid 1994]. The weight of the forearm was also taken from this study. The local reference frames of the forearm were defined following the ISB recommendations [Wu et al. 2005]. The elbow was modelled as hinge joint with one degree of freedom. Pronation and supination of the forearm were not implemented. Ten muscles spanning from scapula or humerus to the forearm were added: triceps brachii, biceps, brachialis, brachioradialis, supinator, pronator teres, flexor carpi radialis, flexor carpi ulnaris, extensor carpi radialis, and extensor carpi
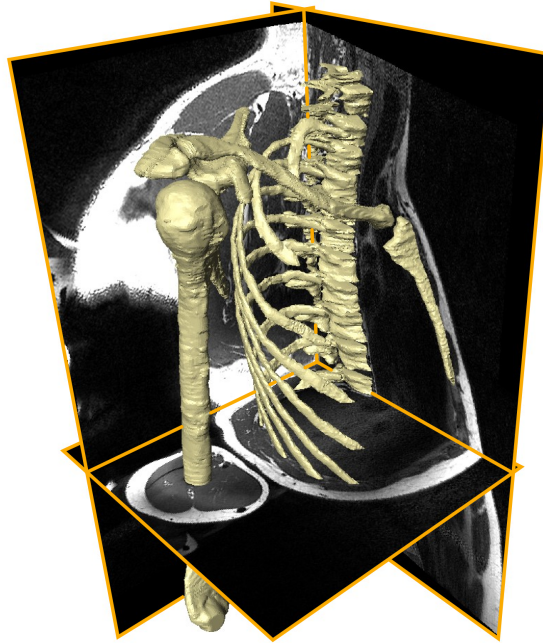
Figure 2.4 – Reconstruction of thorax, clavicle, scapula and humerus out of in vivo MRI images.

ulnaris. Origin and insertion areas of the muscles were identified with the help of the MRI data and anatomic atlases [Schünke et al. 2007, Netter 2015].

The origin and insertion areas of the muscles were interpolated with hermite cubic splines. The special case of Catmull-Rom splines was used. This type of splines allows the construction of a cubic two segment spline with three control points P_1, P_2, P_3 by using the following parameterised form:

$$
\begin{bmatrix} x(u) & y(u) & z(u) \end{bmatrix} = \begin{bmatrix} u^3 & u^2 & u & 1 \end{bmatrix} \begin{bmatrix} -s & 2-s & s-2 & s \\ 2s & s-3 & 3-2s & -s \\ -s & 0 & s & 0 \\ 0 & 1 & 0 & 0 \end{bmatrix} \begin{bmatrix} P_{1x} & P_{1y} & P_{1z} \\ P_{1x} & P_{1y} & P_{1z} \\ P_{2x} & P_{2y} & P_{2z} \\ P_{3x} & P_{3y} & P_{3z} \end{bmatrix} \quad (2.13)
$$

The three control points for the spline interpolation of each origin and insertion area were visually placed on the reconstructed bones using the Amira software, so that the spline traversed the origin respectively insertion area along its largest expansion. The origin and insertion points for the muscle cables were then evenly distributed on the spline, by dividing the arc length of the spline into sections of equal length corresponding to the chosen number of cables per muscle.
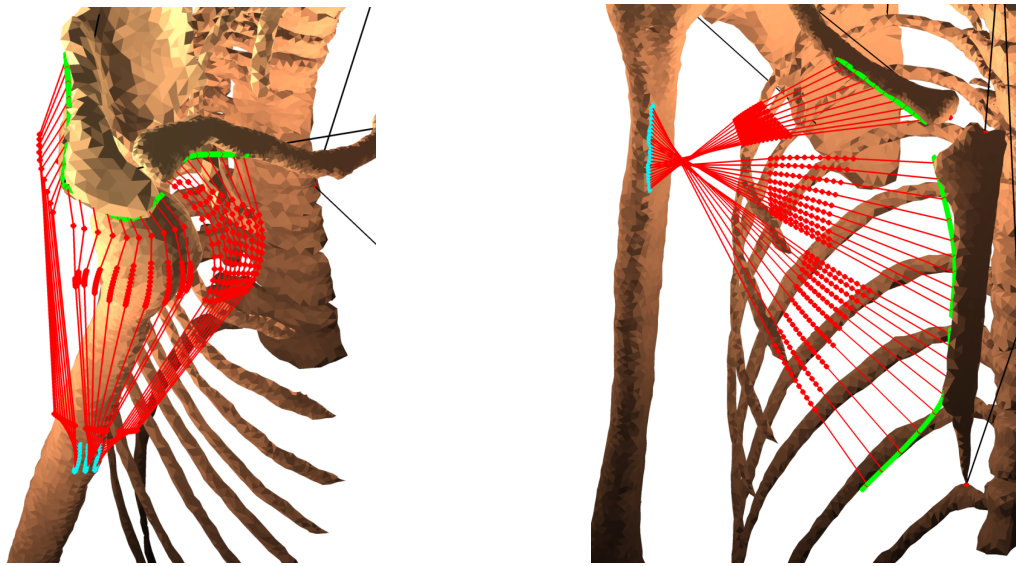
Figure 2.5 – Modelling the three Deltoid muscles and the three Pectoralis muscles and with 10 cables each. Origin and insertion area are interpolated with cubic Catmull-Rom splines. The twisted path of the Pectoralis in a rest position is correctly reproduced.

The muscle cables were guided by cylinders to reproduce the centroid lines of the muscles following the obstacle set approach [Garner and Pandy 2000]. The final placement of origin, wrapping cylinder and insertion was visually verified by superposing to the MRI images.

The model with the forearm is referred to as "Upper Limb Model" (ULM) in the following text.

EMG and Kinematics

The electric muscle activity of six shoulder muscles, anterior deltoid, middle deltoid, posterior deltoid, trapezius, teres major and pectoralis, was recorded simultaneously during an abduction movement in the scapula plane with the same volunteer as for the anatomic dataset (sec. 2.2.2). The measurement was done at the Institute of Sports Studies of the University of Lausanne.

The acquisition system was the Biopac MP150 (www.biopac.com). We used pairs of silver chloride (Ag-AgCl) circular (recording diameter: 1 cm) surface electrodes (Kendall Meditrace 100, Tyco) positioned lengthwise over the muscle belly with an interelectrode (center-to-center) distance of 2 cm. The reference electrode was placed on the lower back. The electrodes were placed following a standard surface electrode placement protocol [Perotto and Delagi 2011]. The placement of the electrodes was verified by activating the muscles. At first, voluntary maximum isometric contractions were measured for the six muscles. This was done two times with a five minutes break in between. During the contraction, the volunteer was kept cheering on. After another five minutes break, the volunteer did two slow abductions in the scapula

plane from a rest position up to 180 °. The abduction movement was tracked during the movement with a 3D accelerometer (Biopac BioNomadix).

The EMG signals were recorded using the Biopaq 4.2 software with a sample rate of 2000 Hz. The data was imported into Matlab for post processing. The EMG signals were high pass filtered with a cut off frequencies of 25 Hz to remove movement artefacts. Then, the signals were full-wave rectified and time averaged over a time span of 250 ms. Finally, the signals were normalized to the maximum voluntary activation measured previously.

The measured kinematics were imported into Matlab to reproduce the same abduction movement with the upper limb model.

Muscle Force Coordination and Glenohumeral Stability

Solving the muscle force coordination problem for a given movement means the calculation of muscle force intensities and their temporal evolution needed to perform the desired movement [Ingram 2015]. The movement was defined through the joint rotation angles and their first and second derivatives over time. With the given joint positions, velocities and accelerations, the dynamic model can be inverted and the torque at each joint is obtained. The resulting system of equations is undetermined with an infinite number of solutions, meaning that there are infinite combinations of muscle activations to produce the required joint torque. In a first step, one solution has been chosen following a cost function. This first interim solution minimised the squared muscle stresses:

$$\min g_1(\boldsymbol{f}) \text{ with: } g_1(\boldsymbol{f}) = \sqrt{\frac{1}{n}\sum_{i=0}^{n}\left(\frac{f_i}{A_i}\right)^2} \tag{2.14}$$

where $\boldsymbol{f}$ was a vector containing the muscle forces, the number of muscles n, and the muscles cross sectional area A. A second optimisation process delt with the stability of the glenohumeral joint. The cost function g_2 minimised the deviation of the glenohumeral reaction force from the center of the glenoid cavity. We defined a local coordinate system GH with origin in the rotational center of the glenohumeral joint and the z axis pointing from the rotational center of the glenohumeral joint to the center of the glenoid cavity. The glenohumeral joint reaction force vector $\boldsymbol{f}_{RF}$ was normalized $\|\boldsymbol{f}_{RF}\|$ and transformed into the local coordinate system $\|\boldsymbol{f}_{RF}\|_{GH}$. The deviation of the joint reaction force from the center of the glenoid cavity was thus given by the x and y components of $\|\boldsymbol{f}_{RF}\|_{GH}$. The second optimisation was defined as follows:

$$\min g_2(\boldsymbol{f}) \text{ with: } g_2(\boldsymbol{f}) = \alpha\sqrt{\|\boldsymbol{f}_{RF}\|_{GHx}^2 + \|\boldsymbol{f}_{RF}\|_{GHy}^2} \tag{2.15}$$

with a parameter α to adjust the severity of the cost function. In a third optimisation, both cost functions were linked following the principles of multicriteria optimisation [Bui and Alam 2008]:

$$\min g_3(g_1, g_2) \text{ with: } g_3(g_1, g_2) = (g_1 - g_{1min})^2 + (g_2 - g_{2min})^2 \tag{2.16}$$

where g_{1min} and g_{2min} are the minimum values of g_1 and g_2 obtained during the previous optimisation steps.

The muscle forces for the recorded abduction movement were estimated three times: first, the upper limb model with one cable per muscle segment. Second, the upper limb model with three cables per muscle segment. And third, the upper limb model with three cables per muscle segment and the stability constraint. The obtained muscle forces were normalized to the theoretical maximum muscle force of each muscle [Garner and Pandy 2000].

2.2.3 Results

The recorded EMG data showed increasing activity of the deltoid muscles up to 90 °abduction, before it slightly decreased to the end of the movement. Trapezius, pectoralis and teres major showed increasing activity over the whole movement (Figure 2.7).

The upper limb model with one cable per muscle (Figure 2.6, left column) predicted no activity of the anterior deltoid. Middle and posterior deltoid were active during the whole movement. Infraspinatus stayed inactive. Supraspinatus was active during the first half of the movement with a maximum activity of 3%. The subscapularis muscle was active throughout the movement. The joint reaction force increased from 0 to 100 degrees of abduction up to 440N (Figure 2.8, left). The joint reaction force pointed initially in superior-anterior direction and moved inferiorly during the movement (Figure 2.9, left).

The upper limb model with three cables per muscle (Figure 2.6, middle column) predicted increasing activity for all deltoid muscles. Infraspinatus showed no activity. The supraspinatus was active up to 90°abduction. The subscapularis force increased throughout the movement. The joint reaction force (Figure 2.8, middle) increased throughout the movement up to 345 N. The joint reaction force pointed initially in superior-anterior direction and moved inferiorly during the movement (Figure 2.9, middle).

The upper limb model with three cables per muscle and the stability constraint (Figure 2.6, right column) predicted increasing activity for all deltoid muscles. Infraspinatus was active up to 90°abduction. Supraspinatus and subscapularis were active throughout the movement. The joint reaction force (Figure 2.8, right) increased throughout the movement up to 390 N.

Estimated Muscle Forces
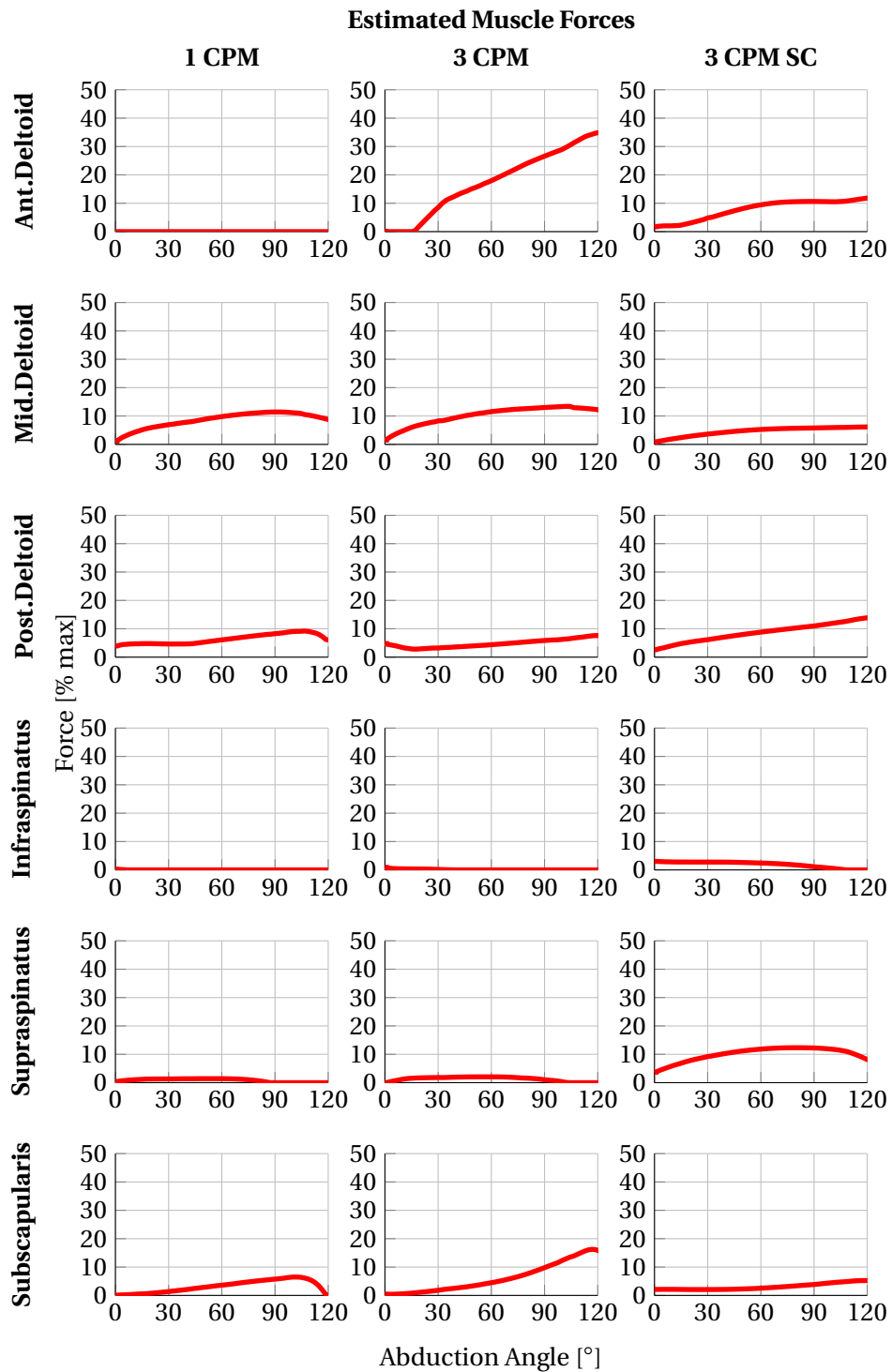
Figure 2.6 – Comparison of muscle force estimations from left to right: upper limb model with one cable per muscle segment (1 CPM), with three cables per muscle segment (3 CPM) and with three cables per muscle segment and stability constraint (3 CPM SC).

Comparison EMG - Muscle Forces
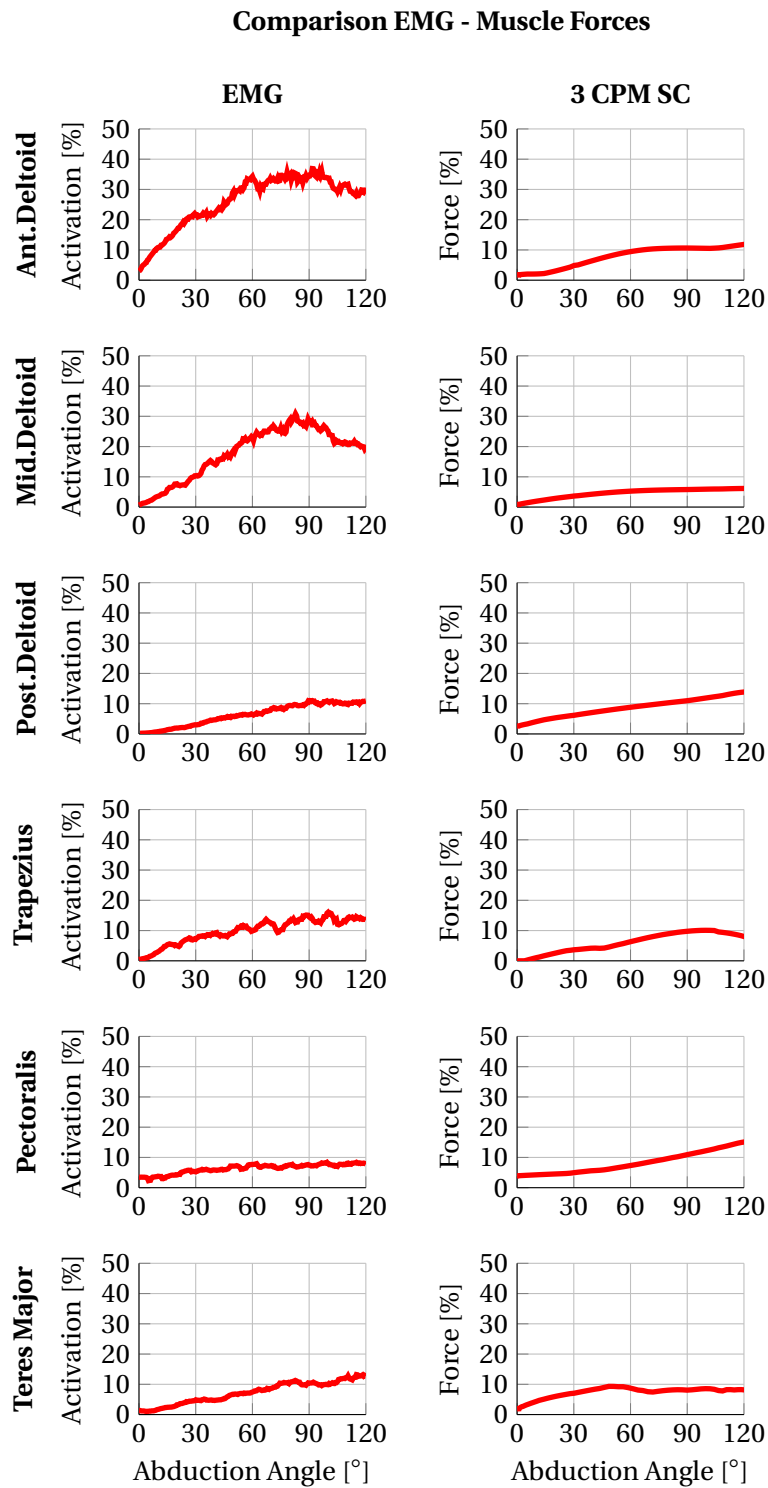
Figure 2.7 – Comparison of EMG measurements of six shoulder muscles during abduction in the scapula plane with the estimated muscle forces of the upper limb model with three cables per muscle segment and stability constraint. The muscle activation was normalized to a maximum voluntary contraction. The muscle force was normalized to the muscle's theoretical maximum force.

Joint Reaction Force
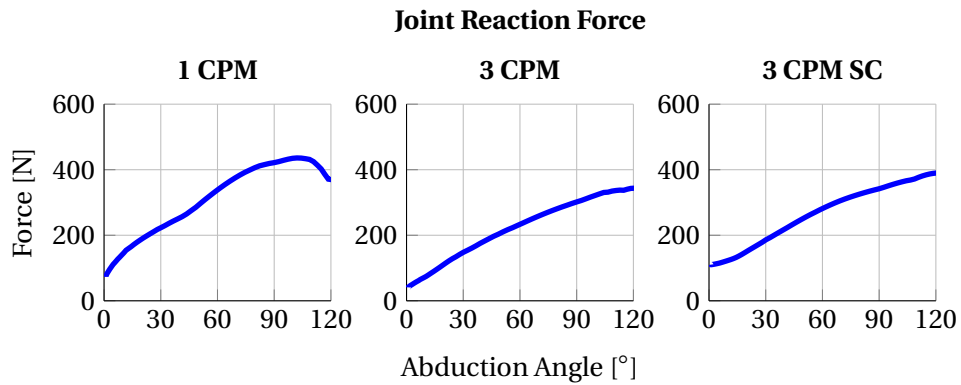
Figure 2.8 – Comparison of joint reaction forces from left to right: upper limb model with one cable per muscle segment (1 CPM), with three cables per muscle segment (3 CPM) and with three cables per muscle segment and stability constraint (3 CPM SC).

Glenohumeral Stability
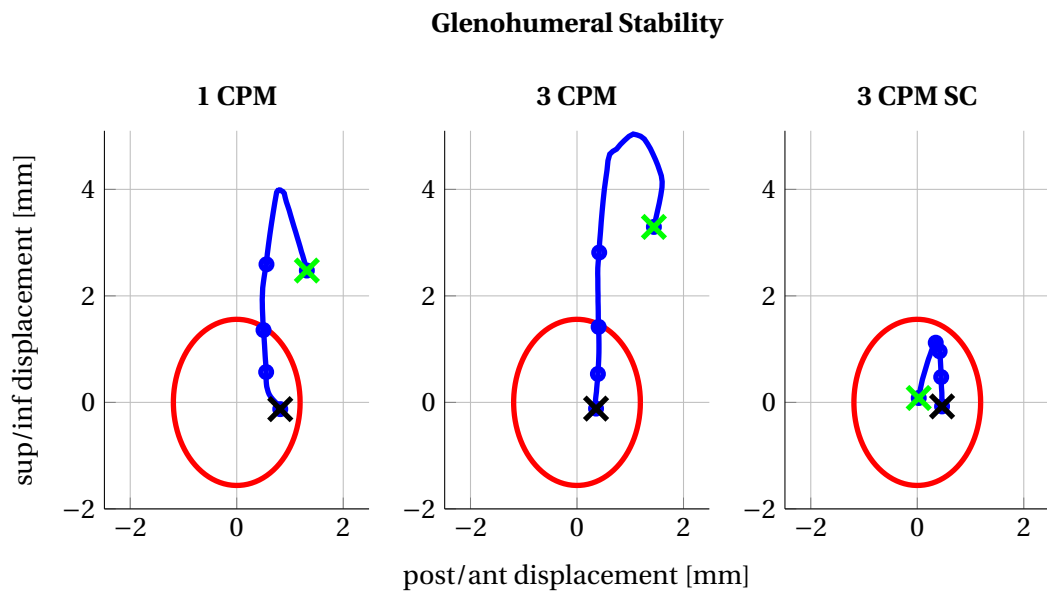
Figure 2.9 – Comparison of joint stability from left to right: upper limb model with one cable per muscle segment (1 CPM), with three cables per muscle segment (3 CPM) and with three cables per muscle segment and stability constraint (3 CPM SC). The direction of the joint reaction force is projected on the glenoid cavity.

The joint reaction force was centered on the glenoid at the beginning of the movement, moved superiorly during the first 30°of abduction, and then moved inferiorly (Figure 2.9, right).

2.2.4 Discussion

Estimating the muscle coordination in the shoulder and calculating joint reaction forces is a difficult task. The complexity of skeletal kinematics and muscle interplay force researchers to use simplifications to reduce the complexity to a manageable level. An existing shoulder model, which was built using the three general simplifications of reducing the skeleton to a rigid body kinematic chain, reducing the number of muscles, and modeling muscles as cables, was the starting point of this work. The model was then improved in three major points: the forearm with the muscles spanning to it were included, muscle origin and insertion sites were interpolated with splines to allow muscle representation with several cables, and the stability of the glenohumeral joint was surveyed with a stability constraint. The different stages of development were tested and compared for an abduction movement in the scapular plane.

In this study, we used patient specific MRI data to build the geometric model. However, the muscles' physiologic parameters were taken from the Visible Human Project [Garner and Pandy 2000]. Within the scope of this project, it was not possible to perform the necessary measurements on our volunteer to obtain patient specific muscle contraction parameters. We justify the use of the Visible Human Project data by the fact, that both the muscle data as well as the numerical model were derived from a young male person. Differences in muscle physiology are thus considered to be small.

The muscle force estimation results showed a common problem in musculoskeletal shoulder models: the inactivity of the anterior deltoid muscle. The EMG data proved this muscle to be active during the whole abduction movement (Figure 2.7), which has also been shown by other EMG studies [Kronberg et al. 1990]. But several musculoskeletal shoulder models have difficulties in predicting the anterior deltoid activity [Quental et al. 2015]. In this work, the problem could be solved by modelling the muscles with several cables. Indeed, more cables increase the scope of action for a muscle. This leads to a greater variation in force direction and moment arms for a single muscle depending on the partial activation of the cables. This problem did not only highlight the role of the cable number, but also the placement of their origin and insertion on the bones. Only few works could be found in literature discussing this problem, which should be further investigated [van der Helm and Veenbaas 1991, Quental et al. 2015, Ingram 2015]. Adding more cables and reviewing the origin and insertion points could however not answer the question of the low rotator cuff activity compared to EMG data [Kronberg et al. 1990]. The upper limb model with three cables per muscle and the stability constraint predicted the highest rotator cuff activity. But still infraspinatus was not active throughout the movement as predicted by EMG measurements [Kronberg et al. 1990]. Other models [van der Helm 1994b, Garner and Pandy 2000] seem to better predict rotator cuff activity. However, it is known that optimization techniques tend to underestimate stabilizing

muscle activity [Engelhardt et al. 2014]. The activity of trapezius, pectoralis and teres major was well replicated by the upper limb model (Figure 2.7).

The highest joint reaction force was predicted by the upper limb model with one cable per muscle segment. Modelling muscles with several cables seems to lead to a more efficient solution. Recalling that the cost function was the sum of squared muscle stresses, more efficient means in this context rising the arm with less muscular effort. This is visible when comparing the joint reaction forces between the 1 cable per muscle model and the 3 cable per muscle model (Figure 2.8, left and middle). The model with 3 cables per muscle and the stability constraint showed increased joint reaction forces compared to the 3 cable per muscle model (Figure 2.8, middle and right). The reason for that is the higher rotator cuff activity (Figure 2.6). Experimental measurements with instrumented prostheses were in the range of 600 to 900 N for an abduction movement [Bergmann et al. 2011]. The upper limb model predicted joint reaction forces lower than the experimental data. However, the simulated abduction was slower than the abduction in the experimental setting. The underestimation of stabilizing muscle activity in optimization methods might further contribute to a low joint reaction force estimation [Engelhardt et al. 2015].

The analysis of the direction of joint reaction forces proved that a stability constraint is necessary: the model did not predict a naturally stable solution in the sense that the glenohumeral reaction force stayed within the glenoid cavity throughout the whole movement. Especially in the first 60°of the abduction movement, the reaction force pointed anteriorly-superiorly of the glenoid cavity (Figure 2.9, left and middle). The anterior-superior shift was less in the upper limb model with one cable per muscle. The glenohumeral stability constraint managed successfully to redirect the joint reaction force onto the glenoid cavity, by increasing the rotator cuff activity (Figure 2.6). Inferior-superior stability was mainly achieved by a higher activation of the supraspinatus. Anterior-posterior stability was achieved by balancing the activity of anterior and posterior deltoid muscles and by activating the infraspinatus muscle.

It is known, that the passive structures of the shoulder do not guarantee joint stability: ligaments and joint capsule are not pre stretched in the midrange of glenohumeral motion. Only in the end range of humeral motion their passive forces increase [Lippitt and Matsen 1993, Veeger and van der Helm 2007]. The labrum is a soft ring-shaped collagen fibre bundle around the glenoid which is flexibly linked to the glenoid. A considerable stabilizing role of the labrum can thus be declined [Tischer and Putz 2003, Barthel et al. 2003, Veeger and van der Helm 2007]. Consequently active mechanisms as muscle cocontraction are more likely to guarantee joint stability in the midrange of motion. The rotator cuff muscles are predisposed for this task. Arranged around the glenoid cavity, they produce compressing forces on the joint without exerting large moments. A stability constraint as implemented in this work shows its ability to constrain the joint reaction force into the glenoid by mainly activating the rotator cuff muscles. However, the use of such a constraint remains discussable. The translation stiffness of the joint correlates with the shape of the articular contact surfaces, which were not included in this model [Peltz et al. 2015]. Further, the stabilisation of the shoulder is probably

a complex process including control and feedback mechanisms, which were not part of this work [Vangsness Jr. et al. 1995, De Vlugt et al. 2002, Veeger and van der Helm 2007, Ingram 2015].

The strength of this model was to compute muscle forces for a given movement by taking into account 42 muscles spanning the shoulder girdle. However, to be able to use an inverse dynamics approach, the skeletal system had to be simplified to a rigid body chain linked through ideal ball joints. This approach has the advantage to solve the muscle force coordination problem by reproducing the known joint torques. Computational efficient optimizations techniques can be applied. On the other hand, the a priori motion planning prevents the prediction of unknown kinematic quantities such as humeral head translations. Forward dynamic approaches are obligatory to use if kinematics are to be estimated. Further, the muscles were simplified with cables to reduce the numerical complexity. We tried to reduce the impact of this simplification on the estimated forces by modelling muscles with several cables. The problem of anterior deltoid activity could be improved by modelling each muscle with three cables. Adding more cables per muscle did not influence the result, but increased the numerical load and worsened the convergence behaviour of the optimization algorithm. The low estimated rotator cuff forces could be improved by including an EMG tracking criterion to the optimization process. To tackle the problem of occasional inactivity of certain muscles, an extensive study of origin and insertion points and resulting moment arms would be necessary [Ingram 2015]. The model could further be extended simulating other movements than the abduction.

The shoulder model presented in this chapter was constructed to estimate muscle and joint forces. The resultant muscle forces were in agreement with EMG measurements. The concept is such promising. However, the use of the muscle cable model should be studied further. The influence of the number of cables and their placement in the ensemble of shoulder muscles on the results need further investigation.

2.3   Conclusion

Solving the muscle coordination problem in musculoskeletal joint models remains a challenging task. The difficulty lies in the overdetermined multi body mechanism coupled with complex muscle behaviour. In the first part of this chapter, two widely used force estimation algorithms, EMG tracking and inverse dynamics coupled with optimization, were implemented and compared. Although the EMG tracking method was found to better replicate stabilizing muscle activity, the upper limb model presented in the second part of this chapter was designed for use with inverse dynamics and null space optimization. The choice was motivated by the flexibility of optimization techniques: they do not require EMG data and can thus be employed for any movement with known kinematics. Future works in the field of inverse dynamics models for muscle force estimation should tackle the problem of muscle cable positioning, which has been found to have a great impact on obtainable solutions. To overcome

the simplified kinematic rigid body chain for prediction of kinematic quantities, methods have to be developed that do not rely on a priori motion planning. A possible approach inspired by cable driven robotics could be a forward dynamic model used with reinforcement learning strategies.

Although we can nowadays predict muscle and joint forces that are in agreement with experimental data, we still do not understand all the control mechanisms fulfilled actively by the neural network and passively by the properties of muscle connective tissues. To take into accounts these control aspects in the muscle coordination problem will require further common research from neuroscience to numerical modelling.

The musculoskeletal model will be used in the scope of a parametric study to analyse the effect of anatomic parameters on predicted muscle and joint forces (Chapter 5).

2.B Bibliography

Anderson E., Bai Z., Bischof C., Blackford S., Demmel J., Dongarra J., Croz J. D., Greenbaum A., Hammarling S., McKenney A., and Sorensen D.: *LAPACK Users' Guide*. SIAM, Philadelphia, PA, 1999.

Barthel T., König U., Böhm D., Loehr J. F., and Gohlke F.: Die anatomie des labrum glenoidale. *Der Orthopäde*, 32(7):578–585, 2003.

Bergmann G., Graichen F., Bender A., Rohlmann A., Halder A., Beier A., and Westerhoff P.: In vivo gleno-humeral joint loads during forward flexion and abduction. *J Biomech*, 44: 1543–1552, 2011.

Blackford L. S., Demmel J., Dongarra J., Duff I., Hammarling S., Henry G., Heroux M., Kaufman L., Lumsdaine A., Petitet A., Pozo R., Remington K., and Whaley R. C.: An updated set of basic linear algebra subprograms (blas). *ACM T. Math. Software*, 28:135–151, 2001.

Buchanan T. S. and Shreeve D. A.: An evaluation of optimization techniques for the prediction of muscle activation patterns during isometric tasks. *J Biomech Eng*, 118(4):565–574, 1996.

Bui L. T. and Alam S.: An introduction to multi-objective optimization. *Multi-Objective Optimization in Computational Intelligence: Theory and Practice*, pages 1–19, 2008.

Charlton I. W. and Johnson G. R.: A model for the prediction of the forces at the glenohumeral joint. *Proc Inst Mech Eng H*, 220(8):801–812, 2006.

Cholewicki J., McGill S. M., and Norman R. W.: Comparison of muscle forces and joint load from an optimization and EMG assisted lumbar spine model: Towards development of a hybrid approach. *J Biomech*, 28(3):321–331, 1995.

Damsgaard M., Rasmussen J., Christensen S. T., Surma E., and de Zee M.: Analysis of musculoskeletal systems in the anybody modeling system. *Simulation Modelling Practice and Theory*, 14(8):1100–1111, 2006.

De Vlugt E., Schouten A. C., and van der Helm F. C. T.: Adaptation of reflexive feedback during arm posture to different environments. *Biological Cybernetics*, 87(1):10–26, 2002.

DeBoor C.: *A Practical Guide to Splines*. Springer, Berlin, 2001.

Engelhardt C., Ingram D., Müllhaupt P., Pralong E., Farron A., Pioletti D., and Terrier A.: Solving overconstrained kinematic in numerical shoulder model using nullspace optimization. *10th International Symposium CMBBE*, 2012.

Engelhardt C., Farron A., Becce F., Pioletti D., and Terrier A.: Impact of partial-thickness tears on supraspinatus tendon strain based on a finite element analysis. *Computer Methods in Biomechanics and Biomedical Engineering*, 17(SUPP1):118–119, 2014.

Engelhardt C., Camine V. M., Ingram D., Muellhaupt P., Farron A., Pioletti D., and Terrier A.: Comparison of an EMG-based and a stress-based method to predict shoulder muscle forces. *Comp Methods Biomech Biomed Engin*, 18(12):1272–1279, 2015.

Erdemir A., McLean S., Herzog W., and van den Bogert A. J.: Model-based estimation of muscle forces exerted during movements. *Clin. Biomech.*, 22(2):131–154, 2007.

Favre P., Snedeker J. G., and Gerber C.: Numerical modelling of the shoulder for clinical applications. *Philos. Trans. R. Soc.*, 367:2095–2118, 2009.

Favre P., Senteler M., Hipp J., Scherrer S., Gerber C., and Snedeker J. G.: An integrated model of active glenohumeral stability. *J Biomech*, 45(13):2248–2255, 2012.

Gagnon D., Larivière C., and Loisel P.: Comparative ability of EMG, optimization, and hybrid modelling approaches to predict trunk muscle forces and lumbar spine loading during dynamic sagittal plane lifting. *Clinical Biomechanics*, 16(5):359–372, 2001.

Garner B. A. and Pandy M. G.: A kinematic model of the upper limb based on thevisible human project (vhp) image dataset. *Comput Methods Biomech Biomed Engin*, 2:107–124, 1997.

Garner B. A. and Pandy M. G.: Musculoskeletal model of the upper limb based on the visible human male dataset. *Comput Methods Biomech Biomed Engin*, 4:93–126, 2000.

Gould N. I. M., Orban D., and Toint P. L.: Galahad, a library of thread-safe fortran 90 packages for large-scale nonlinear optimization. *ACM Trans. Math. Softw.*, 29(4):353–372, 2003.

Graichen H., Stammberger T., Bonel H., Englmeier K.-H., Reiser M., and Eckstein F.: Glenohumeral translation during active and passive elevation of the shoulder - a 3D open-MRI study. *J Biomech*, 33(5):609–613, 2000.

Hanson R. J.: Linear least squares with bounds and linear constraints. *SIAM J. Sci. Stat. Comp.*, 7(3):826–834, 1986.

Happee R. and van der Helm F. C. T.: The control of shoulder muscles during goal directed movements, an inverse dynamic analysis. *J Biomech*, 28(10):1179–1191, 1995.

Högfors C., Peterson B., and Herberts P.: Biomechanical model of the human shoulder - I. elements. *Journal of Biomechanics*, 20(2):157–166, 1987.

Holzbaur K. R., Murray W. M., and Delp S. L.: A model of the upper extremity for simulating musculoskeletal surgery and analyzing neuromuscular control. *Ann Biomedical Engineering*, 33(6):829–840, 2005.

Ingram D., Müllhaupt P., Terrier A., Pralong E., and Farron A.: Dynamical biomechanical model of the shoulder for muscle-force estimation. *Proceedings of the IEEE RAS-EMBS International Conference on Biomedical Robotics and Biomechatronics*, pages 407–412, 2012.

Ingram D.: *Musculoskeletal Model of the Human Shoulder for Joint Force Estimation.* PhD thesis, EPFL, Lausanne, 2015.

Karlsson D. and Peterson B.: Towards a model for force predictions in the human shoulder. *Journal of Biomechanics*, 25(2):189–199, 1992.

Kronberg M., Nemeth G., and Brostrom L.-A.: Muscle activity and coordination in the normal shoulder. an electromyographic study. *Clin. Orthop. Relat. Res.*, 257:76–85, 1990.

Langenderfer J., Jerabek S. A., Thangamani V. B., Kuhn J. E., and Hughes R. E.: Musculoskeletal parameters of muscles crossing the shoulder and elbow and the effect of sarcomere length sample size on estimation of optimal muscle length. *Clin. Biomech.*, 19:664–670, 2004.

Langenderfer J. E., LaScalza S., Mell A., Carpenter J. E., Kuhn J. E., and Hughes R. E.: An EMG-driven model of the upper extremity and estimation of long head biceps force. *Comp. in Bio. and Med.*, 35(1):25–39, 2005.

Lin H.-T., Su F.-C., Wu H.-W., and An K.-N.: Muscle forces analysis in the shoulder mechanism during wheelchair propulsion. *Proceedings of the Institution of Mechanical Engineers, Part H: Journal of Engineering in Medicine*, 218(4):213–221, 2004.

Lippitt S. and Matsen F.: Mechanisms of glenohumeral joint stability. *Clinical Orthopaedics and Related Research*, (291):20–28, 1993.

Lloyd D. G. and Besier T. F.: An EMG-driven musculoskeletal model to estimate muscle forces and knee joint moments in vivo. *Journal of Biomechanics*, 36(6):765–776, 2003.

Massimini D., Boyer P., Papannagari R., Gill T., Warner J., and Li G.: In-vivo glenohumeral translation and ligament elongation during abduction and abduction with internal and external rotation. *Journal of Orthopaedic Surgery and Research*, 7(1):1–9, 2012.

Maurel W.: *3D modeling of the human upper limb including the biomechanics of joints, muscles and soft tissues.* PhD thesis, EPFL, Lausanne, 1999.

McClure P. W., Michener L. A., Sennett B. J., and Karduna A. R.: Direct 3-dimensional measurement of scapular kinematics during dynamic movements in vivo. *J. Shoulder Elbow. Surg.*, 10:269–277, 2001.

Netter F. H.: *Atlas of Human Anatomy.* Elsevier, 2015. ISBN 978-3-437-41605-7.

Nikooyan A. A., Veeger H. E. J., Westerhoff P., Bolsterlee B., Graichen F., Bergmann G., and van der Helm F. C. T.: An EMG-driven musculoskeletal model of the shoulder. *Human Movement Science*, 31(2):429–447, 2012.

Nishinaka N., Tsutsui H., Mihara K., Suzuki K., Makiuchi D., Kon Y., Wright T. W., Moser M. W., Gamada K., Sugimoto H., and Banks S. A.: Determination of in vivo glenohumeral translation using fluoroscopy and shape-matching techniques. *J. Shoulder Elbow. Surg.*, 17(2):319–322, 2008.

Pearsall D. and Reid G.: The study of human body segment parameters in biomechanics. *Sports Medicine*, 18(2):126–140, 1994.

Peltz C., Zauel R., Ramo N., Mehran N., Moutzouros V., and Bey M.: Differences in glenohumeral joint morphology between patients with anterior shoulder instability and healthy, uninjured volunteers. *Journal of Shoulder and Elbow Surgery*, 24(7):1014–1020, 2015.

Perotto A. and Delagi E. F.: *Anatomical Guide for the Electromyographer: The Limbs and Trunk*. Charles C. Thomas, 2011. ISBN 9780398086497.

Poppen N. K. and Walker P. S.: Normal and abnormal motion of the shoulder. *J Bone Joint Surg Am*, 58(2):195–201, 1976.

Quental C., Folgado J., Ambrósio J., and Monteiro J.: Critical analysis of musculoskeletal modelling complexity in multibody biomechanical models of the upper limb. *Computer Methods in Biomechanics and Biomedical Engineering*, 18(7):749–759, 2015.

Schünke M., Schulte E., and Schumacher U.: *Prometheus - LernAtlas der Anatomie: Allgemeine Anatomie und Bewegungssystem*. Thieme, 2007. ISBN 978-3131395221.

Terrier A., Reist A., Vogel A., and Farron A.: Effect of supraspinatus deficiency on humerus translation and glenohumeral contact force during abduction. *Clin. Biomech.*, 22(6):645–651, 2007.

Terrier A., Aeberhard M., Michellod Y., Müllhaupt P., Gillet D., Farron A., and Pioletti D.: A musculoskeletal shoulder model based on pseudo-inverse and nullspace optimization. *Med Eng Physics*, 32:1050–1056, 2010.

Tischer T. and Putz R.: Die anatomie des oberen labrumkomplexes im schultergelenk. *Der Orthopäde*, 32(7):572–577, 2003.

van der Helm F. C. T.: Analysis of the kinematic and dynamic behavior of the shoulder mechanism. *J Biomech*, 27(5):527–550, 1994a.

van der Helm F. C. T.: A finite element musculoskeletal model of the shoulder mechanism. *J Biomech*, 27(5):551–569, 1994b.

van der Helm F. C. T. and Veenbaas R.: Modelling the mechanical effect of muscles with large attachment sites: Application to the shoulder mechanism. *Journal of Biomechanics*, 24(12):1151–1163, 1991.

Vangsness Jr. C. T., Ennis M., Taylor J. G., and Atkinson R.: Neural anatomy of the glenohumeral ligaments, labrum, and subacromial bursa. *Arthroscopy: The Journal of Arthroscopic and Related Surgery*, 11(2):180–184, 1995.

Veeger H. E. J. and van der Helm F. C. T.: Shoulder function: The perfect compromise between mobility and stability. *J Biomech*, 40(10):2119–2129, 2007.

Wu G., van der Helmb F. C. T., Veeger H. E. J., Makhsouse M., Royf P. V., Angling C., Nagelsh J., Kardunai A. R., McQuadej K., Wangk X., Wernerl F. W., and Buchholzm B.: ISB recommendation on definitions of joint coordinate systems of various joints for the reporting of human joint motion - Part II: shoulder, elbow, wrist and hand. *J Biomech*, 38:981–992, 2005.

Yanagawa T., Goodwin C. J., Shelburne K. B., Giphart J. E., Torry M. R., and Pandy M. G.: Contributions of the individual muscles of the shoulder to glenohumeral joint stability during abduction. *J Biomech Eng*, 130(2), 2008.

Yang J., Feng X., Kim J. H., and Rajulu S.: Review of biomechanical models of the human shoulder complex. *I. J. H. F. M. S.*, 1(3):271–293, 2010.

Zajac F. E.: Muscle and tendon: properties, models, scaling, and application to biomechanics and motor control. *Crit Rev Biomed Eng*, 17(4):359–411, 1989.

3 Cartilage Model

The purpose of this chapter is to present a numerical model of the glenohumeral articular contact. The model has the ability to calculate contact pressure and cartilage deformation during shoulder movements. The knowledge about these mechanical quantities is important in the context of glenohumeral osteoarthritis. The mechanical cartilage load must stay within physiological ranges to preserve the natural homeostasis of the joint. Otherwise the risk of tissue degeneration increases. To assess these variables, a numerical finite element model of the glenohumeral joint has been developed. The model takes into account the natural migration of the humeral head on the glenoid cavity and allows thus the evaluation of glenohumeral stability. It further calculates the resulting articular contact patterns, contact pressure, and cartilage deformation for a given shoulder movement.

In the overall work process of this thesis, the model relies on the results of the musculoskeletal upper limb model presented in the previous section 2.2: it takes the joint reaction forces calculated by the upper limb model as input. The estimated humeral head translations will later be used in the tendon model described in chapter 4. In chapter 5, the model will be used to evaluate the effect of anatomic parameters on cartilage load. Risk factors for osteoarthritis will then be derived from the numerical results.

3.1   Introduction

Shoulder pain is a frequent reason for consultation in orthopaedic practice. Studies report a prevalence of 25%. 30% of the affected complain about being significantly disadvantaged [Hasvold and Johnsen 1993, Pope et al. 1997]. The diagnosis osteoarthritis is one of the most common for patients suffering from pain and mobility loss. Prevalence for shoulder osteoarthritis was determined to be at 17.5% increasing with age [Kobayashi et al. 2014]. Research in this field is thus not only motivated by medical factors, but also by socio economical reasons in an ageing society.

Besides the cases where patients report a predisposing history, p.e. shoulder traumata (secondary osteoarthritis), the causes for osteoarthritis are often unknown (primary osteoarthritis). However, the pathogenic role of biomechanical dysfunction in osteoarthritis is well established [Brandt et al. 2009, Egloff et al. 2012]. In this way of thinking, osteoarthritis occurs when the dynamic balance between destructive joint wear and the joint's own repair mechanisms is disturbed [Eyre 2004, Buckwalter and Martin 2006, Helmick et al. 2008]. On the other hand, the absence of mechanical stimulation leads to a similar tissue response [Jurvelin et al. 1986, Vanwanseele et al. 2002]. On the tissue level, a loss of proteoglycans can be observed as well as a disruption of the collagenous network [Wieland et al. 2005]. When progressing further, the articular cartilage gets destroyed and worn out until the subchondral bone layers get in contact. At this stage, only a total shoulder arthroplasty can relieve the patient from pain and restore joint mobility.

The importance of joint motion, with its related cartilage loading for both cartilage maintenance and cartilage repair, is nowadays well accepted [Brand 2005]. This knowledge motivated several studies to analyse the right dosage of the mechanical stimulus. A series of in vitro studies proved, that cartilaginous cells increase their production of cartilage matrix proteins when intermittently loaded with hydrostatic pressures in the range of 7-10 MPa [Grad et al. 2011]. Continuous constant pressure in contrast was shown to be unsuitable for cartilage stimulation [Elder and Athanasiou 2009]. It has also been shown that cyclic compressive loading of 6.8 MPa significantly increased the collagen production compared to cartilage under cyclic loading with 3.4 MPa and to unloaded cartilage [Carver and Heath 1999]. The result suggests that a minimum load for tissue stimulation is necessary.

Several studies tried to assess physiological contact pressure by measuring articular pressure during movements. Experimental in vivo studies using a hip hemiprosthesis measured articular contact pressures up to 20 MPa [Hodge et al. 1986]. In vivo MRI studies have also shown that cartilage in the lower limb can undergo compressive strains up to 45% under static loading [Armstrong et al. 1979, Herberhold et al. 1999, Eckstein et al. 2006]. A cadaveric shoulder study measured peak pressures of 10 MPa using pressure sensitive films [Conzen and Eckstein 2000].

The compressive failure of articular cartilage initiates at 20-30 MPa where significant cell death can be observed independent of the strain rate [Repo and Finlay 1977, Torzilli et al. 1999, Milentijevic et al. 2005]. The strain rate will however have an influence on the water pressed out of the tissue which results in varying strains at which the failure pressure is reached. Massive matrix damage under compression could be observed at loadings in the range of 35 MPa (40% strain) [Kerin et al. 1998] to 45 MPa (80% strain) [Torzilli et al. 1999]. The study of Demarteau et al. reported cartilage cell death to be linked with surface cracking which occurred at 14 MPa stress and 60% strain independent of the strain rate [Demarteau et al. 2006]. Measured fatigue failures in knee cartilage were in the range from 2.5 to 3.0 MPa [Weightman et al. 1978, Bellucci and Seedhom 2001].

Although the presented experimental studies give an idea of physiological contact pressures and cartilage deformation, these quantities can not be measured in vivo during activities of daily living. Therefore several numerical models have been developed to answer this question [Brand 2005]. However, to the authors knowledge no numerical model of a healthy shoulder exists to estimate glenohumeral contact pressures and cartilage deformation. We thus propose a finite element model of the glenohumeral joint, which has the ability to estimate the articular contact mechanics during shoulder movements.

3.2 Material and Methods

The section describes the setup of the numerical model. The geometry was reconstructed out of the same MRI images as the previously described musculoskeletal model (Section 3.2.1). The models were thus patient specific based on the same volunteer. Constitutive laws are described in section 3.2.2. Cartilage material parameters were identified with the use of experimental data on cartilage compression tests. As it was not possible to derive bone elastic moduli out of the MRI images, we analysed CT scans of other healthy shoulders to obtain the elastic moduli for glenoid and humeral head bones. The final section gives details on the finite element realisation of the model in Abaqus (Dassault Systèmes, France).

3.2.1 Anatomy Reconstruction

The glenohumeral contact model was built upon the same MRI images as the musculoskeletal upper limb model for muscle force computation (Section 2.2.2). The images were obtained from a 27 years old male volunteer showing no sign of shoulder pathology. A custom MRI protocol on a 3 Tesla MRI scanner was used, which included two three dimensional sequences: a gradient-recalled echo VIBE (TR/TE, 12.2/4.8 ms) of the glenohumeral joint with an isotropic resolution of 0.6 mm and a turbo spin-echo SPACE (TR/TE, 600/9.1 ms) of the right hemithorax with an isotropic resolution of 0.9 mm. The sequences were registered using Amira (FEI Visualization Sciences Group, France).

The MRI images were used to reconstruct scapula, humerus, glenoid cartilage, and humeral head cartilage. The MRI images were manually segmented using Amira. The reconstructed surfaces were imported to Geomagic (3D Systems, USA) for surface optimization and smoothing. Solidworks (Dassault Systèmes, France) was used to transform the surfaces into volumetric 3D bodies. The reconstructed geometry was superposed to the MRI images for visual verification. Finally, the 3D bodies were imported into Abaqus for finite element analysis.

The dimensions of the glenoid cavity were 23 mm in anterior posterior direction and 30 mm in superior inferior direction. The radius of curvature was 43 mm in the superior inferior plane and 47 mm in the anterior posterior plane.

3.2.2 Material Properties

The cartilage layers were modelled incompressible, isotropic, and hyperelastic. An exponential strain energy density function Ψ was used [Pioletti et al. 1998]:

$$\Psi = \alpha e^{(\beta(I_1 - 3))} - \alpha\beta(I_2 - 3) \tag{3.1}$$

The invariants I_1 and I_2 of the Cauchy Green deformation tensor $\mathbf{C}$ are defined as:

$$I_1 = \text{tr}(\mathbf{C}) \qquad I_2 = \frac{1}{2}\left[\text{tr}(\mathbf{C})^2 - \text{tr}(\mathbf{C}^2)\right] \tag{3.2}$$

and material constants α and β. The stress-strain relationship of the strain energy density Ψ (eq. 3.1) can be written as follows. Ψ is given in terms of invariants, the following derivation can thus be used (for details, see p.e. Holzapfel [2000]):

$$
\begin{aligned}
\mathbf{S} &= 2\frac{\partial \Psi(\mathbf{C})}{\partial \mathbf{C}} \\
&= 2\left[\left(\frac{\partial \Psi(I_1, I_2)}{\partial I_1} + I_1\frac{\partial \Psi}{\partial I_2}\right)\mathbf{I} - \frac{\partial \Psi}{\partial I_2}\mathbf{C}\right] \\
&= 2\left[\alpha\beta e^{\beta(I_1 - 3)} + I_1\alpha\beta\right]\mathbf{I} - \alpha\beta\mathbf{C}
\end{aligned} \tag{3.3}
$$

The identification of the material constants α and β was done with the use of experimental data. Healthy human articular cartilage, harvested from the humeral head of two elderly donors, were used. Cylindrical samples with a diameter of 1.6 mm were cut out of the articular surfaces using a dermal punch. Then the bone layer was cut off with a scalpel to obtain full thickness cartilage samples. The samples were put in a phosphate buffered saline bath to prevent dehydration of the tissues. The samples were used for uniaxial compressive testing with a strain rate of 0.1 1/s. To guarantee full contact between the cartilage sample and the loading actuator, a preloading period was included in the testing protocol before the compression started. Load and displacement were recorded. The tests were done on an Instron E3000 linear mechanical testing machine (Norwood, USA).

The load-displacement data was converted into stress-strain data using the following approach. The principal stretches of an axis symmetric homogeneous deformation state can be expressed in cylindrical coordinates (r, ϕ, z) with:

$$\mathrm{d}r = \lambda_r \mathrm{d}R \qquad \mathrm{d}\phi = \mathrm{d}\Phi \qquad \mathrm{d}z = \lambda_z \mathrm{d}Z \tag{3.4}$$

with the cylindrical coordinates (R, Φ, Z) of the reference configuration and the principal stretches λ_r and λ_z.

Calculating the deformation gradient $\mathbf{F}$ with:

$$\mathbf{F}(\mathbf{X}) = \frac{\partial \chi(\mathbf{X})}{\partial \mathbf{X}} = \nabla \mathbf{x}(\mathbf{X}) \tag{3.5}$$

using the ∇ operator in cylindrical coordinates:

$$\nabla = \mathbf{e}_r \frac{\partial}{\partial R} + \mathbf{e}_\phi \frac{1}{R} \frac{\partial}{\partial \Phi} + \mathbf{e}_z \frac{\partial}{\partial Z} \tag{3.6}$$

leads to:

$$\mathbf{F} = \begin{pmatrix} \frac{\partial r}{\partial R} & 0 & 0 \\ 0 & \frac{1}{R}\frac{\partial \phi}{\partial \Phi} & 0 \\ 0 & 0 & \frac{\partial z}{\partial Z} \end{pmatrix} = \begin{pmatrix} \lambda_r & 0 & 0 \\ 0 & \lambda_r & 0 \\ 0 & 0 & \lambda_z \end{pmatrix} \tag{3.7}$$

The assumption of incompressibility gives the relationship between the principal stretches:

$$J = \det(\mathbf{F}) = \lambda_r^2 \lambda_z = 1 \tag{3.8}$$

The final form of the deformation gradient is thus:

$$\mathbf{F} = \begin{pmatrix} \sqrt{\lambda} & 0 & 0 \\ 0 & \sqrt{\lambda} & 0 \\ 0 & 0 & \lambda \end{pmatrix} \tag{3.9}$$

The 2nd Piola Kirchhoff stress **S** in the cartilage samples was calculated with the following formula:

$$\mathbf{S} = \mathbf{F}^{-1}\mathbf{P} = \mathbf{F}^{-1}\begin{pmatrix} 0 & 0 & 0 \\ 0 & 0 & 0 \\ 0 & 0 & \frac{f_{zz}}{A} \end{pmatrix} \tag{3.10}$$

with the nominal stress **P**, the loading force f_{zz} and the initial surface of the sample A, which gives the stress-strain relationship of the experimental data.

The constitutive equation 3.3 was then fitted to the experimental stress-strain curves to identify the material parameters α and β. To do this, we imported the experimental data into Matlab (The MathWorks, USA), implemented the constitutive equation and performed a least square fitting with the intrinsic Matlab function lscurvefit.

The bones, scapula and humerus, were modelled as rigid bodies except for the glenoid and the humeral epiphysis. These parts were modelled as linear elastic isotropic homogeneous materials. Cortical and trabecular bones were distinguished. CT scans of ten healthy shoulders, provided by the radiology department of the university hospital of Lausanne, were used to evaluate cortical bone thickness and Young's moduli of cortical and trabecular bones on both glenoid and humeral head.

To measure the cortical bone thickness, a line was drawn perpendicular to the articular surface (Figure 3.1 left image). Along this line, the HU value was analysed (Figure 3.1 right image). The width of the first peak was assumed to be the cortical bone thickness. For glenoid cortical bone thickness, the measurement has been done on ten measuring points equally distributed on the glenoid cavity in each of the ten CT scans. This gave a total number of 100 measuring points. The average value of the 100 measurements was taken as glenoid cortical bone thickness. The same procedure has been repeated for the humeral head to determine humeral head cortical bone thickness.

To determine Young's moduli for the trabecular and cortical bone of the glenoid and humeral head out of the CT scans, three steps were performed on each CT scan: first, the glenoid and humeral head were semi-automatically segmented out of the CT data using a threshold. Second, the outer volume of the reconstructed shapes were assigned to be cortical bone (Figure 3.2 left image). The thickness of the glenoid and humeral cortical bone layers were obtained from the measurement described in the previous paragraph. The inner volume was assigned to be trabecular bone (Figure 3.2 right image). Third, the mean HU value was
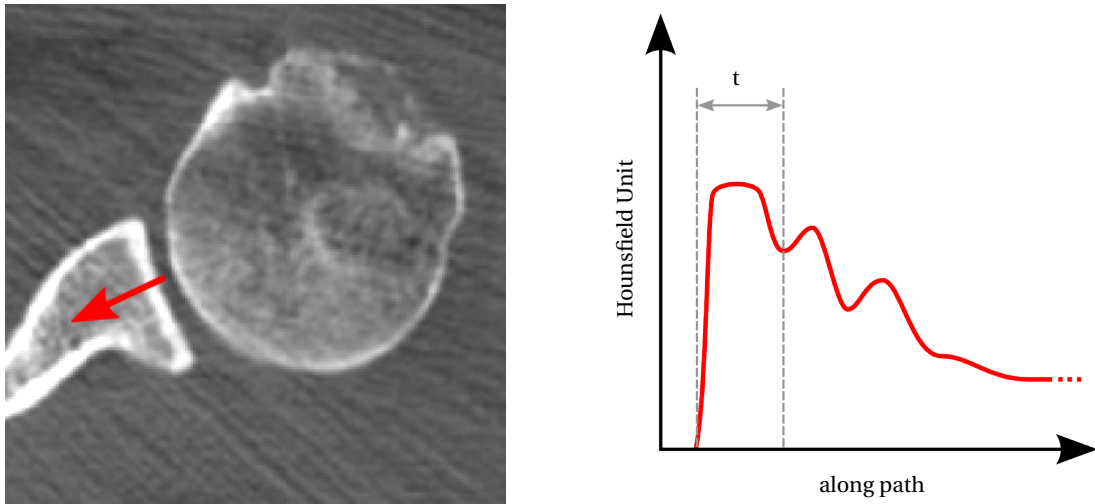
Figure 3.1 – Illustration of cortical bone thickness measurement. A line perpendicular to the articular surface is defined at an arbitrarily chosen point (left image, red arrow). The Hounsfield values are plotted along this line (right image). The first peak is considered to be cortical bone and its width taken as cortical bone thickness.

calculated for each region. The Young's modulus E was calculated using the formula proposed by Gupta et al. [2004]:

$$E = 3 * 10^{-6} * (0.6410 * HU)^3 \tag{3.11}$$

where HU specified the mean Hounsfield value measured in the CT scans.

3.2.3   Finite Element Model

The glenohumeral contact model was built in the scapula reference frame defined following the ISB standards [Wu et al. 2005]. The deformable parts of the finite element model were meshed with quadratic tetrahedral elements (10-node quadratic tetrahedron, hybrid, constant pressure). Due to the geometric complexity, hexahedral elements could not be used. The cartilage layers were meshed with two layers of elements. The required fineness of the mesh was verified during a mesh study. Convergence criterion was the strain energy.

Glenoid trabecular bone, cortical bone, and cartilage were tied together with a tie constraint allowing no displacement. Humeral head trabecular bone, cortical bone, and cartilage were also tied together. The movement of the humerus relative to the scapula was defined with a rotational boundary condition. The rotations were taken from the upper limb model (Section 2.2.2) to reproduce the same movement. In the upper limb model, the rotations of the bones are defined by rotations matrices **R** describing the transformation from local bone reference
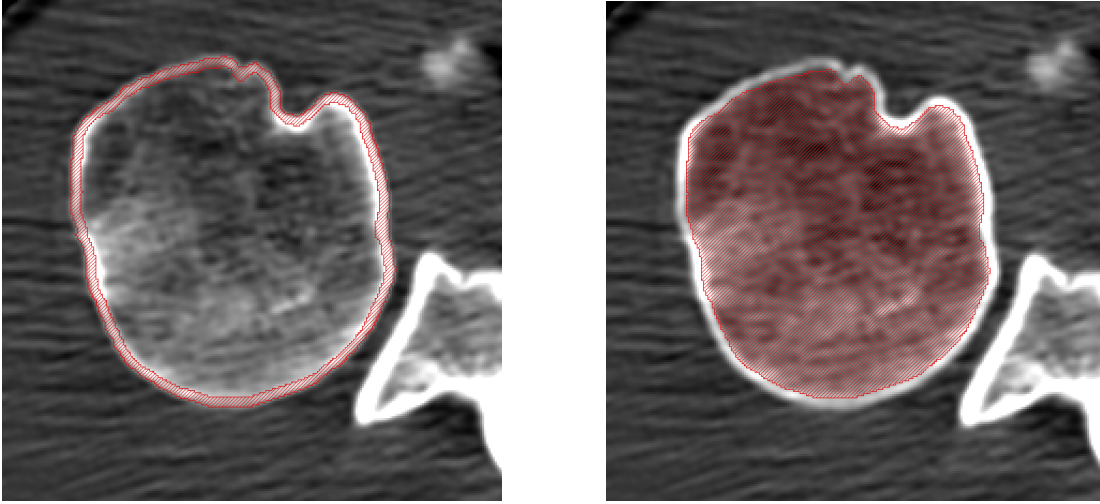
Figure 3.2 – Segmentation of cortical (left image) and trabecular (right image) bone at the humeral head. The mean Hounsfield value was determined for the red regions to estimate the bone density of the bone layers.

frames to the global reference frame. The rotation of the humerus in the scapula reference frame can thus be written as:

$$\mathbf{R}_{H2S} = \mathbf{R}_{H2G} * \mathbf{R}_{S2G}^{\mathrm{T}} \tag{3.12}$$

The rotations in Abaqus are defined as Tait-Bryan Angles (α, β, γ) around the initial axis x-y-z. Thus, the humeral rotation matrix provided by the upper limb model can be decomposed as:

$$
\begin{aligned}
\mathbf{R}_{H2S} &= \mathbf{R}_x \mathbf{R}_y \mathbf{R}_z \\
&= \begin{pmatrix} 1 & 0 & 0 \\ 0 & \cos\alpha & -\sin\alpha \\ 0 & \sin\alpha & \cos\alpha \end{pmatrix} \begin{pmatrix} \cos\beta & 0 & \sin\beta \\ 0 & 1 & 0 \\ -\sin\beta & 0 & \cos\beta \end{pmatrix} \begin{pmatrix} \cos\gamma & -\sin\gamma & 0 \\ \sin\gamma & \cos\gamma & 0 \\ 0 & 0 & 1 \end{pmatrix} \\
&= \begin{pmatrix} \cos\beta\cos\gamma & -\cos\beta\sin\gamma & \sin\beta \\ \sin\alpha\sin\beta\cos\gamma + \cos\alpha\sin\gamma & -\sin\alpha\sin\beta\sin\gamma + \cos\alpha\cos\gamma & -\sin\alpha\cos\beta \\ -\cos\alpha\sin\beta\cos\gamma + \sin\alpha\sin\gamma & \cos\alpha\sin\beta\sin\gamma + \sin\alpha\cos\gamma & \cos\alpha\cos\beta \end{pmatrix}
\end{aligned} \tag{3.13}
$$

The angles (α, β, γ) are obtained by solving this system of equations (for details 3.A.1).

During the movement, the humeral head was loaded with the joint reaction force computed by the upper limb model (Section 2.2.2, figure 2.8). The translation of the humeral head was

not restricted: it was only held by the articular contact surfaces and the joint reaction force. The humeral head could thus migrate on the glenoid cavity in both superior-inferior and anterior-posterior direction.

In between the hyperelastic cartilage layers, a frictionless contact allowing no penetration was defined. The "hard contact" model in Abaqus with the default constraint enforcement method was used. The contact pattern, contact pressure, cartilage and bone deformation were computed for an abduction movement in the scapula plane. To analyse deformation, the equivalent strain (von Mises or maximum distortion strain energy criterion) which is defined in means of principal strains was calculated:

$$\varepsilon_e = \frac{2}{\sqrt{3}} \sqrt{I_2'} \tag{3.14}$$

with the second invariant of the strain deviator I_2', expressed in terms of principal strains:

$$I_2' = \frac{1}{6} \left[(\varepsilon_1 - \varepsilon_2) + (\varepsilon_2 - \varepsilon_3) + (\varepsilon_3 - \varepsilon_1) \right] \tag{3.15}$$

The influence of the Young's modulus of the bones on the numerical results was further analysed. To do this, the Young's modulus of scapula cortical, scapula trabecular, humeral cortical, and humeral trabecular bone was increased by + 50 % and changes in predicted cartilage equivalent strain were analysed

3.3 Results

The cortical bone thickness in the glenoid cavity was 3.2 mm in average on the ten CT scans. The average cortical bone thickness on the humeral head was 1.9 mm. The HU value analysis of the CT images gave a Young's modulus of 190 MPa for glenoid cortical bone and 60 MPa for glenoid trabecular bone respectively. The Young's modulus for the humeral head cortical bone was determined to be 120 MPa and 45 MPa for humeral head trabecular bone respectively.

The material parameters for cartilage obtained from the experimental stress-strain measurements (Figure 3.1) were $\alpha = 1.15$ MPa and $\beta = 1.17$ respectively.

At the beginning of the abduction movement, the humeral head was situated in a superior position on the glenoid cavity. Up to 60° abduction, the humeral head stayed in a superior position and moved slightly anteriorly. From 60° to 120°, the humeral head translated inferiorly staying in the anterior half of the glenoid cavity (Figure 3.4).

The cartilage contact pressure increased from 2.2 MPa at 0° abduction up to 3.9 MPa at 90° abduction (Figure 3.5). Glenoid cartilage equivalent strains increased from 21% at 30° up to 36% at 90° abduction. The histogram of strain distribution in the finite element mesh showed that peak strains were limited to a small region (Figure 3.6). The maximum cartilage strains were located underneath the contact area at the interface between cartilage and cortical bone. Humeral cartilage equivalent strains increased from 20% to 27%.

In the glenoid cortical bone, the minimum principal strain ranged from 0.5% at 0° up to 2.1% at 90° and from 1.5% to 3.2% in the glenoid trabecular bone respectively. In the humeral cortical bone, minimum principal strains ranged from 0.5% at 0° abduction up to 3.1% at 90° abduction and from 2.7% to 4.5% for humeral trabecular bone respectively.

The variation of the Young's modulus of the bones by +50% did not increase the maximum cartilage strain. However, a larger volume experienced higher strains in the range of 17 to 35 % equivalent strain (Figure 3.6).

3.4   Discussion

Osteoarthritis is a widely spread joint disease which can be triggered by unphysiological biomechanical conditions. Both repeated cartilage overloading and insufficient mechanical stimulus lead to similar tissue alterations. To investigate the articular contact pressure in the shoulder during movements, we propose a numerical model of the glenohumeral joint coupled to a musculoskeletal shoulder. It has the ability to reproduce the natural translation of the humeral head on the glenoid cavity, and thus can be used to estimate the contact pattern and contact pressure during shoulder movement.

The geometric reconstruction of the glenohumeral joint was obtained from in vivo MRI images. MRI scans have the advantage to be harmless to the scanned person, but provide a lower spatial resolution than CT images. For the reconstruction of bones and the identification of the cartilage layers, the isotropic resolution of 0.6 mm was sufficient. The reconstruction of the articular surfaces was especially challenging. The reconstructed contact surfaces did not have a smooth curvature and were not congruent. As a consequence the contact pattern was not circular (Figure 3.5).

The size of the glenoid cavity was in agreement with experimental studies [Peltz et al. 2015]. The radius of curvature was however larger than the reported mean values. This suggests a lower translational stiffness of the joint compared to the statistical average [Peltz et al. 2015].

The developed model only contained bones and cartilages. The exclusion of labrum, joint capsule and ligaments might lead to the assumption the model is underestimating glenohumeral stability. However, the labrum consists of collagen fibres that are ring-shaped around the glenoid. It is thus considered to be soft in the transverse plane. Further it is flexibly linked to the glenoid which further declines a considerable stabilizing role [Tischer and Putz 2003,

Parameter Identification Cartilage Model
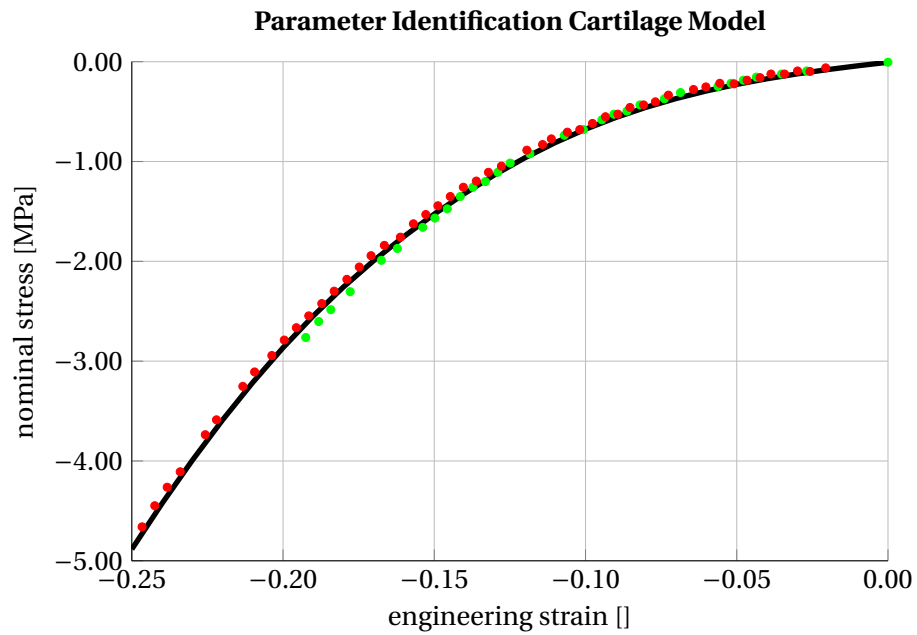
Figure 3.3 – Parameter identification for the cartilage model. The red and green dots show the experimental results of the compression test on two human cartilage samples harvested from the humeral head. The black curve shows the stress prediction of the fitted constitutive equation.
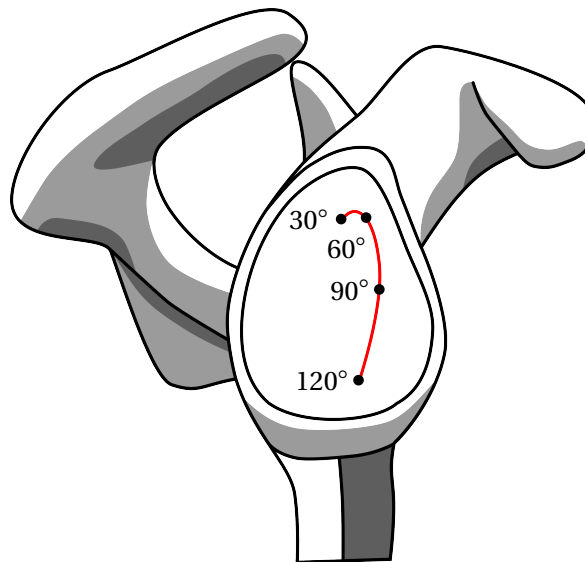
Figure 3.4 – Translation of the humeral head on the glenoid cavity for an abduction movement from a rest position up to 120 ° arm elevation.
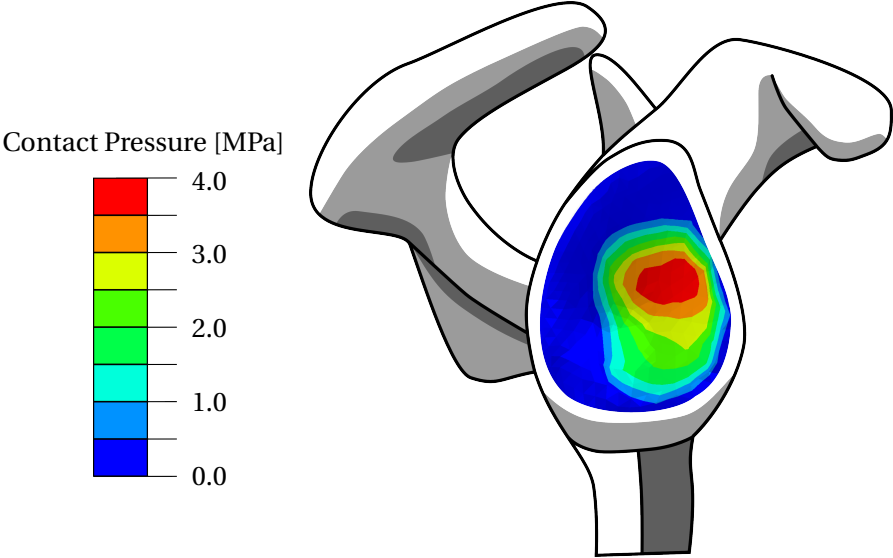
Figure 3.5 – Contact pressure on the glenoid cartilage layer at 90° abduction. The humeral head translated anteriorly.
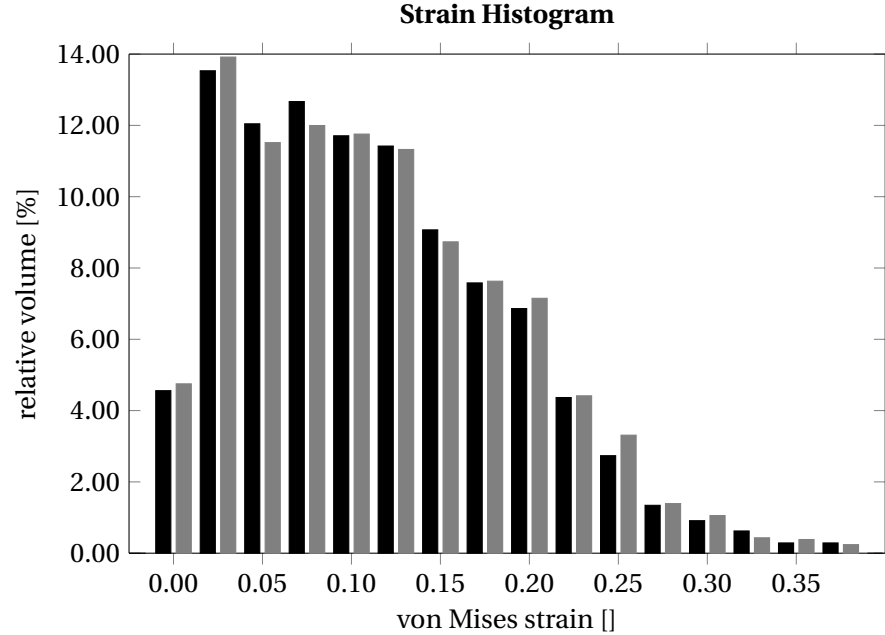
Figure 3.6 – Histogram of the strain distribution in the finite element mesh at 90° abduction. The relative volume (volume in threshold divided by total volume) is plotted over the equivalent strain. Black bars show the strain distribution for bone Young's modulus determined from CT scans. Grey bars show the strain distribution with increased bone Young's modulus.

Barthel et al. 2003, Veeger and van der Helm 2007]. Joint capsule and ligaments are passive tissues and can consequently only provide stability when they are stretched. This is only the case in extreme rotated positions. In the midrange of shoulder movements and humeral translations they do not contribute to joint stability [Engin and Chen 1986, Blasier et al. 1997, Veeger and van der Helm 2007]

In this work we modelled cartilage with an exponential hyperelastic constitutive law. The parameters were identified using experimental data. The material model thus described the mechanical behaviour of healthy cartilage, but it was limited to low compression rates under 0.1 1/s. We only had 2 cartilage samples at disposal. The measurement should be repeated with further samples to verify statistical validity. The viscoelastic properties of cartilage, that are linked to synovial fluid flow in the tissue were not taken into account. However, the material model was only used in quasistatic simulations and was thus considered suitable in our framework.

The subchondral bone layers were modelled with homogeneous isotropic linear elastic materials. We justify the simplification with the fact, that we did not aim to predict bone strains. The deformable bone layers should rather diminish stress-strain peaks at the cartilage-bone interface to prevent a possible stress-strain overestimation at this location. Due to the unavailability of a complete set of material properties and geometric parameters for glenoid and humeral, cortical and trabecular bone layers, we identified the Young's modulus of these bones with the help of CT data. We took advantage of the link between HU values and bone density. As it was not feasible to do a CT scan of the volunteer used for anatomic reconstruction (Section 2.2.2), we used ten CT scans of healthy shoulders of poly-traumatic patients, provided by the CHUV orthopaedic department, to determine cortical bone thickness and average HU values for cortical and trabecular bones. The obtained HU values for the glenoid bone were in agreement with a similar study [Knowles et al. 2014]. Another study reported glenoid HU values more than three times higher [Simon et al. 2015]. It is however difficult to compare HU values, as they may vary from CT scanner calibration and scan protocols. The Young's modulus was calculated with a formula proposed by Gupta et al. [2004]. The obtained Young's modulus for glenoid trabecular bone was lower than those determined in experimental studies (mean 150 MPa [Kalouche et al. 2010], mean 105 MPa [Frich et al. 1997]). We used the same formula to estimate the Young's modulus of the humeral head, although the coefficients of this formula were calibrated for use with the scapula. Again, the obtained values for the Young's modulus were lower than those determined with experimental studies using cylindrical samples harvested from the humeral head (average 190 MPa [Frich and Jensen 2014]). We assume accordingly that the estimation of Young's Moduli from CT images tends to underestimate the elastic properties. For the use in our model however, increasing the bones' Young's modulus did not increase maximum strains and showed a similar strain distribution (Figure 3.6). An alternative approach to obtain the bone density data would be the use of quantitative MRI protocols [Lammentausta et al. 2006, Bae et al. 2012], which were however not at the author's disposal.

In vivo studies that analysed humeral head translations during abduction movements, found an initial superior shift, followed by an inferior shift in the second half of the movement [Graichen et al. 2000, Massimini et al. 2012]. The same studies reported a posterior shift during the movement. The model's prediction are thus in agreement concerning the superior-inferior shift. In contrast to the experimental studies, our model predicted the humeral head to stay in the anterior part of the glenoid cavity. The predicted humeral head translations are strongly linked to the input data from the musculoskeletal upper limb model (Section 2.2.2): the humeral head follows the direction of the used joint reaction force. The anterior shift of the humeral head position is such not a default of the contact model. It is a result of the anteriorly shifted joint reaction force (Section 2.2.3).

The model's prediction for cartilage contact pressure was lower than failure stresses [Repo and Finlay 1977, Torzilli et al. 1999, Milentijevic et al. 2005, Demarteau et al. 2006] and lower than experimental pressures used for growth stimulation [Grad et al. 2011]. As the predicted contact pressure is dependent on the joint reaction force taken from the musculoskeletal model, the low cartilage pressure might be an indication that the joint reaction force is underestimated. Both the joint reaction force and contact pressure are also related to the chosen movement of a slow abduction. Peak joint reaction forces and damaging contact pressures are rather expected during dynamic movements or accident impacts.

The predicted contact pressure was however in the range of fatigue damage [Weightman et al. 1978, Bellucci and Seedhom 2001]. In the experimental studies by Weightman et al. and Bellucci and Seedhom, cadaveric cartilage samples were loaded with up to 10^6 cycles. The samples were such deprived of their proper repair mechanisms. Further it is unlikely that such numbers of loading cycles in the experimental time span are reached in vivo. The fact, that matrix protein production is stimulated at pressures higher than fatigue failure, is understood in such a way, that cartilage cells react on initiated damage.

Predicted cartilage strains were lower than experimentally determined cartilage failure strains [Kerin et al. 1998, Torzilli et al. 1999, Demarteau et al. 2006]. We used the equivalent strain for the evaluation. In a compressive deformation, the minimum principal strains could also be investigated. The equivalent strain does however consider the three dimensional deformation state and not only the deformation in one direction.

The experimental studies on cartilage tissue cited here had in most cases no direct link to shoulder pathologies. Several studies worked with bovine cartilage, those analysing human cartilage used samples from shoulder, hip and knee. We consider these studies nevertheless. The clinical relevance of animal based cartilage models has been proven [Demarteau et al. 2006, Chu et al. 2010, Lampropoulou-Adamidou et al. 2014]. We are aware that cartilage properties differ between joints [Kuettner and Cole 2005]. On the other hand, all articular cartilage layers show the same structure: a dense extracellular matrix made of collagen, proteoglycans, and water, in which chondrocytes are sparsely embedded [Sophia Fox et al. 2009]. The property variations are thus expected to stay within a close range. However, there

is a lack of experimental studies on glenohumeral cartilage and there is a need to confirm the existing findings in cartilage research for the shoulder.

The strength of the presented model was to represent the articular contact of a healthy shoulder. The contact was modelled with two deformable hyperelastic cartilage layers. Cortical and trabecular bone layers were included to avoid overestimation of the cartilage strains and stresses. Further the humeral head was free to translate on the glenoid cavity to allow its natural translation. However, we did not model the labrum around the glenoid cavity nor ligaments and joint capsule. The model might underestimate the stability of the joint in extreme position and consequently predict subluxations in cases where the joint is hold by ligaments and joint capsule. In this study, we only simulated a quasistatic movement, although highest pressures are expected to arise during dynamic movement. For such a framework, the material model for cartilage should further be extended with viscoelastic properties, which would require further experimental data for material parameter identification.

In the context of this thesis, the cartilage model will be used to analyse the link between patient specific joint reaction forces and cartilage strain. The model does not only allow to estimate cartilage strain, but also the contact pattern related to humeral head translations. We aim to identify risk factors for the development of glenohumeral osteoarthritis. The migration of the humerus will further be used to investigate supraspinatus tendon impingement and related tendon tears.

3.A Appendix

3.A.1 Computing Tait-Bryan Angles from Rotation Matrices

A rotation matrix $\mathbf{R}$ is given. To compute the corresponding Tait-Bryan angles using the x-y-z sequence around the initial axis, $\mathbf{R}$ can be decomposed as follows:

$$
\begin{aligned}
\mathbf{R} &= \mathbf{R}_x \mathbf{R}_y \mathbf{R}_z \\
&= \begin{pmatrix} 1 & 0 & 0 \\ 0 & \cos\alpha & -\sin\alpha \\ 0 & \sin\alpha & \cos\alpha \end{pmatrix} \begin{pmatrix} \cos\beta & 0 & \sin\beta \\ 0 & 1 & 0 \\ -\sin\beta & 0 & \cos\beta \end{pmatrix} \begin{pmatrix} \cos\gamma & -\sin\gamma & 0 \\ \sin\gamma & \cos\gamma & 0 \\ 0 & 0 & 1 \end{pmatrix} \\
&= \begin{pmatrix} \cos\beta\cos\gamma & -\cos\beta\sin\gamma & \sin\beta \\ \sin\alpha\sin\beta\cos\gamma + \cos\alpha\sin\gamma & -\sin\alpha\sin\beta\sin\gamma + \cos\alpha\cos\gamma & -\sin\alpha\cos\beta \\ -\cos\alpha\sin\beta\cos\gamma + \sin\alpha\sin\gamma & \cos\alpha\sin\beta\sin\gamma + \sin\alpha\cos\gamma & \cos\alpha\cos\beta \end{pmatrix}
\end{aligned} \tag{3.16}
$$

The second Tait-Bryan angle β can be obtained by solving:

$$
\beta_1 = \arcsin(\mathbf{R}_{1,3}) \tag{3.17}
$$

Since $\sin\beta = \sin(\pi - \beta)$, a second value for β can be obtained with:

$$
\beta_2 = \pi - \beta_1 = \pi - \arcsin(\mathbf{R}_{1,3}) \tag{3.18}
$$

The angle α can be calculated by solving:

$$
\frac{\mathbf{R}_{23}}{\mathbf{R}_{33}} = -\tan\alpha \tag{3.19}
$$

using the four quadrant tangent inverse:

$$
\alpha = \begin{cases} \arctan 2(-\mathbf{R}_{23}, \mathbf{R}_{33}) & \text{if } \cos\beta \geq 0 \\ \arctan 2(\mathbf{R}_{23}, -\mathbf{R}_{33}) & \text{if } \cos\beta < 0 \end{cases} \tag{3.20}
$$

To avoid the distinction of cases, one can use:

$$\alpha = \arctan 2(-\frac{\mathbf{R}_{23}}{\cos\beta}, \frac{\mathbf{R}_{33}}{\cos\beta}) \tag{3.21}$$

This equation leads to two values for α:

$$\alpha_1 = \arctan 2(-\frac{\mathbf{R}_{23}}{\cos\beta_1}, \frac{\mathbf{R}_{33}}{\cos\beta_1})$$
$$\alpha_2 = \arctan 2(-\frac{\mathbf{R}_{23}}{\cos\beta_2}, \frac{\mathbf{R}_{33}}{\cos\beta_2}) \tag{3.22}$$

The third angle γ can be calculated the same way as α:

$$\gamma_1 = \arctan 2(-\frac{\mathbf{R}_{12}}{\cos\beta_1}, \frac{\mathbf{R}_{11}}{\cos\beta_1})$$
$$\gamma_2 = \arctan 2(-\frac{\mathbf{R}_{12}}{\cos\beta_2}, \frac{\mathbf{R}_{11}}{\cos\beta_2}) \tag{3.23}$$

Both triplets $(\alpha_1, \beta_1, \gamma_1)$ and $(\alpha_2, \beta_2, \gamma_2)$ are valid solutions and reproduce the rotation matrix.

The special case $\mathbf{R}_{13} = \pm 1$, corresponding to $\beta = \pm\pi/2$, leads to $\cos\beta = 0$. This situation is called *Gimbal Lock* and is a known geometric problem in the context of Euler angles. In this situation, the angles α and γ are linked leading to an infinite amount of solutions. As we are only interested in finding one solution, the general approach is to set $\alpha = 0$ and calculate γ using p.e. $\mathbf{R}_{31}$ and $\mathbf{R}_{32}$:

$$\gamma = \arctan 2(\mathbf{R}_{32}, \mathbf{R}_{31}) \tag{3.24}$$

3.B   Bibliography

Armstrong C. G., Bahrani A. S., and Gardner D. L.: In vitro measurement of articular cartilage deformations in the intact human hip joint under load. *Journal of Bone and Joint Surgery - Series A*, 61(5):744–755, 1979.

Bae W., Chen P., Chung C., Masuda K., D'Lima D., and Du J.: Quantitative ultrashort echo time (ute) mri of human cortical bone: Correlation with porosity and biomechanical properties. *Journal of Bone and Mineral Research*, 27(4):848–857, 2012.

Barthel T., König U., Böhm D., Loehr J. F., and Gohlke F.: Die anatomie des labrum glenoidale. *Der Orthopäde*, 32(7):578–585, 2003.

Bellucci G. and Seedhom B. B.: Mechanical behaviour of articular cartilage under tensile cyclic load. *Rheumatology*, 40(12):1337–1345, 2001.

Blasier R. B., Soslowsky L. J., Malicky D. M., and Palmer M. L.: Posterior glenohumeral subluxation: active and passive stabilization in a biomechanical model. *Journal of Bone and Joint Surgery—American*, 79:433–440, 1997.

Brand R. A.: Joint contact stress: a reasonable surrogate for biological processes? *The Iowa orthopaedic journal*, 25:82–94, 2005.

Brandt K. D., Dieppe P., and Radin E.: Etiopathogenesis of osteoarthritis. *Medical Clinics of North America*, 93(1):1–24, 2009.

Buckwalter J. A. and Martin J. A.: Osteoarthritis. *Advanced Drug Delivery Reviews*, 58(2): 150–167, 2006.

Carver S. E. and Heath C. A.: Increasing extracellular matrix production in regenerating cartilage with intermittent physiological pressure. *Biotechnology and Bioengineering*, 62(2): 166–174, 1999.

Chu C. R., Szczodry M., and Bruno S.: Animal models for cartilage regeneration and repair. *Tissue Engineering - Part B: Reviews*, 16(1):105–115, 2010. cited By 85.

Conzen A. and Eckstein F.: Quantitative determination of articular pressure in the human shoulder joint. *Journal of Shoulder and Elbow Surgery*, 9(3):196–204, 2000.

Demarteau O., Pillet L., Inaebnit A., Borens O., and Quinn T. M.: Biomechanical characterization and in vitro mechanical injury of elderly human femoral head cartilage: comparison to adult bovine humeral head cartilage. *Osteoarthritis Cartilage*, 14:589–596, 2006.

Eckstein F., Hudelmaier M., and Putz R.: The effects of exercise on human articular cartilage. *Journal of Anatomy*, 208(4):491–512, 2006.

Egloff C., Hügle T., and Valderrabano V.: Biomechanics and pathomechanisms of osteoarthritis. *Swiss Med Wkly*, 142:w13583, 2012.

Elder B. D. and Athanasiou K. A.: Hydrostatic pressure in articular cartilage tissue engineering: From chondrocytes to tissue regeneration. *Tissue Engineering - Part B: Reviews*, 15(1):43–53, 2009.

Engin A. E. and Chen S. M.: Statistical data base for the biomechanical properties of the human shoulder complex - I: kinematics of the shoulder complex. *Journal of Biomechanical Engineering*, 108:215–221, 1986.

Eyre D. R.: Collagens and cartilage matrix homeostasis. *Clinical Orthopaedics and Related Research*, (427 SUPPL.):118–122, 2004.

Frich L. H. and Jensen N. C.: Bone properties of the humeral head and resistance to screw cutout. *International Journal of Shoulder Surgery*, 8(1):21–26, 2014.

Frich L. H., Jensen N. C., Odgaard A., Pedersen C. M., Søjbjerg J. O., and Dalstra M.: Bone strength and material properties of the glenoid. *Journal of Shoulder and Elbow Surgery*, 6(2): 97 – 104, 1997.

Grad S., Eglin D., Alini M., and Stoddart M. J.: Physical stimulation of chondrogenic cells in vitro: A review. *Clinical Orthopaedics and Related Research*, 469(10):2764–2772, 2011.

Graichen H., Stammberger T., Bonel H., Englmeier K.-H., Reiser M., and Eckstein F.: Glenohumeral translation during active and passive elevation of the shoulder - a 3D open-MRI study. *J Biomech*, 33(5):609–613, 2000.

Gupta S., van der Helm F. C. T., and van Keulen F.: Stress analysis of cemented glenoid prostheses in total shoulder arthroplasty. *Journal of Biomechanics*, 37(11):1777 – 1786, 2004.

Hasvold T. and Johnsen R.: Headache and neck or shoulder pain- frequent and disabling conditions in the general population. *Scandinavian Journal of Primary Health Care*, 1993.

Helmick C. G., Felson D. T., Lawrence R. C., Gabriel S., Hirsch R., Kwoh C. K., Liang M. H., Kremers H. M., Mayes M. D., Merkel P. A., Pillemer S. R., Reveille J. D., and Stone J. H.: Estimates of the prevalence of arthritis and other rheumatic conditions in the United States. part I. *Arthritis and Rheumatism*, 58(1):15–25, 2008.

Herberhold C., Faber S., Stammberger T., Steinlechner M., Putz R., Englmeier K. H., Reiser M., and Eckstein F.: In situ measurement of articular cartilage deformation in intact femoropatellar joints under static loading. *Journal of Biomechanics*, 32(12):1287–1295, 1999.

Hodge W. A., Fijan R. S., Carlson K. L., Burgess R. G., Harris W. H., and Mann R. W.: Contact pressures in the human hip joint measured in vivo. *Proceedings of the National Academy of Sciences of the United States of America*, 83(9):2879–2883, 1986.

Holzapfel G. A.: *Nonlinear Solid Mechanics*. Wiley, Chichester, England, 2000.

Jurvelin J., Kiviranta I., Tammi M., and Helminen J. H.: Softening of canine articular cartilage after immobilization of the knee joint. *Clinical orthopaedics and related research*, (207): 246–252, 1986.

Kalouche I., Crépin J., Abdelmoumen S., Mitton D., Guillot G., and Gagey O.: Mechanical properties of glenoid cancellous bone. *Clinical Biomechanics*, 25(4):292–298, 2010.

Kerin A. J., Wisnom M. R., and Adams M. A.: The compressive strength of articular cartilage. *Proceedings of the Institution of Mechanical Engineers, Part H: Journal of Engineering in Medicine*, 212(4):273–280, 1998.

Knowles N. K., Athwal G. S., Keener J. D., and Ferreira L. M.: Regional bone density variations in osteoarthritic glenoids: A comparison of symmetric to asymmetric (type b2) erosion patterns. *Journal of Shoulder and Elbow Surgery*, 2014.

Kobayashi T., Takagishi K., Shitara H., Ichinose T., Shimoyama D., Yamamoto A., Osawa T., and Tajika T.: Prevalence of and risk factors for shoulder osteoarthritis in japanese middle-aged and elderly populations. *Journal of Shoulder and Elbow Surgery*, 23(5):613–619, 2014.

Kuettner K. E. and Cole A. A.: Cartilage degeneration in different human joints. *Osteoarthritis and Cartilage*, 13(2):93–103, 2005.

Lammentausta E., Hakulinen M., Jurvelin J., and Nieminen M.: Prediction of mechanical properties of trabecular bone using quantitative mri. *Physics in Medicine and Biology*, 51(23): 6187–6198, 2006.

Lampropoulou-Adamidou K., Lelovas P., Karadimas E. V., Liakou C., Triantafillopoulos I. K., Dontas I., and Papaioannou N. A.: Useful animal models for the research of osteoarthritis. *European Journal of Orthopaedic Surgery and Traumatology*, 24(3):263–271, 2014.

Massimini D., Boyer P., Papannagari R., Gill T., Warner J., and Li G.: In-vivo glenohumeral translation and ligament elongation during abduction and abduction with internal and external rotation. *Journal of Orthopaedic Surgery and Research*, 7(1):1–9, 2012.

Milentijevic D., Deng X., Helfet D. L., and Torzilli P. A.: Cartilage resistance to a single impact-load: Protective effect of subchondral bone. *5st Annual Meeting of the Orthopaedic Research Society*, 2005.

Peltz C., Zauel R., Ramo N., Mehran N., Moutzouros V., and Bey M.: Differences in gleno-humeral joint morphology between patients with anterior shoulder instability and healthy, uninjured volunteers. *Journal of Shoulder and Elbow Surgery*, 24(7):1014–1020, 2015.

Pioletti D. P., Rakotomanana L. R., Benvenuti J. F., and Leyvraz P. F.: Viscoelastic constitutive law in large deformations: application to human knee ligaments and tendons. *J Biomech*, 31 (8):753–757, 1998.

Pope D. P., Croft P. R., Pritchard C. M., and Silman A. J.: Prevalence of shoulder pain in the community: The influence of case definition. *Annals of the Rheumatic Diseases*, 56(5): 308–312, 1997.

Repo R. U. and Finlay J. B.: Survival of articular cartilage after controlled impact. *Journal of Bone and Joint Surgery - Series A*, 59(8):1068–1076, 1977.

Simon P., Gupta A., Pappou I., Hussey M. M., Santoni B. G., Inoue N., and Frankle M. A.: Glenoid subchondral bone density distribution in male total shoulder arthroplasty subjects with eccentric and concentric wear. *Journal of Shoulder and Elbow Surgery*, 24(3):416–424, 2015.

Sophia Fox A. J., Bedi A., and Rodeo S. A.: The basic science of articular cartilage: Structure, composition, and function. *Sports Health*, 1(6):461–468, 2009.

Tischer T. and Putz R.: Die anatomie des oberen labrumkomplexes im schultergelenk. *Der Orthopäde*, 32(7):572–577, 2003.

Torzilli P. A., Grigiene R., Borrelli Jr. J., and Helfet D. L.: Effect of impact load on articular cartilage: Cell metabolism and viability, and matrix water content. *Journal of Biomechanical Engineering*, 121(5):433–441, 1999.

Vanwanseele, Eckstein F., Knecht H., Stüssi E., and Spaepen A.: Knee cartilage of spinal cord-injured patients displays progressive thinning in the absence of normal joint loading and movement. *Arthritis and Rheumatism*, 46(8):2073–2078, 2002.

Veeger H. E. J. and van der Helm F. C. T.: Shoulder function: The perfect compromise between mobility and stability. *J Biomech*, 40(10):2119–2129, 2007.

Weightman B., Chappell D. J., and Jenkins E. A.: A second study of tensile fatigue properties of human articular cartilage. *Annals of the Rheumatic Diseases*, 37(1):58–63, 1978.

Wieland H. A., Michaelis M., Kirschbaum B. J., and Rudolphi K. A.: Osteoarthritis - an untreatable disease? *Nature Reviews Drug Discovery*, 4(4):331–344, 2005.

Wu G., van der Helmb F. C. T., Veeger H. E. J., Makhsouse M., Royf P. V., Angling C., Nagelsh J., Kardunai A. R., McQuadej K., Wangk X., Wernerl F. W., and Buchholzm B.: ISB recommendation on definitions of joint coordinate systems of various joints for the reporting of human joint motion - Part II: shoulder, elbow, wrist and hand. *J Biomech*, 38:981–992, 2005.

4 Tendon Model

In this chapter, a finite element model of the supraspinatus tendon is presented. The chapter is divided into two parts. The first part describes a model which is limited to compute tendon strains in static positions. The model has been used to analyse loading capacities of partially torn supraspinatus tendon. While the model presented in the first section was limited to an arm position at 90° abduction, the second part introduces an extension of the tendon model to compute tendon strains at different degrees of arm elevation. This was motivated by the fact, that 90% of our daily shoulder movements stay below 60° abduction [Coley et al. 2008]. Chronic tears are thus expected to initiate at low arm elevation angles. The extended model had further the ability to analyse the subacromial space and an eventual tendon impingement. In the overall structure of this thesis, the tendon model is the third model: it takes shoulder kinematics and supraspinatus forces from the upper limb model (Chapter) and humeral head translation from the cartilage model (Chapter 3) as input to estimate tendon strains. In the following chapter, the tendon model will be used to analyse the effect of anatomic parameters on tendon tears.

4.1 Loading Capacity of Partially Torn Supraspinatus Tendon

The following section has been published in the journal "Computer Methods in Biomechanical and Biomedical Engineering" under the title "Effect of Partial-Thickness Tear on Loading Capacities of the Supraspinatus Tendon: A Finite Element Analysis" [Engelhardt et al. 2015].

4.1.1 Introduction

Active stabilization of the glenohumeral joint by the rotator cuff muscles is essential. Stability of the joint can be affected by neurological disorders, degeneration of the muscle-tendon unit, or trauma. Partial-thickness tears of the rotator cuff tendons are among the most common causes of shoulder pathologies [Williams et al. 2004], affecting young athletes, middle-aged workers, and the elderly [Fukuda et al. 1996, Herring and Nilson 1987].

Recommendations for the treatment of partial-thickness tears are still debated. Several studies have come to the conclusion that in general, surgical treatments are not always more beneficial to the patient than conservative treatments [Seida et al. 2010, AHRQ 2010]. This has lead to the recommendation of trying out conservative treatments first, before performing a surgery. Exceptions are severe tears, especially for young patients, where the surgical treatment should not be delayed in order to avoid irreparable rotator cuff damage [Tashjian 2012].

Amongst the rotator cuff muscles, the supraspinatus tendon is the one most often affected by tears [AAOS 2014]. Tears usually manifest as a fraying of the intact tendon at the insertion site on the humeral head. In most cases, the initial partial-thickness tear, symptomatic or asymptomatic at this stage, will enlarge over time, accompanied by arising or worsening symptoms [Tempelhof et al. 1999]. These symptoms include pain, reduced range of motion, and decreased shoulder strength. This has been observed clinically for both symptomatic and asymptomatic supraspinatus tendon tears [McCabe et al. 2005, Kim et al. 2009]. Experimental measurements of the loading capacity of supraspinatus tendons are available [Huang et al. 2005, Matsuhashi et al. 2013]. Cadaveric tendons with intact insertions on the humeral head were loaded up to failure, which occurred most often at the insertional site. Partially torn tendons were however not analysed in these studies. Information on the link between partial-thickness tears and the load bearing capabilities of the supraspinatus would contribute to improving conservative treatments. For example, physiotherapists could use this information to design exercises that are compatible with a patient's specific tendon tear.

Therefore, the goal of this study was to analyse the impact of partial-thickness tears on the loading capacity of the supraspinatus tendon. Assuming a non-linear and anisotropic behaviour of the tendon, we propose a failure criterion calibrated with experimental measurements for our model. The tendon model was used in a finite element model based on magnetic resonance images (MRI) of a healthy volunteer. The loading capacities of the tendon were evaluated for progressing partial-thickness tears.

4.1.2 Methods

The used constitutive equation for the tendon model, its identification with experimental measurements, and the damage criterion are introduced in the following section 4.1.3. The tendon model was then applied in a patient-specific finite element analysis, built upon in vivo magnetic resonance imaging (section 4.1.5). Failure forces were related to muscle force during arm elevation using a musculoskeletal model of the shoulder (section 4.1.4).

4.1.3 Tendon Model

Constitutive Law

The supraspinatus tendon was modelled as an incompressible exponential hyperelastic material with one fibre family. The following strain energy potential was used [Ehret et al. 2011]:

$$\Psi(\mathbf{C}) = \frac{\mu}{4} \left(\frac{1}{\alpha} [e^{\alpha(I_p - 1)} - 1] + \frac{1}{\beta} [e^{\beta(K-1)} - 1] \right) \tag{4.1}$$

where the generalised invariants I_p and K were:

$$I_p = \frac{w_0}{3} \mathrm{tr}\mathbf{C} + w_p \mathrm{tr}(\mathbf{C}\mathbf{M}) \qquad K = \frac{w_0}{3} \mathrm{tr}\mathbf{C}^{-1} + w_p \mathrm{tr}(\mathbf{C}^{-1}\mathbf{M}) \tag{4.2}$$

with the right Cauchy-Green strain tensor $\mathbf{C}$. The structural tensor $\mathbf{M}$ contained the information about the fibre direction $\mathbf{M} = \mathbf{m} \otimes \mathbf{m}$, where $\mathbf{m}$ is a unit vector in the fibre direction.

The first term of the invariant I_p was an isotropic term. The second term of the invariant I_p was the squared fibre stretch and thus associated with longitudinal material properties. The first term of the invariant K was an isotropic term. The second term of the invariant K was the deformation of a surface element perpendicular to the fibre direction in the reference state, and was thus associated with transverse material properties [Ehret et al. 2011].

The derivation of the strain-energy potential gave the following stress-strain relationship in terms of the 2$^{\mathrm{nd}}$ Piola-Kirchhoff stress $\mathbf{S}$:

$$\begin{aligned} \mathbf{S} &= 2\frac{\partial \Psi(\mathbf{C})}{\partial \mathbf{C}} \\ &= \frac{\mu}{2} \left\{ e^{\alpha(I_p - 1)} \left[\frac{w_0}{3}\mathbf{I} + w_p\mathbf{M} \right] - e^{\beta(K-1)} \mathbf{C}^{-1} \left[\frac{w_0}{3}\mathbf{I} + w_p\mathbf{M} \right] \mathbf{C}^{-1} \right\} \end{aligned} \tag{4.3}$$

The equation contained four material parameters: μ, α, β, and w_0. The lower bounds, $\mu, \alpha, \beta > 0$, ensured poly-convexity and coercivity of the constitutive law [Ball 1976]. The stress-free state was associated with the reference configuration, which lead to the link between the weight factors of $w_p = 1 - w_0$ [Ehret et al. 2011].

Parameter Identification

We identified the material parameters μ, α, β and w_0 using experimental data from human cadaveric supraspinatus tendons [Lake et al. 2009; 2010]. Stress-strain curves from a slack position up to failure were available both in the longitudinal and in the transverse direction. We used Matlab's nonlinear least square algorithm lsqcurvefit to fit the nonlinear constitutive equation (eq. 4.3) to the experimental data. The trust region algorithm was used because it allowed us to set lower bounds for the material parameters according to the prerequisites on strain energy functions (sec. 4.1.3). The fitting was performed simultaneously in both the longitudinal and the transverse direction. We launched the least square algorithm with different randomly distributed initial values in the range of [0,100] to verify the detection of a global minimum. The root mean square error was used to assess the quality of the fit in both the longitudinal and the transverse direction with the following formula:

$$RMSE = \sqrt{\frac{\sum_{i=1}^{N}(\sigma_i(\varepsilon_i) - \sigma^*(\varepsilon_i))^2}{N}} \tag{4.4}$$

with the number of experimental measurement points N, the experimentally measured stress σ_i at strain ε_i, and the stress prediction of the constitutive law σ^* at the same strain.

In addition, a variance-based sensitivity analysis on the material parameters was carried out. We followed an approach based on the Monte-Carlo method [Saltelli et al. 2008; 2010]. First, $2N$ random material parameter samples were generated. The material parameters were normally distributed. Mean values were the identified material parameters and the standard deviation was 1. The material parameter samples were saved in two matrices, $\mathbf{A}$ and $\mathbf{B}$, of size $N \times 4$. Further matrices $\mathbf{A}_B^i$, $1 \leq i \leq 4$, were generated, such that the ith column was exchanges with the ith column of matrix $\mathbf{B}$. The remaining columns were equal to matrix $\mathbf{A}$. The six matrices $\mathbf{A}$, $\mathbf{B}$ and $\mathbf{A}_B^i$ provided thus $6N$ material parameter samples. For each material parameter sample the stress-strain curve of the constitutive equation (eq. 4.3) was evaluated. The sensitivity index S was estimated in both longitudinal and transverse direction using the formula [Saltelli et al. 2010]:

$$S_i = \frac{1}{N}\sum_{j=1}^{N} \sigma_{xx}(\mathbf{B})_j \left(\sigma_{xx}\left(\mathbf{A}_B^i\right)_j - \sigma_{xx}(\mathbf{A})_j \right) \tag{4.5}$$

where i specified the analysed material parameter: either μ, α, β, or w_0. $\boldsymbol{\sigma}$ was the Cauchy stress in the longitudinal ($xx = 11$) or transverse ($xx = 22,33$) direction. The term $\sigma_{xx}(\mathbf{B})_j$ described the stress evaluated with the input parameter sample stored in the jth row of matrix
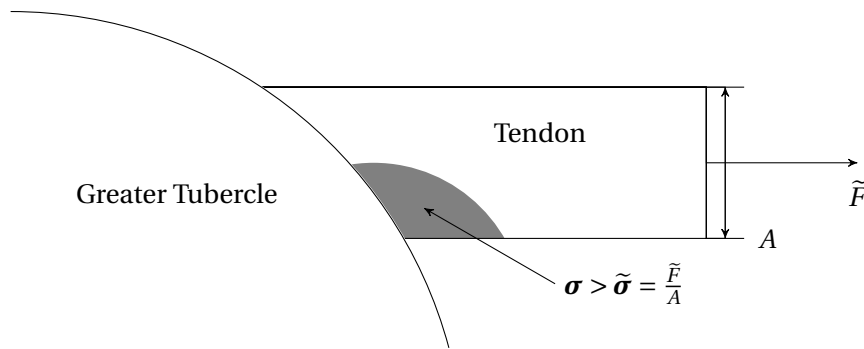
Figure 4.1 – The critical *process zone* (grey) is defined as the volume where the stress exceeded the experimental failure stress $\widetilde{\sigma}$ associated with the failure force $\widetilde{F}$. A was the cross sectional area of the tendon and σ the Cauchy stress.

B, respectively for matrices $\mathbf{A}$ and $\mathbf{A}_B^i$. The number of sample parameters, N, was progressively increased until the computed sensitivity indices showed convergence.

Damage and Failure Criterion

The damage and failure criterion was based on the theory of critical distances [Taylor 2007]. This theory assumes that failure is preceded by the appearance of damage within a *process zone*. In this zone, energy associated with plastic deformation or micro damage is dissipated. Some loading levels can induce damage within a concentrated zone, which increases in size as loading increases until failure. At failure force, the volume of this *process zone* is by definition the critical volume (of the *process zone*). We determined this critical volume by replicating experimental measurements on the supraspinatus tendon[Huang et al. 2005] reporting a failure force of 1007 N and a nominal failure stress of 11.5 MPa. Tendon damage was assumed to occur as soon as the local maximum principal stress reaches the experimental failure stress. The volume containing stresses above the experimental failure stress was defined as *process zone*. The volume of the *process zone* under **failure load** was set as the critical *process zone* volume (Figure 4.1).

4.1.4 Musculoskeletal Model

We used a musculoskeletal model to relate the failure force to the supraspinatus force at 90 degrees of abduction in the scapular plane [Ingram et al. 2012; 2013; 2014, Terrier et al. 2010, Engelhardt et al. 2014]. The arm elevation was simulated with a weight in the hand, starting from 0 N in steps of 10N up to 120 N. The shoulder model was built with the MRI images of the same volunteer (section 4.1.5). The model included thorax, clavicle, scapula and humerus. The bones were linked by spherical joints spanned by 16 muscles: subclavius, serratus anterior (3 parts), trapezius (4 parts), levator scapulae, rhomboid minor, rhomboid major (2 parts), pectoralis minor, pectoralis major (3 parts), latissimus dorsi (3 parts), deltoid (3 parts), rotator

cuff (4 muscles), teres major, and coracobrachialis muscles. Each muscles has been modelled with three cables, which were evenly distributed over the muscle's attachment site. A nullspace optimization algorithm coupled with inverse dynamics solved the unconstrained problem of muscle force distribution. The cost function was the sum of squared muscle stresses.

4.1.5 Application

MRI

A 27 years old male volunteer showing no sign of joint abnormality was used as anatomic reference for this study. We developed a custom MRI protocol consisting of two three-dimensional T1-weighted sequences on a 3 Tesla MRI scanner. The first sequence was a gradient-recalled echo VIBE (TR/TE, 12.2/4.8 ms) and covered the glenohumeral joint with an isotropic resolution of 0.6 mm. The second sequence was a turbo spin-echo SPACE (TR/TE, 600/9.1 ms) and covered the whole right hemithorax with an isotropic spatial resolution of 0.9 mm. We co-registered the two sequences with Amira (FEI Visualization Sciences Group).

The supraspinatus tendon and humerus were reconstructed out of the MRI data (Figure 4.2). The image segmentation was performed manually using Amira. The resulting point clouds were imported into Geomagic for conversion into 3D bodies. The 3D bodies were superposed to the MRI images for visual verification. As the supraspinatus tendon merges with neighbouring tendons and the joint capsule at the lateral end, the tendon tip and its insertion are difficult to distuinguish on MRI images. Therefore, a cadaveric study was additionaly consulted to verify the reconstruction of this region [Curtis et al. 2006]. The 3D bodies were imported into the finite element software Abaqus (Dassault Systèmes Simulia Corp., Providence, RI, USA) for stress analysis.

Finite Element Model

The constitutive equation (eq. 4.3) was implemented into an user material subroutine (UMAT) in the finite element software Abaqus. To achieve an incompressible material behaviour, a penalty method was implemented [Holzapfel 2000]. The UMAT implementation required the specification of the consistent elasticity tensor $\mathbb{C}$. Abaqus defined $\mathbb{C}$ using the Jaumann derivative, which is given in incremental form by the formula:

$$\delta\boldsymbol{\sigma} = \mathbb{C} : \delta\mathbf{D} + \delta\mathbf{W}\boldsymbol{\sigma} - \boldsymbol{\sigma}\delta\mathbf{W} \tag{4.6}$$
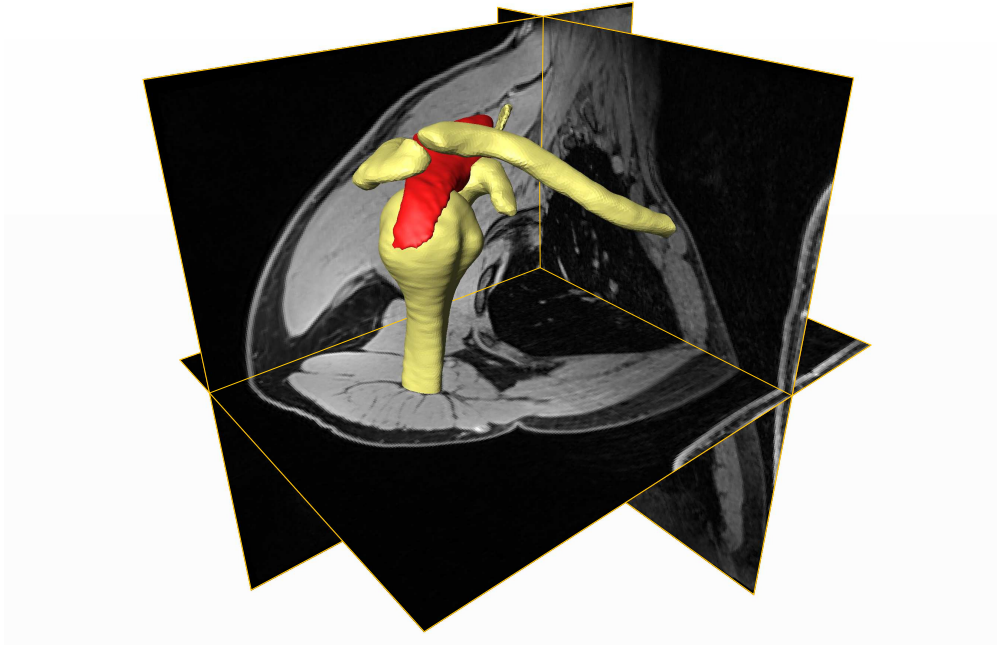
Figure 4.2 – Reconstruction of the clavicle, scapula, humerus and supraspinatus tendon from MRI. The bones are shown in yellow and the supraspinatus muscle-tendon unit in red. Three MRI slices are shown as reference.

where $\boldsymbol{\sigma}$ denoted the Cauchy stress, $\mathbf{D}$ was the rate of deformation tensor and $\mathbf{W}$ the spin tensor. $\delta\mathbf{D}$ and $\delta\mathbf{W}$ were:

$$\delta\mathbf{D} = sym(\delta\mathbf{F}\mathbf{F}^{-1}) \qquad \delta\mathbf{W} = asym(\delta\mathbf{F}\mathbf{F}^{-1}) \tag{4.7}$$

with the deformation gradient $\mathbf{F}$.

To calculate $\mathbb{C}$, we used a numerical approximation. We applied small perturbations on $\mathbf{F}$ as proposed by Miehe [Miehe 1996]:

$$\delta\mathbf{F} = \frac{\epsilon}{2}(e_i \otimes e_j\mathbf{F} + e_j \otimes e_i\mathbf{F}) \tag{4.8}$$
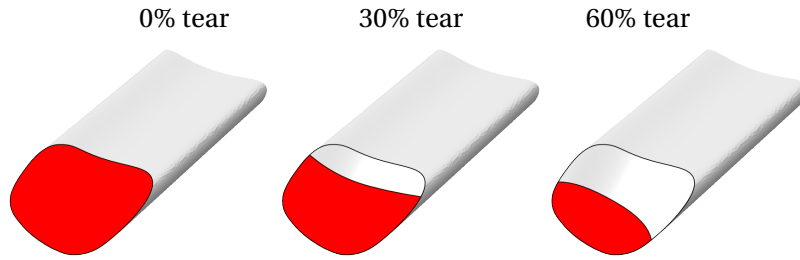
Figure 4.3 – Illustration how tendon tears were modelled. The red part of the insertion is attached to the humerus. On the left, an intact insertion is shown, in the middle a 30% tear, and on the right a 60% tear respectively.

where ϵ was a parameter perturbation, which was set according to Miehe [Miehe 1996]. Inserting equation 4.47 into equation 4.7 lead to:

$$\delta \mathbf{D} = \frac{\epsilon}{2}(e_i \otimes e_j + e_j \otimes e_i) \qquad \delta \mathbf{W} = 0 \tag{4.9}$$

The incremental change in stress was approximated by the forward difference:

$$\delta \boldsymbol{\sigma} = \boldsymbol{\sigma}(\mathbf{F} + \delta \mathbf{F}) - \boldsymbol{\sigma}(\mathbf{F}) \tag{4.10}$$

The elasticity tensor could then be approximated with the formula:

$$\mathbb{C}_{ijkl} = \frac{\boldsymbol{\sigma}(\mathbf{F} + \delta \mathbf{F})_{ij} - \boldsymbol{\sigma}(\mathbf{F})_{ij}}{\delta \mathbf{D}_{kl}} \tag{4.11}$$

Taking advantage of symmetry properties, it was sufficient to apply the perturbation $\delta \mathbf{F}$ in six directions 11, 22, 33, 12, 23, 13 to achieve all components of $\mathbb{C}$.

The tendon was attached to the humeral head at the insertion site on the greater tubercle [Curtis et al. 2006]. The proximal humerus was assumed to be isotropic linear elastic. The Young's Modulus was set to 10.4 GPa and Poisson's ratio to 0.3 [Rho et al. 1993].

To simulate partial-thickness tears of the supraspinatus tendon, the insertion area between the supraspinatus tendon and the humerus was decreased, starting from the articular-sided fibers (Figure 4.3). A 0% tear described an intact insertion, a 50% tear indicated the insertion area was reduced by half, and a 100% tear meant the complete detachment of the tendon respectively.

The deformable parts were meshed with quadratic tetrahedral elements. The mesh size has been evaluated using the strain energy as convergence criterion.

To analyse damage and failure force, we considered a static position at 90 degrees of arm elevation in the scapular plane. Assuming a scapulo-humeral rhythm of 2:1, the scapula was rotated by 30 degrees and the humerus by 60 degrees relative to the scapula. The supraspinatus muscle force applied to the tendon was increased from 0 N up to the failure force. Tendon strains were recorded and the size of the *process zone* determined.

4.1.6 Results

The identified material parameters for the constitutive law (table 4.1) were independent of the initial values of the least square algorithm. The longitudinal and transverse root mean square errors were 11.24 and 1.46, respectively. The sensitivity analysis showed no interactions between the parameters ($\sum_i S^i = 1$). The parameter w_0 had the highest sensitivity index.

	μ	α	β	w_0
material parameter	29.085 MPa	13.244	0.0	0.812
sensitivity index	0.02	0.13	0.0	0.85

Table 4.1 – Results for material parameters and corresponding sensitivity indices.

During progressive loading, the *process zone* was present at the deep articular-sided fibers at 60% of the failure force or more. As force increased, the *process zone* extended more in the longitudinal than in the transverse direction. The calibration of the tendon failure criterion lead to a critical *process zone* volume of 62 mm^3, which was set as the failure criterion for subsequent tests (Figure 4.4).

The failure force decreased for increasing partial-thickness tears (Figure 4.5). For tears between 10% and 20%, the failure force decreased less than 1%. Above 20% tear, the failure force decreased by as much as 92.5% at 90% tear. A gap appeared between the tendon tear and the bone. As force increased, the *process zone* initiated at the deep articular-side of the reduced insertion. The *process zone* then extended more in the longitudinal than in the transverse direction, until the critical volume was reached.

4.1.7 Discussion

To better understand the consequences of tears in the supraspinatus tendon, we analysed the effect of partial thickness tears on the tendon's load bearing capability. The analysis focused on the supraspinatus's tendon insertion on the greater tubercle of the humerus. A numerical
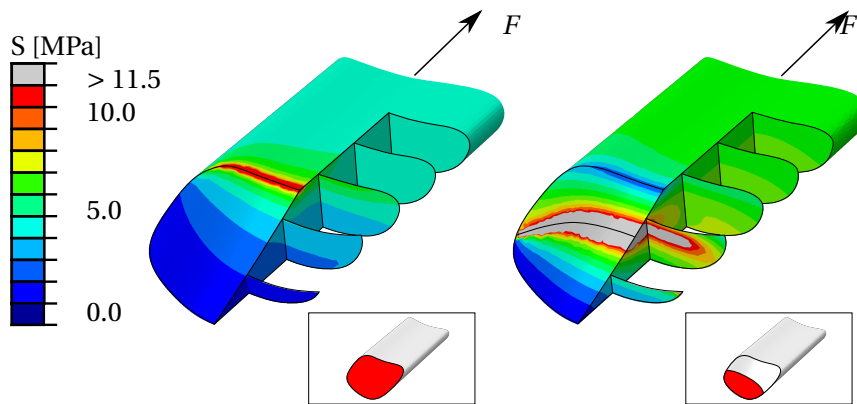
Figure 4.4 – Stress distribution in the tendon close to its insertion on the greater tubercle of the humerus. On the left, the results for an intact insertion are shown; on the right are the results for a 50% torn tendon. Both cases are loaded with 450 N, corresponding to an abduction with 100 N in the hand. The *process zone* ($\sigma > 11.5$ MPa) is shown in grey

model based on MRI images of a young person was developed. We considered an anisotropic hyperelastic constitutive law, and a damage and failure criterion for the tendon. The material parameters were identified using experimental data. Partial thickness tears of increasing size were progressively loaded until the failure criterion was reached. The predicted failure force was related to the estimated active force of the supraspinatus muscle during weight lifting.

Several constitutive laws for the tendon have already been proposed assuming hyperelastic, viscoelastic, or microstructural properties [Pioletti et al. 1998, Holzapfel and Gasser 2001, Weiss et al. 2005]. The constitutive law chosen for this study fulfilled the prerequisites on polyconvexity and coercivity of strain energy functions [Ball 1976, Holzapfel 2000], which are well documented [Ehret and Itskov 2007]. The strain energy potential has further the advantage not to be based on additive split of isotropic and anisotropic components [Ehret et al. 2011], as other laws proposed in literature [Holzapfel et al. 2000, Balzani et al. 2006]. The additive split has the disadvantage, that under compression in fibre direction, the anisotropic part has to be switched off to guarantee convexity of the strain energy potential [Ehret and Itskov 2007]. This leads to an isotropic behaviour when fibres are under compression. On the other hand, a bi-linear equation might better replicate the toe region at the beginning of tendon stress strain curves. However, our work did not focus on the transition from a tendon slack state to a loaded configuration.

Concerning the material parameter identification, we assumed that the nonlinear least square algorithm found a global minimum, since changing the initial values did not influence the result. The parameter β was the only parameter to remain on the lower bound of 0. β appears in the second term of the strain energy potential (eq. 4.1) and the term vanishes as β approaches zero. This the strain potential is reduced to its first term and becomes an
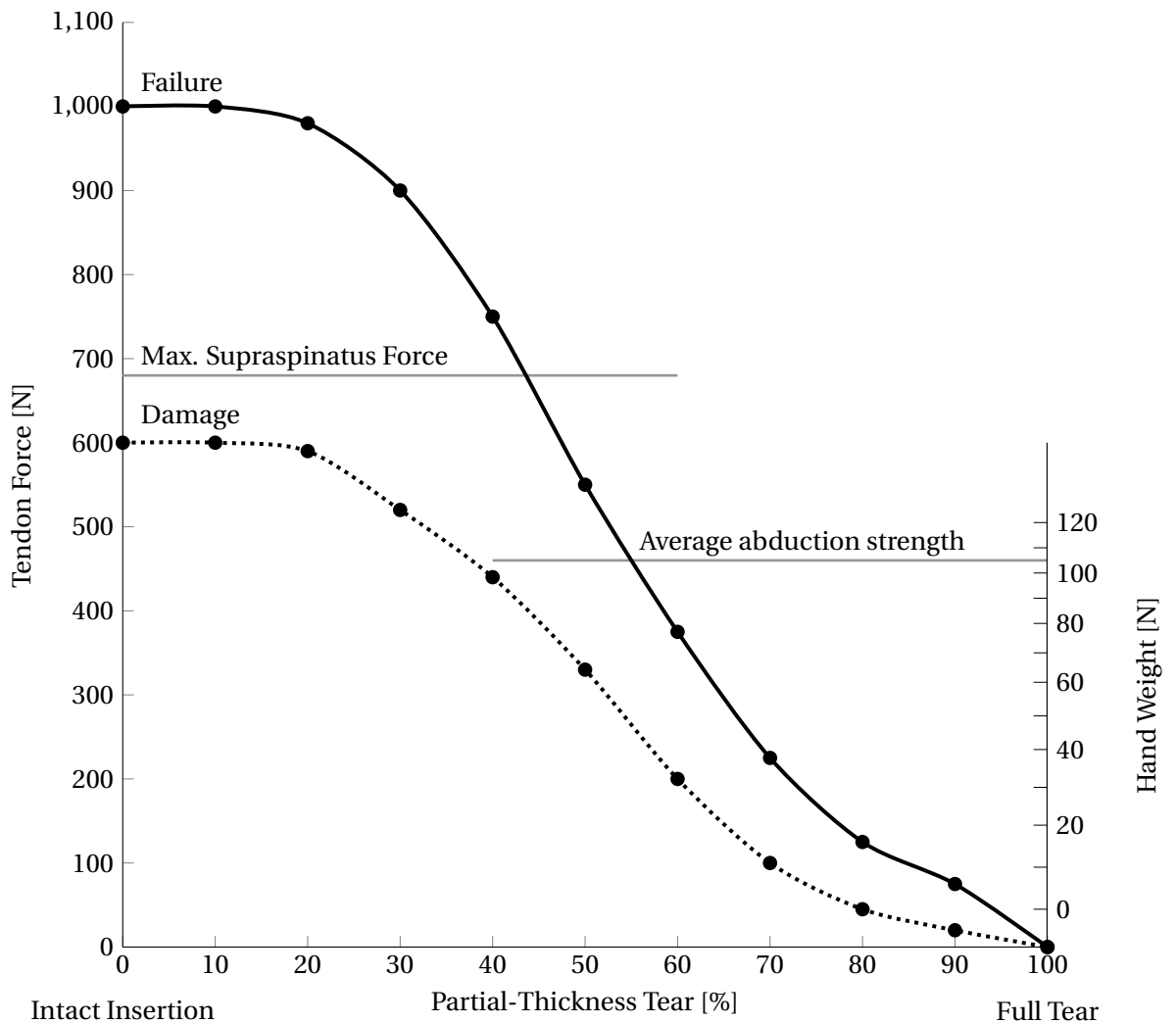
Figure 4.5 – Failure forces for increasing tears (*process zone* volume = critical volume) and damage initiation (*process zone* volume = 10% critical volume). The forces are compared to supraspinatus forces during loaded abduction and to the theoretical maximum supraspinatus force.

exponential function with the invariant I_p (eq. 4.2). We can thus conclude that it is sufficient to model the supraspinatus tendon using constitutive laws that consider the tissue as an isotropic matrix traversed by one fibre family. Additional terms for the transverse plane were indeed not required to match the experimental data.

The quality of the parameter identification (RMSE) was better in the transverse than in the longitudinal direction. This was related to a greater variance in the longitudinal experimental data compared to the transverse data. The sensitivity analysis proved that the parameter with the most influence was w_0. This parameter is a weight factor characterizing the relative importance of the fiber anisotropy over the isotropic matrix.

We calibrated the failure model with experimental data providing the failure stress. We chose this study, because it was the only one reporting ultimate failure on complete tendons attached to the greater tubercle, while other studies used morphologically split tendons [Matsuhashi et al. 2013] or dissected tendon samples detached from bone [Lake et al. 2009; 2010]. We observed however a great difference in failure stresses reported by these studies, which could be ascribed to different methods of sample preparation, testing procedure and natural property variation in biological soft tissues.

In the calibration simulation, the *process zone* initiated at the deep articular-sided aspect of tendon insertion. This is consistent with clinical observations, as well as with experimental studies reporting that tears occur most often at this site [Matsuhashi et al. 2013]. The load initiating the *process zone* was dependent on the finite element mesh. This was related to the fact that loaded edges represent stress concentration points and lead to singularities in the finite element mesh where the elastic strains and stresses are theoretically infinite. However, the evolution and the final volume of the *process zone* was independent from the finite element mesh as soon as the *process zone* volume exceeded 10 % of the critical volume at ultimate failure.

The critical distance approach used here to predict failure has the advantage of simplicity. It indeed only requires the elastic stress field around the stress concentration and one experimental tensile test for calibration [Taylor 2007]. Although this method was initially developed for brittle materials, we justified its use in our work by the fact that stress-strain curves for tendon tissue show sudden failure without preceding plastic straining. This hypothesis has already been successfully used in micro structural [Liao and Belkoff 1999, Weiss et al. 2005] and probabilistic [De Vita and Slaughter 2007, Guo and Vita 2009] models where brittle failure at fibre level is assumed as soon as a limit strain is exceeded. There are two alternatives of modelling failure: using cohesive element techniques, or adding damage terms in the constitutive equations. For cohesive elements, the path of crack evolution needs to be known in advance. Constitutive equations with damage terms require further experimental measurements of tissue softening at failure.

The finite element implementation of the constitutive law used a numerical approximation for the calculation of the elasticity tensor. This tensor serves as an iteration operator for the finite element solver. It thus only influences the convergence speed and not the final result [Miehe 1996]. However, when this approximation might lead to convergence issues when used in more complex loading cases. It might then be necessary to implement an analytical formulation of the elasticity tensor to provide stable and fast convergence.

The predicted load-bearing capacity was consistent with experimental studies on decreased abduction strength of asymptomatic and symptomatic patients with supraspinatus tendon tears [Kim et al. 2009, McCabe et al. 2005]. In both studies, small and medium size tears did not significantly decrease abduction strength. However, significant deficits in abduction strength were observed for large and massive tears. In addition, the model predicts a tendency

of initial tears to further expand, because the highest tissue loadings were always located at the torn side of the reduced insertion. The model further predicted arising gaps even in slight tears which would prevent self-reattachment and healing. However, the predicted forces are unlikely to be reached by patients, as increasing pain is the main limiting factor for abduction strength in patients with shoulder disorders [Kirschenbaum et al. 1993, Ben-Yishay et al. 1994, Oh et al. 2010].

The obtained supraspinatus forces lie in the range of other numerical muscle force computation algorithms [Engelhardt et al. 2014, Yanagawa et al. 2008], although some numerical studies reported supraspinatus forces to be less than half [van der Helm 1994] or more than twice as high [Favre et al. 2012] as the results reported in this study. In either case, using optimization based muscle force estimation risks underestimating the supraspinatus force since optimization based methods tend to underestimate stabilizing muscle activity [Engelhardt et al. 2014]. The load cases were chosen following an experimental study on the abduction strength of average middle-aged people [Kim et al. 2009], this was 102 N at the outstretched arm at 90 degrees abduction.

Given the results of the load bearing capacity analysis, one can see that failure forces decrease following a sigmoidal function (Figure 4.5). The curve shows a plateau between 0% and 20% tear. Then, the slope decreases and reaches its minimum value between 40% and 60% tear. Above 60% tear the curve flattens again. We thus assume that tears sizes between 40% and 60% represent a turning point in the evolution of tears: below 40% tear, the loading capacity stays above the theoretical maximum supraspinatus force of 688 N [Garner and Pandy 2000]. Above 60% the loading capacity dropped below the average abduction strength of 92 Nm, which corresponded to holding 10.5 kg in the hand [Kim et al. 2009].

The strength of this work is that it models the supraspinatus tendon with an anisotropic hyperelastic law identified with experimental data. The singularity associated with the tear was treated with the critical distance method, which was also calibrated with experimental data. However, stress near the insertion might be overestimated, as the model does not include the cartilaginous tissue found at the transition between bone and tendon. Although this layer is very small [Clark and Stechschulte 1998, Benjamin et al. 2006], this tissue might have a damping effect. Also, the inhomogeneity of the tendon in the transverse plane could not be included in the model due to lack of experimental data for identification of material parameters. The model could be further extended by modelling the whole supraspinatus muscle-tendon unit during movements of daily living and taking into account dynamic and fatigue failure effects.

In conclusion, we studied in a numerical analysis the reduced loading capacity of supraspinatus tendon tears. According to the numerical results, with smaller than a 40% tear, conservative treatment strategies and physiotherapy with additional weights in the hand can be considered. However, above a 60% tear, surgery should be considered to restore the loading capacities of the tendon. These results should be further investigated and confirmed by additional

numerical and clinical studies. The numerical model could then be applied to patients to test further hypotheses related to rotator cuff tears. The insight into tendon mechanics will then contribute to the improvement of treatment strategies for patients.

4.2 Extension of Tendon Model

The model presented in the previous section predicted tendon strains at an arm position of 90°abduction. However, 90 % of our daily shoulder movements stay below 60°abduction [Coley et al. 2008]. We thus extended the tendon model to provide values for tendon strains at different degrees of abduction. The final model had further the ability to analyse the subacromial space.

4.2.1 Introduction

Rotator cuff conditions are a frequent diagnosis in patients reporting shoulder pain or reduced mobility. Among the rotator cuff muscles, the supraspinatus is the most often affected, especially its tendon [American Academy of Orthopaedic Surgeons 2014]. Two scenarios of tears are reported: first, tendon tears close to the insertion on the humeral head. Second, the impingement syndrome, where the tendon gets squeezed between the scapula acromion and the humeral head [Tempelhof et al. 1999, Michener et al. 2003].

The pathogenesis of these shoulder conditions are multicausal and not fully understood yet [Kannus and Jozsa 1997, Renström and Hach 2005]. Repeated overloading might lead to micro traumata that induce inflammation and tissue alteration if not healed out completely. Workers and athletes with overhead activities and individuals with a prehistory of shoulder trauma or long time immobilisation of the arm are especially at risk. Both tears at the insertion and the impingement syndrome start with a fraying of the tendon. The tear enlarges over time accompanied by arising or worsening symptoms. Inflammation and swelling worsen the situation, especially for the impingement syndrome, where pressure and friction on the tendon increases due to decreased subacromial space.

To better understand the circumstances that lead to the above described shoulder conditions, knowledge about physiological and unphysiological tendon strains is important. In vivo measurements using an ultrasound tracking technique are reported [Kim et al. 2011]. Maximum tendon strains of 15.7% during abduction were measured at the articular side of the tendon. However, this in vivo study did not measure strains at the insertion, where tears occur most often [Miller et al. 2014]. Tendon strains at the insertion were measured by a cadaveric study using an MRI based deformation tracking method. The strains measured with this method were lower than in the in vivo study. The difference in measured strains might be related to different tendon loads.

In this section, we present a numerical model of the glenohumeral joint including the supraspinatus tendon to calculate tendon strains and to analyse subacromial contact during movements. This part of the work describes further developments of the tendon model introduced in section 4.1. The extended model is not limited to an arm position at 90°abduction, but has the ability to estimate tendon strains at different degrees of arm elevation. It further analyses the subacromial space and an eventual contact between the tendon and the acromion. First results for an abduction movement in the scapula plane are presented.

4.2.2 Tendon Model

Anatomy

The tendon geometry was reconstructed out of the same MRI data used for the musculoskeletal upper limb model (Section 2.2) and the cartilage model (Section 3). The MRI data represented the tendon in a rest position wrapping around the humeral head. The segmentation was performed manually using the Amira software (FEI Visualization Sciences Group, France). Close to its insertion, the segmentation of the tendon and the definition of its footprint on the humeral head were verified with a cadaveric dissection study [Curtis et al. 2006]. The reconstructed geometry was imported into Geomagic (3D Systems, USA) for surface construction. Solidworks (Dassault Systèmes, France) was used for conversion into a volumetric 3D body. The final geometry was superposed with the MRI data for visual verification.

Tissue Modelling

For the analysis of tendon tissue deformation, the constitutive law and its UMAT implementation described in section 4.1.3 was used. The material parameters were taken from section 4.1.6. The rest position of the arm (along the chest) was assumed to be a stress free state of the tendon. The tendon fibres were assumed to be parallel to each other and perpendicular to the cross sectional planes of the tendon. The orientation of the cross sectional plane minimized the cross sectional area of the tendon. Then, a cubic cardinal spline was defined through the midpoints of the tendon's cross sections. The following formula for the spline interpolation was used:

$$p(u)_i = \begin{bmatrix} 1 & u & u^2 & u^3 \end{bmatrix} \begin{bmatrix} 0 & 1 & 0 & 0 \\ -\tau & 0 & \tau & 0 \\ 2\tau & \tau-3 & 3-2\tau & -\tau \\ -\tau & 2-\tau & \tau-2 & \tau \end{bmatrix} \begin{bmatrix} P_{i-2} \\ P_{i-1} \\ P_i \\ P_{i+1} \end{bmatrix} \qquad (4.12)$$

with $u \in (0, 1)$, the tension parameter τ which was set to 0.5, and the control points $P_{i-2}, P_{i-1}, P_i, P_{i+1}$. For each integration point in the finite element mesh, the tendon fibre direction was defined by the tangent direction of the point on the spline closest to the integration point (Figure 4.6).
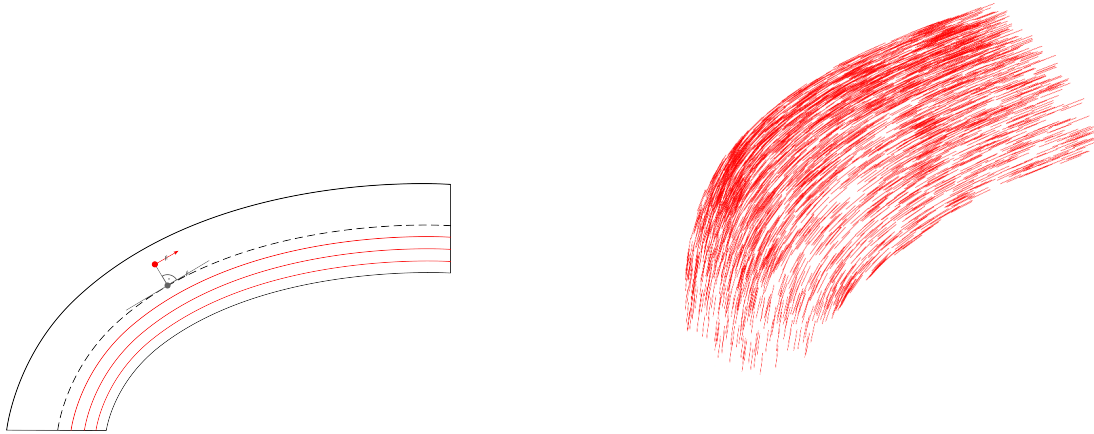
Figure 4.6 – Modelling the fibre distribution in a finite element model of the supraspinatus tendon. A spline (dashed line) is constructed through the cross section midpoints. At each finite element integration point (red point) the fibre direction is assumed to be parallel to the tangent direction of the closest point on the spline (grey point). The right image shows the resultant fibre distribution in the finite element model: at each finite element integration point a unit vector in fibre direction was drawn.

4.2.3 Finite Element Model

The finite element model included the supraspinatus tendon, the humeral head, and the scapula. The model was built in the reference frame of the scapula as defined by the standard of the International Society of Biomechanics (ISB) [Wu et al. 2005]. The scapula was thus fixed in space and the humeral head moved relatively to it. The humeral rotations and translations were taken from the cartilage model (Chapter 3). A frictionless contact allowing no penetration was defined between the tendon and the humeral head to reproduce the wrapping of the tendon around the humeral head. A second contact was defined between the tendon and the scapula acromion to evaluate a potential contact between these two structures. The tendon was meshed with quadratic tetrahedra elements. Mesh size and convergence were evaluated during a mesh study using the strain energy as convergence criterion.

We simulated an abduction movement of the arm in the scapula plane from a rest position up to 90°arm elevation. During the movement, the tendon was loaded with supraspinatus forces calculated with the musculoskeletal upper limb model described in section 2.2. Tendon strains were analysed. We further observed, if the tendon was in contact with the acromion during the movement.

4.2.4 Results

The strain distribution showed increasing strains from the bursal to the articular side of the tendon during the whole abduction movement. The highest tensile strains were located at the articular side of the insertional area and reached 12.6% at 90°abduction (Figure 4.7, left image).

During the whole movement, the tendon did not touch the acromion. The minimum distance between tendon and acromion was 1.2 mm at 30°of abduction (Figure 4.7, right image).
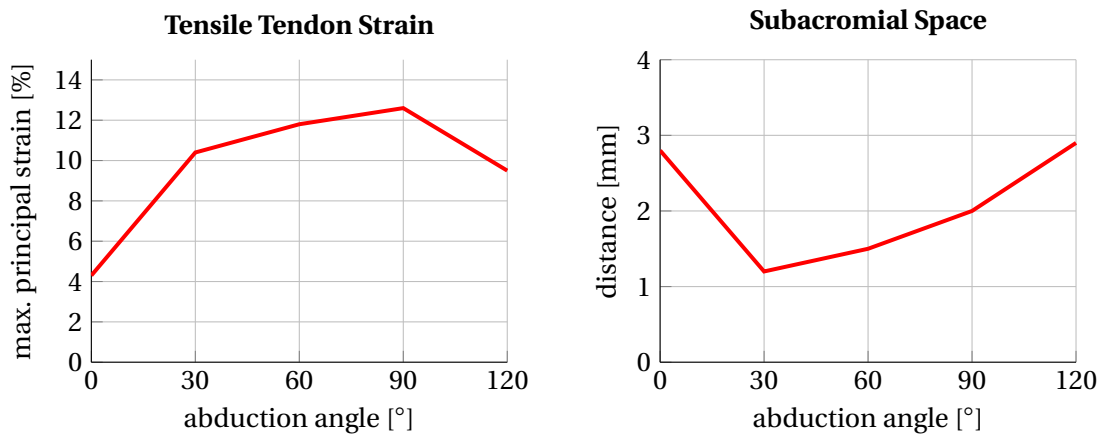
Figure 4.7 – On the left, the strain distribution in the supraspinatus tendon at 90°abduction is shown. On the right, the humeral head in its most superior position at 30°abduction. The distance between tendon and acromion is 1.2 mm.

4.2.5 Discussion

Supraspinatus tendon tears are frequent conditions in patients suffering from shoulder pain and reduced mobility. To analyse biomechanical contributions to the pathogenesis of those tears, we developed a numerical model of the glenohumeral joint which has the ability to estimate supraspinatus tendon strains. The model was built upon in vivo MRI data. The tendon was modelled with a hyperelastic anisotropic constitutive law. The fibres were assumed to be parallel and perpendicular to the tendon's cross section. Tendon strains and subacromial space were analysed during a simulated abduction movement.

The tendon model presented in this section is the third model of a series of numerical shoulder models. The first model, which is the musculoskeletal upper limb model described in chapter 2, estimates muscle forces. The second model, the cartilage model described in chapter 3, computed glenohumeral contact patterns and humeral head translations with the given muscles forces. The tendon model takes the supraspinatus forces and humeral head translations as input to estimate supraspinatus tendon strains. All three models were built upon the same

in vivo MRI data and are thus consistent from a geometrical point of view. The decoupling into three models was necessary to reduce the complexity to a manageable level.

While the model presented in section 4.1 was limited to an arm position at 90°abduction, the extended model has the ability to evaluate tendon strains and subacromial space over the whole range of arm elevation. The extension was motivated by kinematic studies on shoulder movement in daily live showing that 90% of our shoulder movements take place below 60°arm elevation [Coley et al. 2008]. The assumption, that the chronic degenerative process leading to tendon tears initiates during movements of daily living, necessitates tendon strain analysis in low arm elevation ranges.

The tendon geometry has been reconstructed out of in vivo MRI of a young volunteer showing no sign of shoulder pathology. We assume thus to have imaging data of a healthy supraspinatus tendon. The MRI images had a resolution of 0.6 mm, which was the minimum value obtainable with the available 3 Tesla scanner. Higher resolution would require a MRI scanner with a stronger magnetic field or the use of computer tomography. Increasing the resolution would allow a more precise reconstruction of scapula, humeral head and the supraspinatus muscle-tendon complex. However, both in MRI and CT images, the tendon close to its insertion on the humeral head can not be distinguished from the joint capsule, with which it merges at this site. Further the insertion on the humeral head is difficult to localize on medical imaging, as there is no clear border between tendon and bone tissue but rather a transition zone. We solved this situation by consulting a cadaveric dissection studies [Curtis et al. 2006].

The parameters of the anisotropic hyperelastic tendon model were identified with experimental data on uniaxial loading in both longitudinal and transverse direction. However, no experimental data could be found on tendon material properties under compression, which occurs p.e. when the tendon wraps around the humeral head. The model predictions of the tendon compression must be interpreted with caution.

The theory of hyperelasticity in continuum models requires the existence of an undeformed stress free state at which the strain energy vanishes. This is unlikely to be the case in fibrous biological tissues [Fung 1973, Peña et al. 2006]. In contrast, there is a distribution of non-zero stresses in the different components of the tissue, that cancel each other out so that the overall stress remains small. These counteracting micro stresses provide stability and create damping properties. On global view of the tendon, it has a great range of deformations, especially in bending loading conditions, under which the restoring forces remain small. The explanation can again be found in the structure of the tendon: fibres have the ability to slide between each other which leads to a relaxation of the tissue (Figure 4.8). A fact that can not be captured by a continuum model. Tendon stresses and restoring forces due to bending might thus be overestimated by the continuum model.

Besides the hypothesises related to continuum mechanics, we assumed the tendon fibres to be parallel and perpendicular to the tendon cross section. Dissection studies on the supraspinatus muscle revealed its complex fibre architecture and a visual split into a posterior
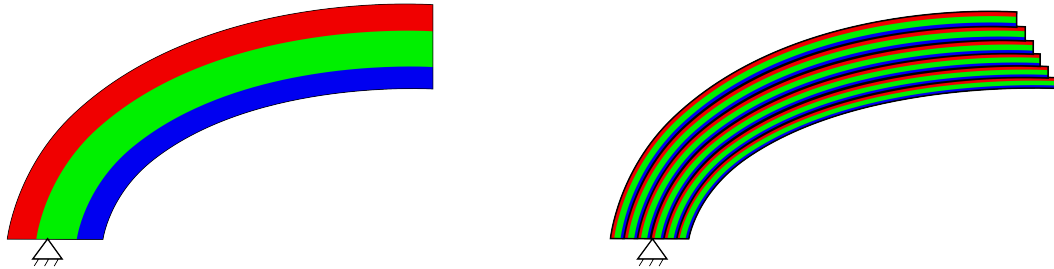
Figure 4.8 – Bending of a tendon. Schematic stress predictions of a continuum model (left) and a microstructural model (right).

and anterior part [Kim et al. 2007]. This split continues in the supraspinatus tendon and has not been taken into account in the numerical model. Other studies have shown that the anterior and posterior supraspinatus tendon do also differ in material properties [Huang et al. 2005, Lake et al. 2009; 2010, Matsuhashi et al. 2013]. The inhomogeneity could not be included into the model due to the lack of experimental data. The only study which analysed the region wise longitudinal and transverse properties of the tendon was done by [Lake et al. 2009; 2010]. More studies of that kind should be done to allow the complete identification of inhomogeneous supraspinatus tendon models.

The supraspinatus muscle force was applied on a cross section of the tendon, although dissection studies have shown that parts of the tendon deeply penetrate the muscle [Kim et al. 2007]. EMG data of the supraspinatus have also shown, that anterior and posterior part are not equally activated during movements. The force transition into the tendon is consequently not homogeneous. In addition with the sliding of the supraspinatus muscle in the scapula notch, the tendon might be guided differently compared to a force pointing to the midpoint of the supraspinatus muscle origin. The joint capsule and the neighbouring tendons of infraspinatus and subscapularis might also act as guiding structures. The tendon position in reality might be different than predicted by the numerical model due to the lack of the neighbouring components.

Compared to in vivo measurements of supraspinatus tendon strains during abduction movements, the peak strains predicted by the numerical model (12.6 %) are in the same range as the experimental values (15.69 ± 2.38 %) [Kim et al. 2011]. The experimental study also confirmed the strain distribution saying that maximum peak strains were located at the articular side of the tendon as predicted by the numerical model. However, the experimental study measured higher strains in the central and superficial regions of the tendon. This again is related to the

continuum model: in tendon tissues, the load transfer between fibres is limited because of the sliding in between them. A fibre consequently transfers its load in the longitudinal direction from its origin to the insertion leading to an almost equal strain distribution in the whole tendon as reported by the experimental study. In the continuum model however, the load is transferred without limitations in the transverse plane leading to strain concentrations at the deep side of the tendon and low strain in central and bursal regions.

The analysis of tendon impingement showed no contact between the tendon and the scapula acromion. It might be an accidental fact that the anatomic data had an acromion cover shaped in a way to provide sufficient space for underlying structures. On the other hand, the musculoskeletal upper limb model (Chapter 2) used for muscle force estimation included a stability criterion. The stability criterion was calibrated in such a way, that the cartilage model (Chapter 3) provides a stable contact pattern, in other words no subluxation during normal movements. As the cartilage model did not include the labrum, ligaments and joint capsule, the range of stable humeral head translations might be underestimated. In consequence the stability criterion might be too strict and the predicted humeral head translations too small.

The strength of the present work was the detailed reconstruction of the supraspinatus tendon from in vivo MRI and the modelling of its mechanical behaviour with an anisotropic hyperelastic constitutive law. The material parameters were identified with experimental data from loading in longitudinal and transverse direction. The predictions for uniaxial loadings are thus reliable. However under a bending loading micro structural effects such as intra fibre sliding come into play which can not be considered by our continuum mechanic models. From a conceptional point of view a microstructural model should be superior for the simulation of complex loading scenarios. The model could be further improved by taking into account the inhomogeneous material properties of the tendon with respecting the anterior-posterior split. Doing this, the force transmission from the muscle into the tendon should also be improved by considering the anterior-posterior split of the supraspinatus muscle in the muscle force estimation process.

In conclusion, we propose a model of the supraspinatus tendon to evaluate tissue strains and tendon impingement during arm abduction. Although the numerical model has a lot of potential for improvement, the obtained tendon strains can be used as reference value when comparing pathological scenarios to the healthy case. The results should further be investigated by numerical and clinical studies. With a deeper understanding of tendon mechanics, load and deformation during activities of daily living, prevention and treatment of supraspinatus tendon conditions could be improved.

4.3   Conclusions

The numerical modelling of biological soft tissues remains a challenging task. The first challenge is to capture the complex mechanical behaviour in a constitutive equation, which requires deep knowledge in advanced engineering mechanics and the related mathematical

background. The more detailed the constitutive law, the more parameters need to be identified with experimental data. This leads to a second challenging task, especially when modelling human tissue: high sample numbers are difficult to obtain, which restricts the number of identification experiments. On the other hand, sufficient repetition is necessary to face the natural variability of tissue properties.

In this chapter, a continuum model of the supraspinatus tendon has been presented. In static positions, the strains predicted by the model were in the range of experimental data. However, the predicted strain distribution during movements differed from experimental findings. This limitation lies in the nature of continuum models, that handle effects related to microstructural behaviour such as fibre sliding. Future research and development should in the author's opinion focus on the development of microstructural simulation models. Future models should also aim to not include single tendons in articulation models, but also neighbouring tissues which might act as guiding structures.

The underlying assumption for tendon damage was to treat supraspinatus tears as overloading injuries. A more complete damage model including fatigue development and compression damage might give further insight to the development of tendon tears.

Despite these limitations, the presented model could predict strains in the range of experimental works. Peak strains were predicted at sites were supraspinatus tendon tears most frequently occur. In the following, this model will be used to evaluate tendon strains in dependence of anatomic parameters.

4.A Appendix

This appendix presents mathematical details on the calculation of elasticity tensors. First, construction of and products with 4th order tensors are summarized. As the analytical calculation of elasticity tensors mainly means derivation of a stress function, the principles of deriving tensor functions are summarized in the next section. Further, the special case of corotational derivation of a stress function is discussed. The last section presents a formula to numerically approximate elasticity tensors in a corotational framework.

4.A.1 Tensor Algebra

Construction out of two 2nd order tensors

To built a 4th order tensor out of two 2nd order tensors, the following four products can be defined:

$$
\begin{aligned}
\boldsymbol{A} \otimes \boldsymbol{B} &= A_{ij} B_{kl} \, \boldsymbol{e}_i \otimes \boldsymbol{e}_j \otimes \boldsymbol{e}_k \otimes \boldsymbol{e}_l \\
[\boldsymbol{A} \otimes \boldsymbol{B}]_{ijkl} &= A_{ij} B_{kl}
\end{aligned}
\tag{4.13}
$$

$$
\begin{aligned}
\boldsymbol{A} \underline{\otimes} \boldsymbol{B} &= A_{ik} B_{jl} \, \boldsymbol{e}_i \otimes \boldsymbol{e}_j \otimes \boldsymbol{e}_k \otimes \boldsymbol{e}_l \\
[\boldsymbol{A} \underline{\otimes} \boldsymbol{B}]_{ijkl} &= A_{ik} B_{jl}
\end{aligned}
\tag{4.14}
$$

$$
\begin{aligned}
\boldsymbol{A} \overline{\otimes} \boldsymbol{B} &= A_{il} B_{jk} \, \boldsymbol{e}_i \otimes \boldsymbol{e}_j \otimes \boldsymbol{e}_k \otimes \boldsymbol{e}_l \\
[\boldsymbol{A} \overline{\otimes} \boldsymbol{B}]_{ijkl} &= A_{il} B_{jk}
\end{aligned}
\tag{4.15}
$$

$$
\begin{aligned}
\boldsymbol{A} \odot \boldsymbol{B} &= \frac{1}{2} (\boldsymbol{A} \underline{\otimes} \boldsymbol{B} + \boldsymbol{A} \overline{\otimes} \boldsymbol{B}) \\
[\boldsymbol{A} \odot \boldsymbol{B}]_{ijkl} &= \frac{1}{2} (A_{ik} B_{jl} + A_{il} B_{jk})
\end{aligned}
\tag{4.16}
$$

Products with 2nd order tensors

Left and right single dot product:

$$\mathbb{A} \cdot \boldsymbol{B} = A_{imkl} B_{mj} \, \boldsymbol{e}_i \otimes \boldsymbol{e}_j \otimes \boldsymbol{e}_k \otimes \boldsymbol{e}_l$$
$$\boldsymbol{B} \cdot \mathbb{A} = B_{im} A_{mjkl} \, \boldsymbol{e}_i \otimes \boldsymbol{e}_j \otimes \boldsymbol{e}_k \otimes \boldsymbol{e}_l \tag{4.17}$$

Double dot product or double contraction:

$$\mathbb{A} : \boldsymbol{B} = A_{ijkl} B_{kl} \, \boldsymbol{e}_i \otimes \boldsymbol{e}_j$$
$$\boldsymbol{B} : \mathbb{A} = B_{ij} A_{ijkl} \, \boldsymbol{e}_k \otimes \boldsymbol{e}_l \tag{4.18}$$

4.A.2 Tensor functions

Functions that have tensors as arguments and a scalar, vector or tensor as return value are called tensor functions.

Scalar valued tensor function

Let the scalar valued tensor function f be defined as:

$$f : \boldsymbol{A} \rightarrow f(\boldsymbol{A}) \tag{4.19}$$

with the 2nd order tensor $\boldsymbol{A} = A_{ij} \, \boldsymbol{e}_i \otimes \boldsymbol{e}_j$. The derivation leads to a 2nd order tensor defined as:

$$\left[\frac{\partial f(\boldsymbol{A})}{\partial \boldsymbol{A}} \right]_{ij} = \frac{\partial f(\boldsymbol{A})}{\partial A_{ij}} \tag{4.20}$$

If f can be written as the product of two scalar valued tensor functions g and h:

$$f(\boldsymbol{A}) = g(\boldsymbol{A}) h(\boldsymbol{A}) \tag{4.21}$$

the product rule of derivation applies as follows:

$$\frac{\partial f(\boldsymbol{A})}{\partial \boldsymbol{A}} = \frac{\partial g(\boldsymbol{A})h(\boldsymbol{A})}{\partial \boldsymbol{A}} = \frac{\partial g(\boldsymbol{A})}{\partial \boldsymbol{A}} h(\boldsymbol{A}) + g(\boldsymbol{A}) \frac{\partial h(\boldsymbol{A})}{\partial \boldsymbol{A}}$$

$$\left[\frac{\partial f(\boldsymbol{A})}{\partial \boldsymbol{A}} \right]_{ij} = \left[\frac{\partial g(\boldsymbol{A})h(\boldsymbol{A})}{\partial \boldsymbol{A}} \right]_{ij} = \frac{\partial g(\boldsymbol{A})}{\partial A_{ij}} h(\boldsymbol{A}) + g(\boldsymbol{A}) \frac{\partial h(\boldsymbol{A})}{\partial A_{ij}}$$

(4.22)

Tensor valued tensor function

Let the 2nd order tensor valued tensor function $\boldsymbol{F}$ be defined as:

$$\boldsymbol{F} : \boldsymbol{A} \rightarrow \boldsymbol{F}(\boldsymbol{A}) \tag{4.23}$$

with the 2nd order tensor $\boldsymbol{A} = A_{ij}\, \boldsymbol{e}_i \otimes \boldsymbol{e}_j$. The derivation leads to a 4th order tensor defined as:

$$\left[\frac{\partial \boldsymbol{F}(\boldsymbol{A})}{\partial \boldsymbol{A}} \right]_{ijkl} = \frac{\partial \boldsymbol{F}(\boldsymbol{A})_{ij}}{\partial A_{kl}} \tag{4.24}$$

If $\boldsymbol{F}$ can be written as the product of two 2nd order tensor valued tensor functions $\boldsymbol{G}$ and $\boldsymbol{H}$:

$$\boldsymbol{F}(\boldsymbol{A}) = \boldsymbol{G}(\boldsymbol{A})\boldsymbol{H}(\boldsymbol{A})$$

$$F_{ij}(\boldsymbol{A}) = G_{im}(\boldsymbol{A})H_{mj}(\boldsymbol{A})$$

(4.25)

then the product rule of derivation applies as follows:

$$\frac{\partial \boldsymbol{F}(\boldsymbol{A})}{\partial \boldsymbol{A}} = \frac{\partial \boldsymbol{G}(\boldsymbol{A})\boldsymbol{H}(\boldsymbol{A})}{\partial \boldsymbol{A}} = \frac{\partial \boldsymbol{G}(\boldsymbol{A})}{\partial \boldsymbol{A}} \cdot \boldsymbol{H}(\boldsymbol{A}) + \boldsymbol{G}(\boldsymbol{A}) \cdot \frac{\partial \boldsymbol{G}(\boldsymbol{A})}{\partial \boldsymbol{A}}$$

$$\left[\frac{\partial \boldsymbol{F}(\boldsymbol{A})}{\partial \boldsymbol{A}} \right]_{ijkl} = \left[\frac{\partial \boldsymbol{G}(\boldsymbol{A})\boldsymbol{H}(\boldsymbol{A})}{\partial \boldsymbol{A}} \right]_{ijkl}$$

$$= \left[\frac{\partial \boldsymbol{G}(\boldsymbol{A})}{\partial \boldsymbol{A}} \right]_{imkl} H_{mj}(\boldsymbol{A}) + G_{im}(\boldsymbol{A}) \left[\frac{\partial \boldsymbol{H}(\boldsymbol{A})}{\partial \boldsymbol{A}} \right]_{mjkl}$$

$$= \frac{\partial G_{im}(\boldsymbol{A})}{\partial A_{kl}} H_{mj}(\boldsymbol{A}) + G_{im}(\boldsymbol{A}) \frac{\partial H_{mj}(\boldsymbol{A})}{\partial A_{kl}}$$

(4.26)

If the 2nd order tensor valued tensor function $\boldsymbol{F}$ can be written as a product of a scalar valued tensor function g and a 2nd order tensor valued tensor function $\boldsymbol{H}$:

$$\boldsymbol{F}(\boldsymbol{A}) = g(\boldsymbol{A})\boldsymbol{H}(\boldsymbol{A}) \tag{4.27}$$

then the product rule of derivation applies as follows:

$$\frac{\partial \boldsymbol{F}(\boldsymbol{A})}{\partial \boldsymbol{A}} = \frac{\partial g(\boldsymbol{A})\boldsymbol{H}(\boldsymbol{A})}{\partial \boldsymbol{A}} = \boldsymbol{H}(\boldsymbol{A}) \otimes \frac{\partial g(\boldsymbol{A})}{\partial \boldsymbol{A}} + g(\boldsymbol{A})\frac{\partial \boldsymbol{H}(\boldsymbol{A})}{\partial \boldsymbol{A}}$$

$$\begin{aligned}
\left[\frac{\partial \boldsymbol{F}(\boldsymbol{A})}{\partial \boldsymbol{A}}\right]_{ijkl} &= \left[\frac{\partial g(\boldsymbol{A})\boldsymbol{H}(\boldsymbol{A})}{\partial \boldsymbol{A}}\right]_{ijkl} \\
&= \left[\frac{\partial g(\boldsymbol{A})}{\partial \boldsymbol{A}}\right]_{kl} H_{ij}(\boldsymbol{A}) + g(\boldsymbol{A})\left[\frac{\partial \boldsymbol{H}(\boldsymbol{A})}{\partial \boldsymbol{A}}\right]_{ijkl} \\
&= \frac{\partial g(\boldsymbol{A})}{\partial A_{kl}} H_{ij}(\boldsymbol{A}) + g(\boldsymbol{A})\frac{\partial H_{ij}(\boldsymbol{A})}{\partial A_{kl}}
\end{aligned} \tag{4.28}$$

4.A.3 Corotational Derivatives of Stress Tensors

The basic framework and definitions used in this work can be reread p.e. in Holzapfel [2000].

The linearised material behaviour in Lagrange description reads as follow:

$$\boldsymbol{\sigma}_{2\text{PK}} = \mathbb{C} : \mathbf{E} \tag{4.29}$$

with the 2nd Piola-Kirchhoff stress $\boldsymbol{\sigma}_{2\text{PK}}$, tangent modulus $\mathbb{C}$ and Green strain tensor $\mathbf{E}$.

Replacing the 2nd Piola-Kirchhoff by Cauchy stress leads to:

$$J\mathbf{F}^{-1} \cdot \boldsymbol{\sigma} \cdot \mathbf{F}^{-T} = \mathbb{C} : \mathbf{E} \tag{4.30}$$

with the deformation gradient $\mathbf{F}$. Solving to Cauchy stress

$$\boldsymbol{\sigma} = \frac{1}{J}\mathbf{F} \cdot (\mathbb{C} : \mathbf{E}) \cdot \mathbf{F}^{T} \tag{4.31}$$

and taking the time derivative gives:

$$\dot{\boldsymbol{\sigma}} = -\left(\frac{\dot{J}}{J^2}\right) \mathbf{F} \cdot (\mathbb{C} : \mathbf{E}) \cdot \mathbf{F}^T + \frac{1}{J} \dot{\mathbf{F}} \cdot (\mathbb{C} : \mathbf{E}) \cdot \mathbf{F}^T + \frac{1}{J} \mathbf{F} \cdot (\mathbb{C} : \dot{\mathbf{E}}) \cdot \mathbf{F}^T + \frac{1}{J} \mathbf{F} \cdot (\mathbb{C} : \mathbf{E}) \cdot \dot{\mathbf{F}}^T \qquad (4.32)$$

The following terms can be substituted with:

$$\text{tr}(\mathbf{D}) = \frac{\dot{J}}{J} \qquad \dot{\mathbf{F}} = \mathbf{L} \cdot \mathbf{F} \qquad \dot{\mathbf{F}}^T = \mathbf{F}^T \cdot \mathbf{L}^T \qquad \dot{\mathbf{E}} = \mathbf{F}^T \cdot \mathbf{D} \cdot \mathbf{F} \qquad (4.33)$$

by using the velocity gradient $\mathbf{L}$. This leads to:

$$\begin{aligned}
\dot{\boldsymbol{\sigma}} = &- \text{tr}(\mathbf{D}) \frac{1}{J} \mathbf{F} \cdot (\mathbb{C} : \mathbf{E}) \cdot \mathbf{F}^T + \frac{1}{J} \mathbf{L} \cdot \mathbf{F} \cdot (\mathbb{C} : \mathbf{E}) \cdot \mathbf{F}^T + \\
&\frac{1}{J} \mathbf{F} \cdot \left(\mathbb{C} : (\mathbf{F}^T \cdot \mathbf{D} \cdot \mathbf{F}) \right) \cdot \mathbf{F}^T + \frac{1}{J} \mathbf{F} \cdot (\mathbb{C} : \mathbf{E}) \cdot \mathbf{F}^T \cdot \mathbf{L}^T
\end{aligned} \qquad (4.34)$$

As $\frac{1}{J} \mathbf{F} \cdot (\mathbb{C} : \mathbf{E}) \cdot \mathbf{F}^T = \boldsymbol{\sigma}$, the equation can be written this way:

$$\dot{\boldsymbol{\sigma}} = -\text{tr}(\mathbf{D})\, \boldsymbol{\sigma} + \mathbf{L} \cdot \boldsymbol{\sigma} + \boldsymbol{\sigma} \cdot \mathbf{L}^T + \frac{1}{J} \mathbf{F} \cdot \left(\mathbb{C} : (\mathbf{F}^T \cdot \mathbf{D} \cdot \mathbf{F}) \right) \cdot \mathbf{F}^T \qquad (4.35)$$

Rearranging the terms leads finally to:

$$\dot{\boldsymbol{\sigma}} - \mathbf{L} \cdot \boldsymbol{\sigma} - \boldsymbol{\sigma} \cdot \mathbf{L}^T = -\text{tr}(\mathbf{D})\, \boldsymbol{\sigma} + \frac{1}{J} (\mathbf{F} \cdot \mathbf{F} \cdot \mathbb{C} \cdot \mathbf{F}^T \cdot \mathbf{F}^T) : \mathbf{D} \qquad (4.36)$$

The term $\text{tr}(\mathbf{D})$ is negligibly small, for incompressible materials it is zero.

The terms involving $\mathbb{C}$ represent rigid body rotations of the stiffness tensor. The terms $\frac{1}{J} (\mathbf{F} \cdot \mathbf{F} \cdot \mathbb{C} \cdot \mathbf{F}^T \cdot \mathbf{F}^T)$ are replaced by $\mathbb{c}$.

The left hand side in equation 4.36 is the Lie Derivative represented by $\overset{\nabla}{\boldsymbol{\sigma}}$. The equation reduces to:

$$\overset{\nabla}{\boldsymbol{\sigma}} = \mathbb{c} : \mathbf{D} \tag{4.37}$$

Let the object rotate without deformation $\mathbf{D} = 0$:

$$\overset{\nabla}{\boldsymbol{\sigma}} = \dot{\boldsymbol{\sigma}} - \mathbf{L} \cdot \boldsymbol{\sigma} - \boldsymbol{\sigma} \cdot \mathbf{L}^T = 0 \tag{4.38}$$

It can be seen that the terms containing the velocity gradient $\mathbf{L}$ are needed to compensate $\dot{\boldsymbol{\sigma}} \neq 0$. With $\mathbf{D} = 0$, $\mathbf{L}$ reduces to $\mathbf{W}$ because of $\mathbf{L} = \mathbf{D} + \mathbf{W}$. Replacing leads to:

$$\overset{\nabla}{\boldsymbol{\sigma}} = \dot{\boldsymbol{\sigma}} - \mathbf{W} \cdot \boldsymbol{\sigma} - \boldsymbol{\sigma} \cdot \mathbf{W}^T = 0 \tag{4.39}$$

With $\mathbf{W}^T = -\mathbf{W}$ ($\mathbf{W}$ is antisymmetric) one can obtain the Jaumann derivative $\overset{o}{\boldsymbol{\sigma}}$:

$$\overset{o}{\boldsymbol{\sigma}} = \dot{\boldsymbol{\sigma}} - \mathbf{W} \cdot \boldsymbol{\sigma} + \boldsymbol{\sigma} \cdot \mathbf{W} = 0 \tag{4.40}$$

The derivation of $\boldsymbol{\sigma}$ can thus be written as:

$$\dot{\boldsymbol{\sigma}} = \mathbb{c} : \mathbf{D} + \mathbf{W} \cdot \boldsymbol{\sigma} - \boldsymbol{\sigma} \cdot \mathbf{W} \tag{4.41}$$

4.A.4   Incremental Form of Jaumann Stress Rate

Starting from the definition of the Jaumann stress rate:

$$\dot{\boldsymbol{\sigma}} = \mathbb{c} : \mathbf{D} + \mathbf{W} \cdot \boldsymbol{\sigma} - \boldsymbol{\sigma} \cdot \mathbf{W} \tag{4.42}$$

with the time derivative of the Cauchy stress $\boldsymbol{\sigma}$, the determinant of the deformation gradient J, the fourth order elasticity tensor $\mathbb{C}$, the rate of deformation tensor $\mathbf{D}$, the spin tensor $\mathbf{W}$ and the Cauchy stress $\boldsymbol{\sigma}$. With the following definitions:

$$\mathbf{D} = sym(\dot{\mathbf{F}}\mathbf{F}^{-1}) = \frac{1}{2}(\dot{\mathbf{F}}\mathbf{F}^{-1} + \mathbf{F}^{-T}\dot{\mathbf{F}}^{T}) \qquad \mathbf{W} = asym(\dot{\mathbf{F}}\mathbf{F}^{-1}) = \frac{1}{2}(\dot{\mathbf{F}}\mathbf{F}^{-1} - \mathbf{F}^{-T}\dot{\mathbf{F}}^{T}) \qquad (4.43)$$

inserted into equations 4.43 leads to:

$$\dot{\boldsymbol{\sigma}} = \mathbb{C} : \frac{1}{2}(\dot{\mathbf{F}}\mathbf{F}^{-1} + \mathbf{F}^{-T}\dot{\mathbf{F}}^{T}) + \frac{1}{2}(\dot{\mathbf{F}}\mathbf{F}^{-1} - \mathbf{F}^{-T}\dot{\mathbf{F}}^{T})\boldsymbol{\sigma} - \boldsymbol{\sigma}\frac{1}{2}(\dot{\mathbf{F}}\mathbf{F}^{-1} - \mathbf{F}^{-T}\dot{\mathbf{F}}^{T}) \qquad (4.44)$$

Replacing all time derivatives by incremental changes leads to the incremental form:

$$\delta\boldsymbol{\sigma} = \mathbb{C} : \frac{1}{2}(\delta\mathbf{F}\mathbf{F}^{-1} + \mathbf{F}^{-T}\delta\mathbf{F}^{T}) + \frac{1}{2}(\delta\mathbf{F}\mathbf{F}^{-1} - \mathbf{F}^{-T}\delta\mathbf{F}^{T})\boldsymbol{\sigma} - \boldsymbol{\sigma}\frac{1}{2}(\delta\mathbf{F}\mathbf{F}^{-1} - \mathbf{F}^{-T}\delta\mathbf{F}^{T}) \qquad (4.45)$$

With the definitions of the rate of deformation tensor and the spin tensor in equation 4.43, the following formula is achieved:

$$\delta\boldsymbol{\sigma} = \mathbb{C} : \delta\mathbf{D} + \delta\mathbf{W}\boldsymbol{\sigma} - \boldsymbol{\sigma}\delta\mathbf{W} \qquad (4.46)$$

4.A.5   Numerical Approximation of Elasticity Tensors

The numerical approximation of elasticity tensors is based on a perturbation scheme of the deformation gradient based on a forward differentiation approximation [Miehe 1996]. When applying a perturbation of the following form:

$$\delta\mathbf{F} = \frac{\epsilon}{2}(e_i \otimes e_j \mathbf{F} + e_j \otimes e_i \mathbf{F}) \qquad (4.47)$$

with a perturbation parameter ϵ, the incremental rate of deformation tensor and the spin tensor becomes the following:

$$
\begin{aligned}
\delta\mathbf{D} &= \frac{1}{2}\left(\frac{\epsilon}{2}\left(e_i \otimes e_j\mathbf{F} + e_j \otimes e_i\mathbf{F}\right)\mathbf{F}^{-1} + \mathbf{F}^{-T}\frac{\epsilon}{2}\left(e_i \otimes e_j\mathbf{F} + e_j \otimes e_i\mathbf{F}\right)^T\right) \\
&= \frac{\epsilon}{4}\left(\left(e_i \otimes e_j + e_j \otimes e_i\right)\mathbf{F}\mathbf{F}^{-1} + \left((e_i \otimes e_j + e_j \otimes e_i)\mathbf{F}\mathbf{F}^{-1}\right)^T\right) \\
&= \frac{\epsilon}{4}\left(\left(e_i \otimes e_j + e_j \otimes e_i\right) + \left(e_i \otimes e_j + e_j \otimes e_i\right)^T\right) \\
&= \frac{\epsilon}{2}(e_i \otimes e_j + e_j \otimes e_i) \\
\delta\mathbf{W} &= \frac{1}{2}\left(\frac{\epsilon}{2}\left(e_i \otimes e_j\mathbf{F} + e_j \otimes e_i\mathbf{F}\right)\mathbf{F}^{-1} - \mathbf{F}^{-T}\frac{\epsilon}{2}\left(e_i \otimes e_j\mathbf{F} + e_j \otimes e_i\mathbf{F}\right)^T\right) \\
&= \frac{\epsilon}{4}\left(\left(e_i \otimes e_j + e_j \otimes e_i\right)\mathbf{F}\mathbf{F}^{-1} - \left((e_i \otimes e_j + e_j \otimes e_i)\mathbf{F}\mathbf{F}^{-1}\right)^T\right) \\
&= \frac{\epsilon}{4}\left(\left(e_i \otimes e_j + e_j \otimes e_i\right) - \left(e_i \otimes e_j + e_j \otimes e_i\right)^T\right) \\
&= 0
\end{aligned}
\tag{4.48}
$$

The incremental change in stress can then be approximated by the forward difference:

$$
\delta\boldsymbol{\sigma} = \boldsymbol{\sigma}(\mathbf{F} + \delta\mathbf{F}) - \boldsymbol{\sigma}(\mathbf{F})
\tag{4.49}
$$

The elasticity tensor can then be approximated with the formula:

$$
\mathbb{C}_{ijkl} = \frac{\boldsymbol{\sigma}(\mathbf{F} + \delta\mathbf{F})_{ij} - \boldsymbol{\sigma}(\mathbf{F})_{ij}}{\delta\mathbf{D}_{kl}}
\tag{4.50}
$$

4.B   Bibliography

Agency for Healthcare Research and Quality.: Comparative effectiveness of nonoperative and operative treatments for rotator cuff tears. *AHRQ Comparative Effectiveness Review*, (22), 2010.

American Academy of Orthopaedic Surgeons, August 2014. URL http://orthoinfo.aaos.org/ topic.cfm?topic=a00064. "Most tears occur in the supraspinatus muscle and tendon, . . . If you fall down on your outstretched arm or lift something too heavy with a jerking motion, you can tear your rotator cuff.".

Ball J.: Convexity conditions and existence theorems in nonlinear elasticity. *Arch Rational Mech Anal*, 63(4):337–403, 1976.

Balzani D., Neff P., Schröder J., and Holzapfel G. A.: A polyconvex framework for soft biological tissues. adjustment to experimental data. *International Journal of Solids and Structures*, 43 (20):6052 – 6070, 2006.

Ben-Yishay A., Zuckerman J., Gallagher M., and Cuomo F.: Pain inhibition of shoulder strength in patients with impingement syndrome. *Orthopedics*, 17(8):685–688, 1994.

Benjamin M., Toumi H., Ralphs J. R., Bydder G., Best T. M., and Milz S.: Where tendons and ligaments meet bone: attachment sites ('entheses') in relation to exercise and/or mechanical load. *J Anat*, 208(4):471–490, 2006.

Clark J. and Stechschulte D. J.: The interface between bone and tendon at an insertion site: a study of the quadriceps tendon insertion. *J Anat*, 192(4):605–616, 1998.

Coley B., Jolles B. M., Farron A., and Aminian K.: Arm position during daily activity. *Gait Posture*, 28(4):581–587, 2008.

Curtis A. S., Burbank K. M., Tierney J. J., Scheller A. D., and Curran A. R.: The insertional footprint of the rotator cuff: An anatomic study. *Arthroscopy*, 22(6):603–609.e1, 2006.

De Vita R. and Slaughter W.: A constitutive law for the failure behavior of medial collateral ligaments. *Biomech Model Mechanobiol*, 6(3):189–197, 2007.

Ehret A. E. and Itskov M.: A polyconvex hyperelastic model for fiber-reinforced materials in application to soft tissues. *J Mater Sci*, 42(21):8853–8863, 2007.

Ehret A. E., Böl M., and Itskov M.: A continuum constitutive model for the active behaviour of skeletal muscle. *J Mech Phys Solids*, 59(3):625–636, 2011.

Engelhardt C., Farron A., Becce F., Pioletti D., and Terrier A.: Impact of partial-thickness tears on supraspinatus tendon strain based on a finite element analysis. *Computer Methods in Biomechanics and Biomedical Engineering*, 17(SUPP1):118–119, 2014.

Engelhardt C., Ingram D., Müllhaupt P., Farron A., Becce F., Pioletti D., and Terrier A.: Effect of partial-thickness tear on loading capacities of the supraspinatus tendon: a finite element analysis. *Comp Methods Biomech Biomed Engin*, 2015. PMID: 26290956.

Favre P., Senteler M., Hipp J., Scherrer S., Gerber C., and Snedeker J. G.: An integrated model of active glenohumeral stability. *J Biomech*, 45(13):2248–2255, 2012.

Fukuda H., Hamada K., Nakajima T., Yamada N., Tomonaga A., and Goto M.: Partial-thickness tears of the rotator cuff. a clinicopathological review based on 66 surgically verified cases. *Int Orthop*, 20(4):257–265, 1996.

Fung Y. C.: Biorheology of soft tissues. *Bioreheology*, 10:139–155, 1973.

Garner B. A. and Pandy M. G.: Musculoskeletal model of the upper limb based on the visible human male dataset. *Comput Methods Biomech Biomed Engin*, 4:93–126, 2000.

Guo Z. and Vita R. D.: Probabilistic constitutive law for damage in ligaments. *Med Eng Phys*, 31(9):1104 – 1109, 2009.

Herring S. A. and Nilson K. L.: Introduction to overuse injuries. *Clin Sports Med*, 6(2):225–239, 1987.

Holzapfel G. A.: *Nonlinear Solid Mechanics*. Wiley, Chichester, England, 2000.

Holzapfel G. A. and Gasser T. C.: A viscoelastic model for fiber-reinforced composites at finite strains: Continuum basis, computational aspects and applications. *Computer Methods in Applied Mechanics and Engineering*, 190(34):4379–4403, 2001.

Holzapfel G., Gasser T., and Ogden R.: A new constitutive framework for arterial wall mechanics and a comparative study of material models. *Journal of elasticity and the physical science of solids*, 61(1-3):1–48, 2000.

Huang C.-Y., Wang V. M., Pawluk R. J., Bucchieri J. S., Levine W. N., Bigliani L. U., Mow V. C., and Flatow E. L.: Inhomogeneous mechanical behavior of the human supraspinatus tendon under uniaxial loading. *J Orthop Res*, 23(4):924 – 930, 2005.

Ingram D., Müllhaupt P., Terrier A., Pralong E., and Farron A.: Dynamical biomechanical model of the shoulder for muscle-force estimation. *Proceedings of the IEEE RAS-EMBS International Conference on Biomedical Robotics and Biomechatronics*, pages 407–412, 2012.

Ingram D., Engelhardt C., Farron A., Terrier A., and Muellhaupt P. A Minimal Set of Coordinates for Describing Humanoid Shoulder Motion. In *2013 Ieee/Rsj International Conference On Intelligent Robots And Systems (Iros)*, IEEE International Conference on Intelligent Robots and Systems, pages 5537–5544. Ieee, 2013.

Ingram D., Engelhardt C., Farron A., Terrier A., and Müllhaupt P.: Design of a humanoid shoulder mechanism without a gliding shoulder blade architecture. *IEEE Transactions on Robotics*, 2014.

Kannus P. and Jozsa L. G.: *Human Tendons: Anatomy, Physiology and Pathology*. Human Kinetics Publishers, 1997.

Kim H. M., Teefey S. A., Zelig A., Galatz L. M., Keener J. D., and Yamaguchi K.: Shoulder strength in asymptomatic individuals with intact compared with torn rotator cuffs. *J Bone Joint Surg*, 91:289–296, 2009.

Kim S. Y., Boynton E. L., Ravichandiran K., Fung L. Y., Bleakney R., and Agur A. M.: Three-dimensional study of the musculotendinous architecture of supraspinatus and its functional correlations. *Clin Anat*, 20(6):648–655, 2007.

Kim Y.-S., Kim J.-M., Bigliani L. U., Kim H.-J., and Jung H.-W.: In vivo strain analysis of the intact supraspinatus tendon by ultrasound speckles tracking imaging. *Journal of Orthopaedic Research*, 29(12):1931–1937, 2011.

Kirschenbaum D., Coyle Jr. M., Leddy J., Katsaros P., Tan Jr. F., and Cody R.: Shoulder strength with rotator cuff tears: Pre- and postoperative analysis. *Clinical Orthopaedics and Related Research*, (288):174–178, 1993.

Lake S. P., Miller K. S., Elliott D. M., and Soslowsky L. J.: Effect of fiber distribution and realignment on the nonlinear and inhomogeneous mechanical properties of human supraspinatus tendon under longitudinal tensile loading. *J Orthop Res*, 27(12):1596–1602, 2009.

Lake S. P., Miller K. S., Elliott D. M., and Soslowsky L. J.: Tensile properties and fiber alignment of human supraspinatus tendon in the transverse direction demonstrate inhomogeneity, nonlinearity, and regional isotropy. *J Biomech*, 43(4):727–732, 2010.

Liao H. and Belkoff S. M.: A failure model for ligaments. *J Biomech*, 32(2):183–188, 1999.

Matsuhashi T., Hooke A. W., Zhao K. D., Goto A., Sperling J. W., Steinmann S. P., and An K.-N.: Tensile properties of a morphologically split supraspinatus tendon. *Clin Anat*, pages n/a–n/a, 2013.

McCabe R. A., Nicholas S. J., Montgomery K. D., Finneran J. J., and McHugh M. P.: The effect of rotator cuff tear size on shoulder strength and range of motion. *J Orthop Sports Phys Ther*, 35(3):130–135, 2005.

Michener L., McClure P., and Karduna A.: Anatomical and biomechanical mechanisms of subacromial impingement syndrome. *Clinical Biomechanics*, 18(5):369–379, 2003.

Miehe C.: Numerical computation of algorithmic (consistent) tangent moduli in large-strain computational inelasticity. *Comput Method Appl M*, 134(3-4):223–240, 1996.

Miller R., Fujimaki Y., Araki D., Musahl V., and Debski R.: Strain distribution due to propagation of tears in the anterior supraspinatus tendon. *Journal of Orthopaedic Research*, 32(10): 1283–1289, 2014.

Oh J., Yoon J., Kim J., and Oh C.: Isokinetic muscle performance test can predict the status of rotator cuff muscle. *Clinical Orthopaedics and Related Research*, 468(6):1506–1513, 2010.

Peña E., Martinez M. A., Calvo B., and Doblaré M.: On the numerical treatment of initial strains in biological soft tissues. *International Journal for Numerical Methods in Engineering*, 68(8):836–860, 2006.

Pioletti D. P., Rakotomanana L. R., Benvenuti J. F., and Leyvraz P. F.: Viscoelastic constitutive law in large deformations: application to human knee ligaments and tendons. *J Biomech*, 31 (8):753–7, 1998.

Renström P. and Hach T.: *Insertional tendinopathy in sports*. 2005.

Rho J. Y., Ashman R. B., and Turner C. H.: Young's modulus of trabecular and cortical bone material: Ultrasonic and microtensile measurements. *J Biomech*, 26(2):111 – 119, 1993.

Saltelli A., Ratto M., Andres T., Campolongo F., Cariboni J., Gatelli D., Saisana M., and Tarantola S.: *Global sensitivity analysis: the primer*. John Wiley & Sons, 2008.

Saltelli A., Annoni P., Azzini I., Campolongo F., Ratto M., and Tarantola S.: Variance based sensitivity analysis of model output. design and estimator for the total sensitivity index. *Comput Phys Comm*, 181(2):259–270, 2010.

Seida J. C., LeBlanc C., Schouten J. R., Mousavi S. S., Hartling L., Vandermeer B., Tjosvold L., and Sheps D. M.: Systematic review: Nonoperative and operative treatments for rotator cuff tears. *Ann Intern Med*, 153(4):246–255, 2010.

Tashjian R. Z.: Epidemiology, natural history, and indications for treatment of rotator cuff tears. *Clin Sports Med*, 31(4):589–604, 2012.

Taylor D. Chapter 2 - the theory of critical distances: Basics: An introduction to the basic methodology of the {TCD}. In Taylor D., editor, *The Theory of Critical Distances*, pages 21–31. Elsevier Science Ltd, Oxford, 2007. ISBN 978-0-08-044478-9.

Tempelhof S., Rupp S., and Seil R.: Age-related prevalence of rotator cuff tears in asymptomatic shoulders. *J Shoulder Elbow Surg*, 8(4):296 – 299, 1999.

Terrier A., Aeberhard M., Michellod Y., Müllhaupt P., Gillet D., Farron A., and Pioletti D.: A musculoskeletal shoulder model based on pseudo-inverse and nullspace optimization. *Med Eng Physics*, 32:1050–1056, 2010.

van der Helm F. C. T.: A finite element musculoskeletal model of the shoulder mechanism. *J Biomech*, 27(5):551–569, 1994.

Weiss J. A., Gardiner J. C., Ellis B. J., Lujan T. J., and Phatak N. S.: Three-dimensional finite element modeling of ligaments: Technical aspects. *Med Engin Phys*, 27(10):845–861, 2005.

Williams G. R., Rockwood C. A., Bigliani L. U., Iannotti J. P., and Stanwood W.: Rotator cuff tears: Why do we repair them? *J Bone Joint Surg Am*, 86(12):2764–2776, 2004.

Wu G., van der Helmb F. C. T., Veeger H. E. J., Makhsouse M., Royf P. V., Angling C., Nagelsh J., Kardunai A. R., McQuadej K., Wangk X., Wernerl F. W., and Buchholzm B.: ISB recommendation on definitions of joint coordinate systems of various joints for the reporting of human joint motion - Part II: shoulder, elbow, wrist and hand. *J Biomech*, 38:981–992, 2005.

Yanagawa T., Goodwin C. J., Shelburne K. B., Giphart J. E., Torry M. R., and Pandy M. G.: Contributions of the individual muscles of the shoulder to glenohumeral joint stability during abduction. *J Biomech Eng*, 130(2), 2008.

5 Effect of Anatomic Parameters on Shoulder Biomechanics

This chapter will be submitted for publication to the Journal of Shoulder and Elbow Surgery under the title "Effect of Acromion Length and Glenoid Inclination on Glenohumeral Osteoarthritis and Supraspinatus Tears: A Biomechanical Analysis".

5.1 Introduction

Shoulder disorders are widely spread debilitating diseases, that can quickly lead to significant restrictions in daily life [Hasvold and Johnsen 1993, Pope et al. 1997]. Osteoarthritis and rotator cuff tears are the two most common pathologies [Mitchell et al. 2005]. Statistically spoken, age is the primary risk factor for both diseases [Buckwalter and Martin 2006, Nho et al. 2008]. Recent research assumes a long term multi causal process of degeneration in the affected soft tissues [Buckwalter and Martin 2006, Renström and Hach 2005]. Besides metabolic and inflammatory contributions, it is well accepted that purely biomechanical factors play a significant role to maintain the homeostasis of the shoulder joint [Brandt et al. 2009, Egloff et al. 2012]. Until recently, mechanical contributions were mainly related to lifestyle dependent activity level, i.e. a higher risk for overhead athletes and physical hard working people could be shown [Buckwalter and Martin 2006]. However, greater attention is paid nowadays to the biomechanical effect of anatomical parameters of the shoulder joint degeneration pathologies.

The preliminary studies investigating the association between anatomical parameters and degenerative pathologies of the shoulder focused on the glenoid orientation [Hughes et al. 2003, Tétreault et al. 2004, Wong et al. 2003]. An upward inclination of the glenoid was correlated with increased occurrence of supraspinatus tears. In the same way, retroversion of the glenoid was associated with tears of anterior rotator cuff muscles, while anteversion was associated with tears of posterior cuff muscles respectively.

In 2006, Nyffeler et al. hypothesized that a long acromion would favour the middle deltoid to pull the humeral head upwards, which increases the risk of impingement and induces

more rotator cuff activity to counteract and stabilize the glenohumeral joint [Nyffeler et al. 2006]. This study introduced the acromion index, which measured the lateral extension of the acromion. A large acromion index could be linked with tears of the supraspinatus tendon. However, a low acromion index could not be correlated to osteoarthritis, although, when applying the same mechanical principles as previously, a short acromion would favor the deltoid to increase the compressive stresses on the glenoid cavity.

Later, Moor et al. developed another anatomic parameter called the critical shoulder angle [Moor et al. 2013]. The parameter measures the angle between two lines starting from the inferior edge of the glenoid to the superior edge of the glenoid, respectively to the lateral edge of the acromion. The authors claimed the critical shoulder angle was a better parameter to link anatomy with osteoarthritis and rotator cuff tears as the parameter takes into account the glenoid inclination. Indeed, the study could identify critical shoulder angles for healthy subjects (33 degrees), subjects suffering from osteoarthritis (28 degrees) and rotator cuff tears (38 degrees).

However, these radiologic studies had only observatory character. The statistical link between the anatomic parameters and shoulder disease was found through analysis of medical image databases.

Therefore, the goal of this work was to evaluate biomechanically the effect of these two anatomical parameters on cartilage and supraspinatus tendon strain. We extended an existing numerical musculoskeletal shoulder model based on a healthy volunteer, to vary the acromion index and glenoid inclination of the model. The numerical predictions of strain were related to clinical observation through the critical shoulder angle. By extension, we estimated the relative importance of these two anatomical parameters on the reported occurrence of glenohumeral osteoarthritis and supraspinatus tendon tears.

5.2 Materials and Methods

We used a biomechanical model of the shoulder divided into three levels (Figure 5.1). At the first level, a musculoskeletal model of the shoulder estimated the muscle and joint forces [Brandt et al. 2009, Ehret et al. 2011, Terrier et al. 2010]. At the second level, we developed a model of the glenohumeral joint, to evaluate cartilage strain and humeral head translations, from the force predictions of the musculoskeletal model. At the third level, we used a model of the supraspinatus tendon to predict subacromial space and strain, using the muscle force and humeral translation obtained by the previous two models [Engelhardt et al. 2015a].

5.2.1 Musculoskeletal Model

The musculoskeletal shoulder model included the thorax, clavicle, scapula, humerus, radius and ulna [Engelhardt et al. 2015b, Ingram et al. 2015a;b]. The model was built from MRI scans

of a 27 years old male volunteer showing no sign of shoulder pathology. We developed a custom MRI protocol consisting of two three-dimensional T1-weighted sequences on a 3 Tesla MRI scanner. The first sequence, covering the glenohumeral joint, was a gradient-recalled echo VIBE (TR/TE, 12.2/4.8 ms) with an isotropic resolution of 0.6 mm. The second sequence, covering the whole right hemi thorax, was a turbo spin-echo SPACE (TR/TE, 600/9.1ms) with an isotropic spatial resolution of 0.9 mm. We co-registered the two sequences with Amira (FEI Visualization Sciences Group, France). The bony structures were reconstructed out of the MRI data. The segmentation was performed with Amira. We then used Geomagic (3D Systems, USA) to transform the segmentation into surfaces. These 3D reconstructions were superposed to the MRI images for visual verification.

Bones were rigid. The sternoclavicular, acromioclavicular and glenohumeral joints were spherical joints. The elbow joint was modelled as a hinge joint with one degree of freedom. The scapula was constraint to glide on an ellipsoid representing the thoracic cage [Garner
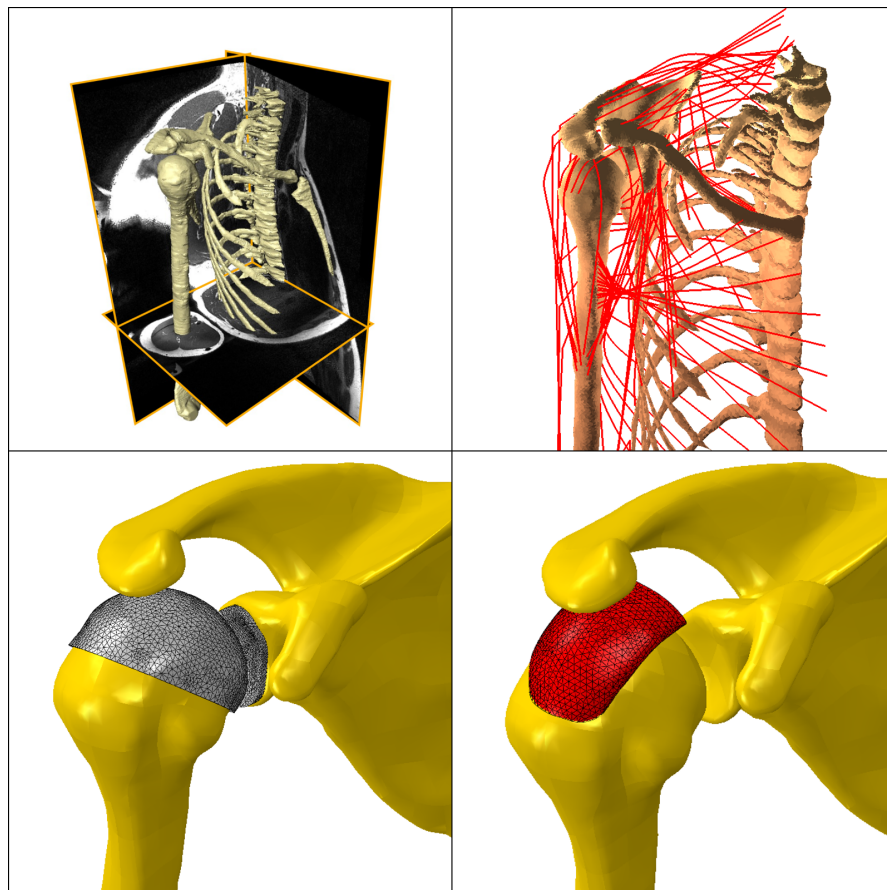

Figure 5.1 – Reconstruction of thorax, clavicle, scapula and humerus out of in vivo MRI images (top left). The musculoskeletal shoulder model with 24 muscles (top right). The glenohumeral model with cartilage and glenohumeral force in red (bottom left). The tendon model with the supraspinatus tendon and supraspinatus muscle force in red (bottom right).

and Pandy 1997; 2000b]. The model contained 24 muscle divided into 42 segments, and each segment was represented by three cables. Origin and insertion sites were interpolated from MRI images with cubic Catmull-Rom splines, on which the start and end points of the muscle cables were evenly distributed. The muscle cables wrapped around cylinders to reproduce the centroid lines of the muscles following the obstacle set approach [Garner and Pandy 2000a]. The final muscle path was visually verified by superposing the muscle path to the MRI images. The undetermined problem of muscle force coordination was solved using an inverse dynamics approach followed by a null-space optimization [Engelhardt et al. 2015b, Ingram et al. 2015a;b, Terrier et al. 2010]. The sum of squared muscle stresses was used as optimization criterion. A glenohumeral joint stability criterion was included to avoid subluxation. The musculoskeletal model was implemented in Matlab (The MathWorks, USA). We simulated an abduction movement in the scapula plane from a rest position up to 120 degrees. The model predicted the muscle forces and the glenohumeral joint reaction force.

5.2.2   Cartilage Model

The cartilage model included the cartilage of the humerus and scapula, and the scapula and humerus bones. The geometry of the cartilage was reconstructed from the same MRI images. The cortical bone thickness was estimated from ten CT scans of healthy subjects provided by the radiology department of the University Hospital Lausanne (CHUV). It was two mm for the humeral head, and three mm for the glenoid side. The cartilage was modelled by an incompressible exponential hyperelastic constitutive law [Pioletti and Rakotomanana 2000]. The subchondral bone was linear elastic, with specific elastic constants for cortical and trabecular bone (Table 5.1). The elastic constants were estimated from Hounsfield values of the same ten CT [Gupta et al. 2004]. The humeral head was free to move within the glenoid cavity. A frictionless contact was assumed between the two cartilage layers. The scapula was fixed. The relative rotation of the humerus and the joint force were imposed as predicted by the musculoskeletal model. The model was implemented in Abaqus 6.13 (Simulia, Dassault Systèmes, France). We considered a quasi-static problem and used the implicit solver. Bones were meshed with quadratic tetrahedral elements. Cartilages were meshed with hybrid quadratic tetrahedral elements to model incompressibility. The constitutive law for cartilage was implemented in a user subroutine UHYPER. A mesh sensitivity analysis was performed using a strain energy criterion. The model predicted the (von Mises) strain within the glenoid cartilage layers, and the humeral head translation [Khan and Huang 1995]. We further analysed the volume of cartilage that was exposed to strains higher than 15 %.

5.2.3   Supraspinatus Tendon Model

The supraspinatus tendon model included the scapula, humerus and the lateral part of the supraspinatus tendon at its insertion on the humeral head. The tendon was reconstructed out of the same MRI images. The supraspinatus tendon insertion was estimated from a cadaveric study [Curtis et al. 2006]. The tendon was modelled with an anisotropic hyperelastic

Tissue	Constitutive Law
Cartilage	$W = \alpha e^{(\beta(I_1 - 3))} - \alpha\beta(I_2 - 3)$ $\alpha = 1.148\,\mathrm{MPa} \qquad \beta = 1.173$
Glenoid Cortical	Linear elastic $E = 190\,\mathrm{MPa} \qquad \nu = 0.3$
Glenoid Trabecular	Linear elastic $E = 60\,\mathrm{MPa} \qquad \nu = 0.3$
Humerus Cortical	Linear elastic $E = 120\,\mathrm{MPa} \qquad \nu = 0.3$
Glenoid Trabecular	Linear elastic $E = 45\,\mathrm{MPa} \qquad \nu = 0.3$
Supraspinatus Tendon	$W = \frac{\mu}{4}\left(\frac{1}{\alpha}[e^{\alpha(I_p - 1)} - 1] + \frac{1}{\beta}[e^{\beta(K - 1)} - 1]\right)$ $\mu = 29.08\,\mathrm{MPa}\,, \alpha = 13.24, \beta = 0, w_0 = 0.81$

Table 5.1 – Constitutive laws for bone, cartilage, and tendon.

constitutive law, and identified with experimental measurements [Ehret et al. 2011, Engelhardt et al. 2015a]. Scapula and humerus were rigid. A frictionless contact was defined between the supraspinatus tendon and the humeral head. The force applied on the tendon was obtained from the musculoskeletal model, while the motion of the humerus relative to the scapula was taken from the cartilage model. The model was also implemented in Abaqus 6.13. We considered a quasi-static problem and used the implicit solver. The constitutive law for tendon tissue (Table 5.1) was implemented in a user subroutine UMAT. The tendon was meshed quadratic tetrahedral elements. A mesh sensitivity analysis was performed using a strain energy criterion. With this model, we evaluated the volume of tendon exposed to maximum principal strains higher than 3 % and measured the subacromial space.

5.2.4 Acromion Index and Glenoid Inclination

We artificially varied the acromion index and the glenoid inclination of the models in the range of typical values [Hughes et al. 2003, Nyffeler et al. 2006, Wong et al. 2003]. These two parameters were measured on 2D views of the scapula projected on the scapular plane [Terrier et al. 2014a].

The acromion index was defined as the distance between glenoid plane and the most lateral point of the acromion, divided by the distance between glenoid plane and the most lateral point of the greater tubercle on the humeral head. The acromion index of our healthy volunteer

was 0.71. We varied the length of the acromion in the model by extending or shortening the acromion, along a direction perpendicular to the glenoid plane (Figure 5.2, left image). Muscle insertions on the acromion were moved accordingly. The reference normal acromion index was set at 0.65 [Nyffeler et al. 2006]. The minimum and maximum acromion index were 0.5 and 0.8 [Kim et al. 2012, Nyffeler et al. 2006].

The glenoid inclination was defined as the angle between the glenoid centre line projected onto the scapula plane and the scapular axis [Terrier et al. 2014a]. The glenoid inclination of our healthy volunteer was 7 degrees. We varied the glenoid inclination in the model by rotating the glenoid around the glenohumeral rotation centre (Figure 5.2, right image). Rotation axis was perpendicular to the scapular plane. We considered three values of glenoid inclination. The reference normal glenoid inclination was set at 5 degrees. The minimum and maximum glenoid inclination was -5 and 15 degrees [Hughes et al. 2003].

We related acromion index and glenoid inclination to the critical shoulder angle. This angle is defined as the angle between two lines [Moor et al. 2013]. The first line connects the inferior border of the glenoid cavity with the superior border of the glenoid cavity. The second line connects the inferior border of the glenoid cavity with the lateral edge of the acromion. This angle is thus determined by the previous two parameters. The critical shoulder angle of our healthy volunteer was 32.9 degrees. With the chosen values for acromion index and glenoid inclination, the critical shoulder angle range from 28 to 38 degrees was covered.

Within the range of variability of the acromion index and glenoid inclination, we evaluated their effect on glenohumeral joint force, supraspinatus force, glenoid cartilage strain, superior humeral head migration, supraspinatus tendon strain, and subacromial space at an arm elevation of 60 degrees abduction. To quantify the strain level, we considered the volume
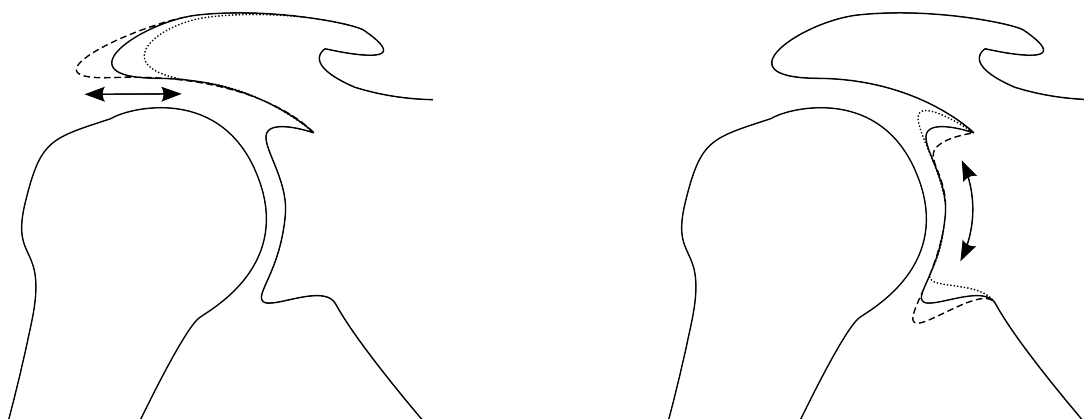

Figure 5.2 – The acromion length is varied by moving the lateral acromion edge perpendicular to the glenoid plan (left). The glenoid inclination is varied by rotating the glenoid cavity around the glenohumeral rotation center (right).

of tissue undergoing strains larger than a predefined threshold. For cartilage, the threshold was at 15 % strain, for tendon at 3 % strain respectively. These values correspond to 50 % of reported failure strains [Kerin et al. 1998, Sasazaki et al. 2006, Stavropoulou et al. 2009]. We compared these quantities to the reference configuration with an acromion index of 0.65 and glenoid inclination of 5 degrees.

5.3 Results

5.3.1 Musculoskeletal Model

The supraspinatus force at 60 degrees abduction was 73 N in the reference configuration. The supraspinatus force decreased with increasing acromion index (Figure 5.3, left). The supraspinatus force showed a drop at -5 degrees glenoid inclination compared to the reference configuration (Figure 5.3, right).

The glenohumeral joint reaction force at 60 degrees abduction was 274 N in the reference configuration. The joint reaction force decreased with increasing acromion index (Figure 5.4, left). The joint reaction force showed a drop at -5 degrees glenoid inclination compared to the reference configuration (Figure 5.4, right).
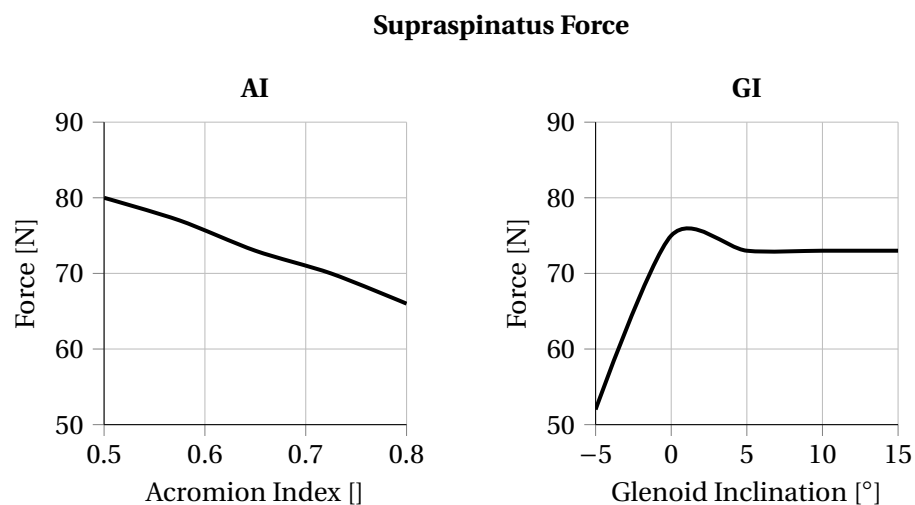
Supraspinatus Force

Figure 5.3 – Supraspinatus force at 60 degrees abduction under variation of acromion index (AI) and glenoid inclination(GI).
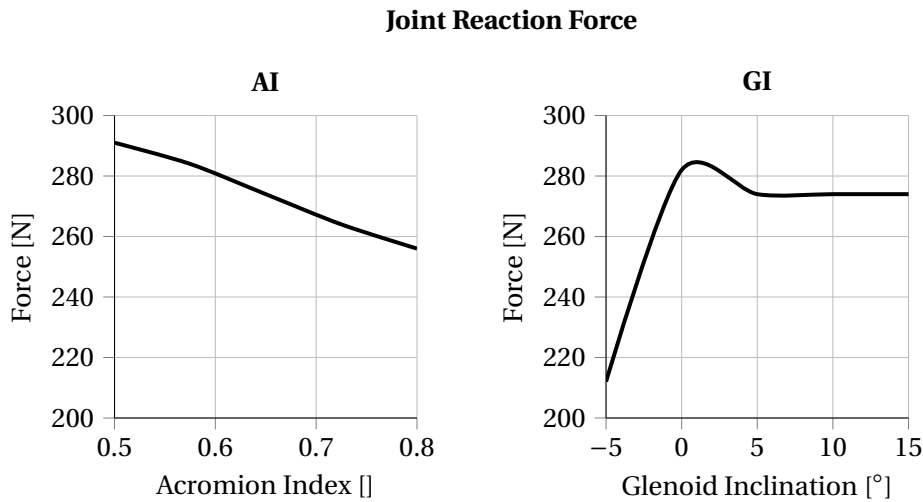
Joint Reaction Force

Figure 5.4 – Glenohumeral joint reaction forces at 60 degrees abduction under variation of acromion index (AI) and glenoid inclination (GI).

5.3.2   Cartilage Model

The maximum strain was located at the cartilage-bone interface (Figure 5.5). The cartilage volume exposed to strains higher than 15 % was 100 mm^3 in the reference configuration. The high strain cartilage volume decreased with increasing acromion index (Figure 5.6). At -5 degrees glenoid inclination, the high strain cartilage volume was lower compared to larger glenoid inclinations (Figure 5.6).

Superior humeral head migration was 2.9 mm in the reference configuration. Humeral head migration increased for increasing acromion index and increasing glenoid inclination.

5.3.3   Supraspinatus Tendon Model

Maximal tendon strain was located at the articular (humeral) side of the tendon insertion. The tendon volume exposed to higher maximum principal strains than 3 % was 32 mm^3 in the reference configuration. High strain tendon volume decreased for increasing acromion index (Figure 5.7). At -5 degrees glenoid inclination, the high strain tendon volume was lower compared to larger glenoid inclinations (Figure 5.7).

The subacromial space was 0.4 mm in the reference configuration. The subacromial space decreased with increasing acromion index and increasing glenoid inclination.

5.4   Discussion

Several clinical studies reported a statistical correlation between scapular anatomy and the occurrence of degenerative shoulder pathologies. Upward inclination of the glenoid and lateral
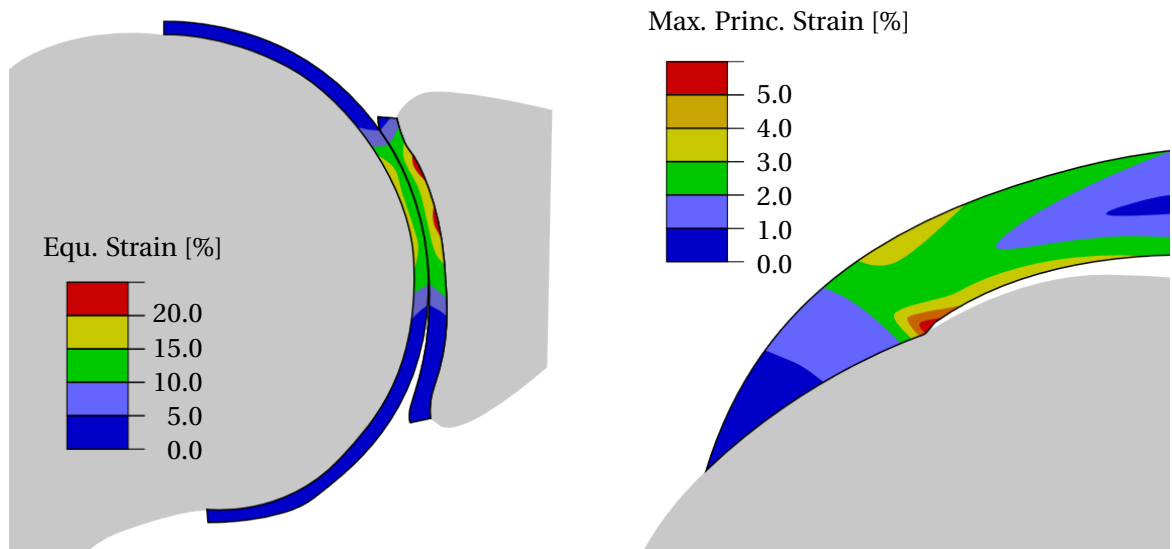
Figure 5.5 – Cut view (scapular plane) of the strain distribution in the cartilage (left) and tendon (right). Maximum strains were located at the cartilage-bone interface (left) and on the articular side of the tendon insertion (right).
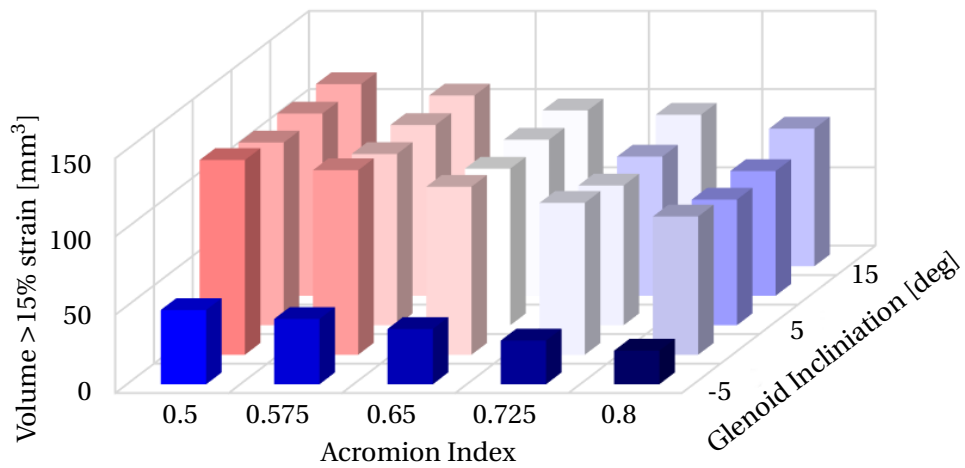
Figure 5.6 – Critical cartilage strain volume in dependence of acromion index and glenoid inclination.
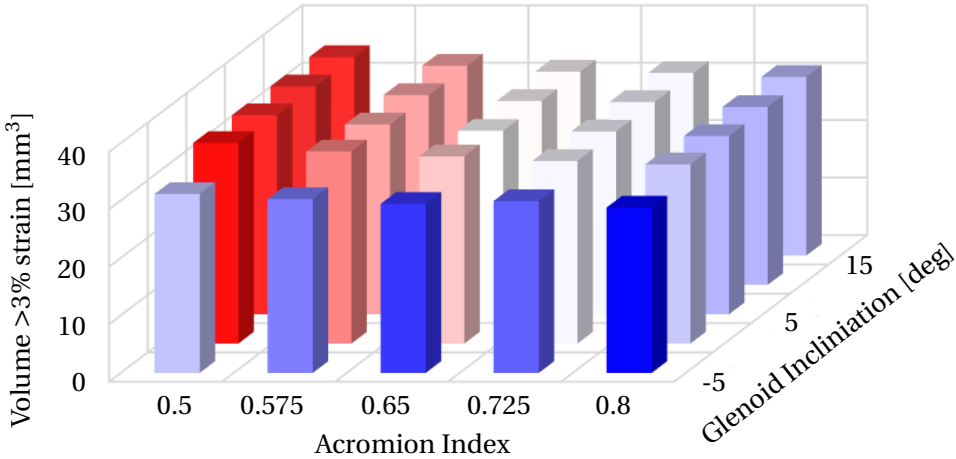
Figure 5.7 – Critical tendon strain volume in dependence of acromion index and glenoid inclination.
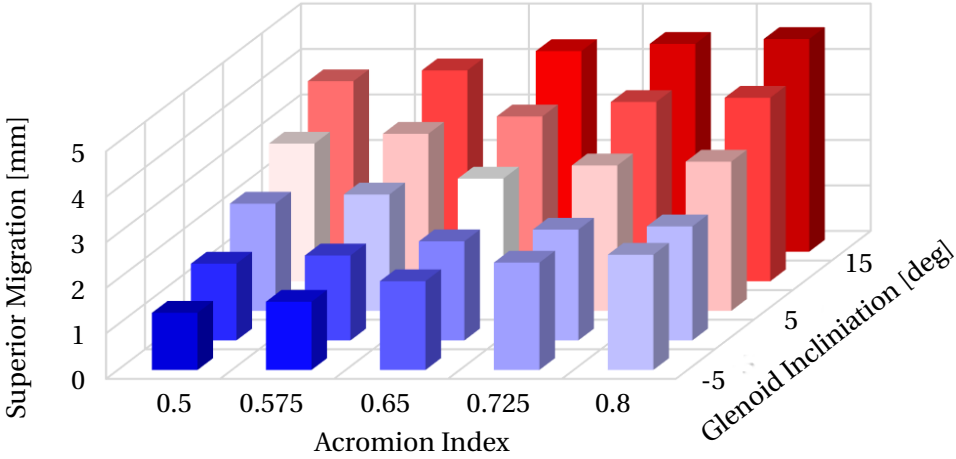
Figure 5.8 – Superior humeral head migration in dependence of acromion index and glenoid inclination.

extension of the acromion were associated to rotator cuff tears, while downward inclination of the glenoid and short acromion were associated to glenohumeral osteoarthritis [Hughes et al. 2003, Moor et al. 2013, Nyffeler et al. 2006, Tétreault et al. 2004, Wong et al. 2003]. In the present paper, we developed and applied a numerical model of the shoulder to evaluate the effect of these two anatomical parameters on glenoid cartilage strain, subacromial space, and supraspinatus tendon strain. Assuming that cartilage strain is mechanically related to osteoarthritis, and subacromial space and tendon strain are related to supraspinatus tendon tears, the model predictions confirmed the reported clinical observations. In addition, the model predicted that the effect of the acromion index was more important than the effect of the glenoid inclination.

The two anatomic parameters analysed here were the acromion index and the glenoid inclination. For healthy subjects, acromion index and the glenoid inclination are reported to be respectively 0.64 and 1 degree,[Hughes et al. 2003, Nyffeler et al. 2006]. which corresponds to a CSA of 30 degrees. This value is consistent with the CSA of 33 degrees reported for asymptomatic shoulders with normal rotator cuffs and no osteoarthritis [Moor et al. 2013]. The acromion index and the glenoid inclination of our healthy volunteer were respectively 0.71 and 7 degrees, corresponding to a critical shoulder angle of 32.8 degrees.

The supraspinatus muscle force was sensitive to the acromion length. The glenoid inclination had small effect on supraspinatus muscle force, except for negative glenoid inclination. The same tendency could be observed for the joint reaction force. This behaviour can be explained with the stabilizing effect of negative glenoid inclinations on the glenohumeral joint [Terrier et al. 2014b]. A longer acromion decreased the supraspinatus muscle force. Increasing the acromion length increases the deltoid moment arm, reducing thus its required force, and the force of the supraspinatus. As a consequence, the glenohumeral joint force is also reduced. The numerical results confirmed the hypothesis, that a short acromion increased joint reaction forces [Moor et al. 2013, Nyffeler et al. 2006]. For a short acromion, the deltoid force points more towards the glenoid cavity. In addition, the numerical results predict higher muscle forces due to decreased moment arms. The changes in supraspinatus and joint reaction force were observed at 60 degrees abduction. Higher abduction angles are however seldom [Coley et al. 2008].

The cartilage underwent a three dimensional deformation. We thus chose the equivalent (Mises) strain to capture the complex deformation in one scalar value. The strain analysis was done at an abduction angle of 60 degrees. The angle has been chosen since joint reaction forces were most sensitive to anatomic parameter changes at this position. We justify this choice further by the fact that most of our daily movements occur below 60 degrees of abduction [Coley et al. 2008]. Cartilage strain increased as joint force increased. The numerical results predicted an increase in cartilage strain for short acromion. The results were consistent with radiologic findings that a short acromion is associated to a higher risk of osteoarthritis [Moor et al. 2013, Nyffeler et al. 2006]. Increased glenoid inclination compared to the reference configuration had no effect on cartilage strain. Negative glenoid inclination caused a drop in

cartilage strain, which is associated to the reduced joint reaction force for negative glenoid inclinations. To the authors' knowledge, no link between glenoid inclination and osteoarthritis is reported in the literature so far. The effect of negative glenoid inclinations on osteoarthritis should be further investigated by clinical studies.

Since the supraspinatus tendon was loaded along its longitudinal direction, tensile strains were the dominant deformation type. We thus chose the maximum principal (tensile) strains to evaluate tendon deformation. Highest tendon strains were observed at the articular side of the tendon insertion, a site were tendon tears are frequently observed in clinics [Tempelhof et al. 1999]. Tendon strains were following the previous findings on supraspinatus forces: increased supraspinatus force induced increased supraspinatus tendon strains and vice versa. The tendon strains were consequently higher for a shorter acromion. This result seems contradictory to the radiologic findings, which correlated an increased risk for tendon tears for a long acromion [Moor et al. 2013, Nyffeler et al. 2006]. However, the radiologic studies did not precise at which site the tendon tears occurred. Following the numerical results, tears at the insertion site should occur more often in patients with a short acromion due to elevated tendon strains.

The subacromial space was obviously associated to the humeral head translation in the glenoid fossa. Lengthening the acromion increased superior humeral head translation and thus decreased the subacromial space. Increasing glenoid inclination increased the superior humeral head translation and thus decreased the subacromial space. Putting these findings into context with the radiologic observations [Moor et al. 2013, Nyffeler et al. 2006], we can conclude that a long acromion would increase the risk of supraspinatus tendon impingement and associated tears. Our numerical predictions could also confirm the observation of an increased risk of tendon impingement for increased glenoid inclination [Wong et al. 2003].

The tissue strains predicted by the finite element models were of elastic strains. Plastic deformation as well as tissue softening or hardening due to fatigue damage were not included in this model. However, the predicted elastic strains were below experimental failure strains. The contribution of irreversible deformations to the total strain was assumed to be small. We further linked elastic strains to degenerative joint disease that accumulate over time. The goal of this work was however to analyse changes in cartilage load, tendon load and humeral head migration rather than modelling the degeneration of the tissues.

The strength of the presented work was to provide a generic numerical model of the shoulder, allowing to vary independently specific anatomical parameters of the scapular anatomy. We could thus evaluate the effect of these anatomical parameters on biomechanical quantities such as cartilage strain and subacromial space, which are linked to osteoarthritis and supraspinatus tendon tears. The most important limitation is certainly associated to the single anatomy of a single volunteer. Ideally, we should have modelled a series of patients with different pathologies, and a control group, to account for the other anatomical variability. This option of patient-specific modelling is however too time consuming yet. Although the

numerical results were consistent with clinical observations, the relative changes of maximum cartilage and tendon strains were small (< 2.5 %). The results were obtained for a quasi-static (slow) abduction movement with no weight in the hand. Even if this movement is typical of activities of daily living, the model might be applied to simulate more complex movement.

5.5   Conclusion

The acromion length and glenoid inclination have been both associated to glenohumeral osteoarthritis and supraspinatus tendon tears. The hypothetical mechanical causality link was confirmed with a parametric shoulder model. This parametric study suggests a greater importance of the lateral extension of the acromion for cartilage load and associated osteoarthritis, and a greater importance of the glenoid inclination for humeral head migration and associated tendon tears. Although degenerative shoulder disorders are known to be multi-causal, the anatomic parameters have certainly a strong contribution. A better understanding of the relative importance of these anatomical parameters on the occurrence of osteoarthritis and tendon tears might help in planning the optimal treatment of these pathologies.

5.B Bibliography

Brandt K. D., Dieppe P., and Radin E.: Etiopathogenesis of osteoarthritis. *Medical Clinics of North America*, 93(1):1–24, 2009.

Buckwalter J. A. and Martin J. A.: Osteoarthritis. *Advanced Drug Delivery Reviews*, 58(2): 150–167, 2006.

Coley B., Jolles B. M., Farron A., and Aminian K.: Arm position during daily activity. *Gait Posture*, 28(4):581–587, 2008.

Curtis A. S., Burbank K. M., Tierney J. J., Scheller A. D., and Curran A. R.: The insertional footprint of the rotator cuff: An anatomic study. *Arthroscopy*, 22(6):603–609.e1, 2006.

Egloff C., Hügle T., and Valderrabano V.: Biomechanics and pathomechanisms of osteoarthritis. *Swiss Med Wkly*, 142:w13583, 2012.

Ehret A. E., Böl M., and Itskov M.: A continuum constitutive model for the active behaviour of skeletal muscle. *J Mech Phys Solids*, 59(3):625–636, 2011.

Engelhardt C., Ingram D., Müllhaupt P., Farron A., Becce F., Pioletti D. P., and Terrier A.: Effect of partial-thickness tear on loading capacities of the supraspinatus tendon: A finite element analysis. *CMBBE*, 2015a.

Engelhardt C., Camine V. M., Ingram D., Muellhaupt P., Farron A., Pioletti D., and Terrier A.: Comparison of an EMG-based and a stress-based method to predict shoulder muscle forces. *Comp Methods Biomech Biomed Engin*, 18(12):1272–1279, 2015b.

Garner B. A. and Pandy M. G.: A kinematic model of the upper limb based on thevisible human project (vhp) image dataset. *Comput Methods Biomech Biomed Engin*, 2:107–124, 1997.

Garner B. A. and Pandy M. G.: Musculoskeletal model of the upper limb based on the visible human male dataset. *Comput Methods Biomech Biomed Engin*, 4:93–126, 2000a.

Garner B. A. and Pandy M. G.: The obstacle-set method for representing muscle paths in musculoskeletal models. *CMBBE*, 2000b.

Gupta S., van der Helm F. C. T., and van Keulen F.: Stress analysis of cemented glenoid prostheses in total shoulder arthroplasty. *Journal of Biomechanics*, 37(11):1777 – 1786, 2004.

Hasvold T. and Johnsen R.: Headache and neck or shoulder pain- frequent and disabling conditions in the general population. *Scandinavian Journal of Primary Health Care*, 1993.

Hughes R. E., Bryant C. R., and Hall J. M.: Glenoid inclination is associated with full-thickness rotator cuff tears. *Clin Orthop Relat Res*, 407:86–91, 2003.

Ingram D., Engelhardt C., Farron A., Terrier A., and Müllhaupt P.: Muscle moment-arms: a key element in muscle force estimation. *CMBBE*, 18:506–513, 2015a.

Ingram D., Engelhardt C., Farron A., Terrier A., and Müllhaupt P.: Improving anterior deltoid in a musculoskeletal shoulder model - an analysis of the torque-feasible space at the sternoclavicular joint. *CMBBE*, 2015b.

Kerin A. J., Wisnom M. R., and Adams M. A.: The compressive strength of articular cartilage. *Proceedings of the Institution of Mechanical Engineers, Part H: Journal of Engineering in Medicine*, 212(4):273–280, 1998.

Khan A. S. and Huang S., editors.: *Continuum Theory of Plasticity*. Wiley, 1995.

Kim J., Ryu K., Hong I., Kim B., and Kim J.: Can a high acromion index predict rotator cuff tears? *International Orthopaedics*, 36(5):1019–1024, 2012.

Mitchell C., Adebajo A., Hay E., and Carr A.: Shoulder pain: diagnosis and management in primary care. *BMJ*, 331(7525):1124–1128, 2005.

Moor B. K., Bouaicha S., Rothenfluh D. A., Sukthankar A., and Gerber C.: Is there an association between the individual anatomy of the scapula and the development of rotator cuff tears or osteoarthritis of the glenohumeral joint? A radiological study of the critical shoulder angle. *Bone and Joint Journal*, 95 B(7):935–941, 2013.

Nho S. J., Yadav H., Shindle M. K., and MacGillivray J. D.: Rotator cuff degeneration: Etiology and pathogenesis. *Am J Sports Med*, 36(5):987–993, 2008.

Nyffeler R. W., Werner C. M., Sukthankar A., Schmid M. R., and Gerber C.: Association of a large lateral extension of the acromion with rotator cuff tears. *The Journal of Bone & Joint Surgery*, 88(4):800–805, 2006.

Pioletti D. P. and Rakotomanana L. R.: Non-linear viscoelastic laws for soft biological tissues. *European Journal of Mechanics a-Solids*, 19(5):749–759, 2000.

Pope D. P., Croft P. R., Pritchard C. M., and Silman A. J.: Prevalence of shoulder pain in the community: The influence of case definition. *Annals of the Rheumatic Diseases*, 56(5): 308–312, 1997.

Renström P. and Hach T.: *Insertional tendinopathy in sports*. 2005.

Sasazaki Y., Shore R., and Seedhom B.: Deformation and failure of cartilage in the tensile mode. *Journal of Anatomy*, 208(6):681–694, 2006.

Stavropoulou E., Dafalias Y., and Sokolis D.: Biomechanical and histological characteristics of passive esophagus: Experimental investigation and comparative constitutive modeling. *Journal of Biomechanics*, 42(16):2654–2663, 2009.

Tempelhof S., Rupp S., and Seil R.: Age-related prevalence of rotator cuff tears in asymptomatic shoulders. *J Shoulder Elbow Surg*, 8(4):296 – 299, 1999.

Terrier A., Ston J., Larrea X., and Farron A.: Measurements of three-dimensional glenoid erosion when planning the prosthetic replacement of osteoarthritic shoulders. *Bone and Joint Journal*, 96 B(4):513–518, 2014a.

Terrier A., Ston J., Larrea X., and Farron A.: Measurements of three-dimensional glenoid erosion when planning the prosthetic replacement of osteoarthritic shoulders. *Bone & Joint Journal*, 96B(4):513–518, 2014b.

Terrier A., Aeberhard M., Michellod Y., Müllhaupt P., Gillet D., Farron A., and Pioletti D.: A musculoskeletal shoulder model based on pseudo-inverse and nullspace optimization. *Med Eng Physics*, 32:1050–1056, 2010.

Tétreault P., Krueger A., Zurakowski D., and Gerber C.: Glenoid version and rotator cuff tears. *J Orthop Res*, 22:202–207, 2004.

Wong A. S., Gallo L., Kuhn J. E., Carpenter J. E., and Hughes R. E.: The effect of glenoid inclination on superior humeral head migration. *J Shoulder Elbow Surg*, 12:360–364, 2003.

6 Conclusions

6.1 Summary of Findings

Shoulder disorders represent a group of debilitating orthopaedic conditions, of which osteoarthritis and rotator cuff tears are the most common [Hasvold and Johnsen 1993, Pope et al. 1997]. Despite a frequent occurrence the underlying triggers are not fully understood yet. A long term multi-causal pathogenesis is assumed, including metabolic, inflammatory, and mechanical contributions [Renström and Hach 2005, Buckwalter and Martin 2006]. It is nowadays well accepted that biomechanics play an important role in joint homeostasis. Until recently the main focus in biomechanical research lied on the activity level and lifestyle of affected patients. In the last decade, several studies found in addition that the anatomic shape of the shoulder blade, described through anatomic parameters, can be statistically linked to the occurrence of osteoarthritis and rotator cuff tears: these parameters are the lateral extension of the acromion and the glenoid inclination [Hughes et al. 2003, Wong et al. 2003, Tétreault et al. 2004, Nyffeler et al. 2006, Moor et al. 2013].

The aim of this dissertation was to provide a mechanical explanation for this clinical observation. Three generic numerical shoulder models were specifically developed to answer this question. Numerical modelling has the advantage of giving access to variables that are not measurable in vivo without considerable invasive effort. The development of biomechanical models is however challenging: the shoulder's musculoskeletal system is a complicated mechanism and surrounding tissue have complex material characteristics.

The first model was a musculoskeletal model of the shoulder complex. The model calculated muscle forces for 42 muscle segments and joint reaction forces. The underlying skeleton was modelled as rigid bones connected by ideal ball joints. This mechanism was then spanned by muscle cables, wrapping around obstacles to replicate the centroid lines following the obstacle set method. Inverse dynamics computed the joint torques. An optimisation routine estimated the forces by minimizing a cost function. With this model, we introduced a technique to vary the number of cables per muscle segment. Origin and insertion sites were interpolated with cubic splines, on which the cables were evenly distributed. We further developed a new

kind of stability criterion, which is not formulated as a constraint on a specified boundary, but implemented into the optimisation routine as a smooth stability potential. The model had further the flexibility to be adapted to given anatomic parameters: acromion index and glenoid inclination.

The second model was developed to calculate contact pressure, cartilage strains, and humeral head translations. It thus contained the bones and cartilages of the glenohumeral joint. Cortical bone thickness and Young's modulus for cortical and trabecular bone were derived from CT scans. The cartilage itself was modelled with an hyperelastic exponential constitutive law. The constitutive parameters were identified with experimental data on cartilage compression. Between the cartilages, a frictionless contact was defined. The joint reaction force obtained with the musculoskeletal model served as input for the cartilage model. The joint reaction force pressed the humeral head onto the glenoid cavity. As the humeral head was not restricted in his displacement, it could migrate on the glenoid cavity allowing for an estimation of humeral head translation.

The third model was developed to estimate supraspinatus tendon strains and subacromial space. To do this, the model used the supraspinatus force calculated by the musculoskeletal model and the humeral head translations obtained from the cartilage model. The tendon was modelled with an anisotropic hyperelastic constitutive law. The constitutive equations were implemented into a user subroutine of the finite element software Abaqus. Material parameters were identified in both fibre as well as in transverse direction. The elasticity tensor was numerically approximated with a forward differentiation algorithm.

The three models were used to test the possible effect of anatomical parameters on the reported occurrence of osteoarthritis and tendon tears. More specifically, we varied the length of the acromion and the superior-inferior inclination of the glenoid cavity and observed changes in shoulder muscle forces, glenohumeral joint forces, cartilage strain, tendon strain, and subacromial space.

This numerical parametric study predicted that all mechanical quantities considered here were more sensitive to the lateral extension of the acromion than the glenoid inclination. Assuming increased cartilage strain is a risk factor for osteoarthritis, the parametric study confirmed the radiologic findings that a short acromion is associated to the occurrence of osteoarthritis. The parametric study could further show a reduced subacromial space for a long acromion, which can be interpreted as an increased risk for tendon impingement and associated tears. We further observed an increase in tendon strains close to the tendon insertion for short acromion. At first glance, this seems to be contradictory to the radiologic findings, which predicted an increased risk for tendon tears for long acromion. However, the radiologic studies did not distinguish between tendon tears due to impingement and tears at the insertion due to repeated overloading.

6.2 General Discussion

Although the numerical modelling has greatly improved, there remains a gap between the simulation and the real system. The reason for this lies in the simplifying assumption that have to be made to master the complexity of the biomechanical system. The assumptions applied on the presented numerical models correspond to the actual state of the art, which however does not exclude the need for validation. In the case of biomechanics, the validation is an especially challenging task, as several of the biomechanical variables can not be measured in vivo. The validation should thus be seen as an ongoing process as experimental and clinical methods improve. The models ability to reproduce the real system must be continuously challenged.

The developer of numerical models have further to choose whether to replicate a single patient in a patient specific model or to provide a generic model which allows to derive general conclusions. Both approaches are challenging: in patient specific models it is difficult to obtain all needed physiologic parameters from the same patient, especially if measurements require invasive techniques. On the other hand, a generic model requires physiologic parameters that fulfill statistical requirements, which usually means repetitive measurements on large sample sizes.

The most challenging part of finite element modelling of biological tissues remains the identification of material parameters. Complex constitutive equations derived on the principles of continuum theory can be found in literature. However, more material parameters neccesites more experimental data for identification. Especially when modelling human tissue, sample sizes are usually small which makes it difficult to achieve statistical validation. Noninvasive test methods like ultrasound p.e. present a promising approach at least for superficial structures. Such techniques would allow to develop fully patient-specific models regarding anatomy, kinematics, and tissue properties and support the trend in patient specific modelling.

The implementation of constitutive laws in finite element environments is also challenging, especially the calculation of the 4th order elasticity tensor. To overcome the last point, an approximation algorithm was developed in this work, which can be applied to any kind of constitutive law. Development time for specific constitutive laws can be reduced by using this algorithm. There is however one drawback: the approximation might lead to convergence problems in complex loading conditions. In such a case, there is no getting around the analytical derivation of the elasticity tensor.

The presentation of three numerical models all based on the same in vivo MRI images was a novum. The decoupling into three models was necessary to reduce the numerical complexity. The decoupling does induce a further source of error which would require a more profound sensitivity analysis of propagating errors before using such a model in clinical applications. The coupling of muscle force estimation and humeral head translation should not significantly change the results. Indeed, the changes in muscle moment arms due to humeral head translations are an order of magnitude smaller than the moment arms. The coupling of

humeral head translation and tendon impingement is considered to be more important, as the subacromial contact between tendon and shoulder blade will restrict superior humeral head migration. Developing a shoulder model that can provide all biomechanical variables will be a challenging task. Analysing the interaction between the variables might be an interesting and promising research goal for future works.

There are strong indications both from clinical as well as biomechanical perspective, that a joint's surrounding anatomy plays a significant role in the joint's homeostasis. The present work was the first one that analysed the the biomechanical variables muscle force, joint force, cartilage strain, subacromial space and tendon strain in dependence of anatomical parameters. The work was thus a retrospective study of clinical observations. A possible next step would be to develop the method further to be able to predict clinical outcomes in the sense of prospective studies with patient specific shoulder models.

One reported experimental study analysed the effect of the critical shoulder angle on the supraspinatus forces [Gerber et al. 2014]. The cited study also came to the conclusion, that a lateral extension of the acromion increased the risk for supraspinatus tears due to the tendency of an increased superior humeral head shift. [Gerber et al. 2014] indicates an increased stabilising force as reason for the increased risk of supraspinatus tears. The question remains open, if a long acromion leads to supraspinatus tears due to unphysiological tendon load or tendon impingement. In this case, an analysis of the tear location could clarify this: following our numerical results, unphysiological tendon load should induce tears at the articular side of the tendon close to its insertion, while tendon impingement should induce tears on the bursal side below the acromion.

To the author's knowledge no other experimental or numerical study existed that analysed the anatomic parameters with a view on osteoarthritis.

6.3   Future Work

6.3.1   Musculoskeletal Model

Modelling a musculoskeletal system is always a compromise between the level of complexity of the used muscle description and the number of muscles. The mathematical complexity and computational effort of the problem must stay within manageable ranges. In this work, we decided to consider the entire upper limb, and thus we had to include 42 muscle segments. We were therefore constrained to limit the muscle complexity to cables. The muscle model could be further extended by including the muscle's internal dynamic limitations of force exertion depending on muscle length and contraction velocity [Garner and Pandy 2003]. Although the geometric modelling of muscles as cables is widely used, only few studies analysed how to implement it correctly [van der Helm and Veenbaas 1991, Ingram 2015]. The geometric modelling of the muscles should be revised by analysing each muscles contribution to the

joint reaction force. This would optimize the global muscular interplay towards a natural stable solution and might make the implementation of a stability criterion unnecessary.

Although inverse dynamics provide a handy way to approach the problem of muscle force estimation, this method are unsuitable to predict kinematic variables. In the case of the shoulder however, the humeral head translations and muscle forces are strongly linked through the active stabilisation of the humeral head by the rotator cuff muscles. To couple the prediction of humeral head movement and muscle force estimation, a forward dynamic approach might be considered. This would probably require some form of iterative method, which corrects muscle activation pattern each time the model is run until the desired movement is executed in an acceptable range.

6.3.2 Cartilage Model

The deformation of cartilage under compression can be replicated with hyperelastic constitutive laws. However, the material parameters are only valid for a given strain rate. To model dynamic movements, the cartilage model should thus be extended by adding the visco elastic, strain rate dependent material properties. The difficulties of this task are less rooted in the constitutive theory, which provides corresponding material models, but rather in the availability of experimental data for the identification of the time dependent material parameters.

6.3.3 Tendon Model

The main limitation of the tendon model lies in the nature of the continuum assumption: interfibre sliding cannot be replicated. Especially under bending loading occurring during wrapping of the tendon around the humeral head, strain and stress predictions might be overestimated. The interfibre sliding has in such situations a relaxing effect which is not taken into account. Consequently, a microstructural modelling of the tendon might be more appropriate to simulate tendons under complex loading conditions. The implemented constitutive law and its identification could be used further in such a microstructural model e.g. to model the single fibres, which could be bundled within a deformable membrane. In the current implementation, the elasticity tensor is approximated with a forward differentiation algorithm. In our simulations, we did not experience convergence issues. Under complex loading conditions, it might be necessary to implement an analytical calculation of the elasticity tensor.

For now, the model was limited to the lateral tip of the supraspinatus tendon. Regarding the complex architecture of the supraspinatus muscle and the transition to the tendon, the whole muscle tendon unit should be included into the model. This would not only lead to a more realistic force transmission into the tendon, but would also provide better guidance and more realistic positioning. The constitutive equation for tendon tissue presented in this work can

be extended by an active term to model muscle contraction. Identification of the material parameters for passive and active muscle behaviour will be however a challenging task.

6.3.4 Anatomic Parameter Study

In this work, we investigated a parametric study on acromion length and glenoid inclination. Both geometric measurements were varied artificially without link to real anatomical scapula shapes. Two improve the study further, we propose two options. First, the natural shape variation of the scapula has been analysed in various statistical shape modelling studies. These studies could be consulted when artificially varying parameters to ensure that the resulting scapula shape stays within realistic ranges. The second option would be to model real scapulas. This would require a data analysis of a CT database to find a set of CT scans that cover the range of the anatomic parameter of interest.

The study should further be extended by the analysis of dynamic motion. When considering dynamic effects such as inertia during fast executed movements or external impacts, we expect the impact of anatomic parameters to become more important.

The anatomic dataset used in this study was taken from MRI scans of a young male volunteer. A comparison between male and female anatomy, different age groups, and different lifestyles would be interesting. Further anatomic parameters like anterior-posterior inclination might also be included in the analysis.

6.4 Clinical Perspective

The knowledge about anatomical parameters and their impact on shoulder diseases can give insight into predisposing factors for osteoarthritis and rotator cuff tears. However, the anatomic shape of the shoulder is determined once the growth is completed at the end of the adolescence. During adult life the changes in bone geometry due to remodelling are limited. Correcting the scapula geometry with invasive surgical procedures is definitely not justified by the finding of an out of range anatomic parameter. However, the knowledge about anatomic parameters might be included in the planing of total joint replacement surgeries with the aim to prevent complications and extend prosthesis lifetime. In the prophylaxis or conservative treatement strategies, physiotherapeutic measures might help to improve muscular balance and coordination in order to compensate the unfavorable impact of extreme anatomic shapes.

Overall, the idea of describing the scapula shape with anatomic parameters is quite new. The research of their impact on joint diseases is still in an early phase of their development. There is evidence that these parameters play a role in the multicausal process of disease development. Before this knowledge can successfully applied in clinical daily life, the importance of these parameters should be further evaluated, dominant parameters should be identified, and it might also be necessary to introduce parameters that take into account the three dimensional

structure of the shoulder blade. The research activities in this field need thus further input from the medical and biomechanical research community so that the knowledge about anatomic parameters can help to prevent, stop, or one day even reverse debilitating shoulder diseases.

6.B   Bibliography

Buckwalter J. A. and Martin J. A.: Osteoarthritis. *Advanced Drug Delivery Reviews*, 58(2): 150–167, 2006.

Garner B. A. and Pandy M. G.: Estimation of musculotendon properties in the human upper limb. *Annals of Biomedical Engineering*, 31:207–220, 2003.

Gerber C., Snedeker J. G., Baumgartner D., and Viehöfer A. F.: Supraspinatus tendon load during abduction is dependent on the size of the critical shoulder angle: A biomechanical analysis. *Journal of Orthopaedic Research*, 32(7):952–957, 2014.

Hasvold T. and Johnsen R.: Headache and neck or shoulder pain- frequent and disabling conditions in the general population. *Scandinavian Journal of Primary Health Care*, 1993.

Hughes R. E., Bryant C. R., and Hall J. M.: Glenoid inclination is associated with full-thickness rotator cuff tears. *Clin Orthop Relat Res*, 407:86–91, 2003.

Ingram D.: *Musculoskeletal Model of the Human Shoulder for Joint Force Estimation*. PhD thesis, EPFL, Lausanne, 2015.

Moor B. K., Bouaicha S., Rothenfluh D. A., Sukthankar A., and Gerber C.: Is there an association between the individual anatomy of the scapula and the development of rotator cuff tears or osteoarthritis of the glenohumeral joint? A radiological study of the critical shoulder angle. *Bone and Joint Journal*, 95 B(7):935–941, 2013.

Nyffeler R. W., Werner C. M., Sukthankar A., Schmid M. R., and Gerber C.: Association of a large lateral extension of the acromion with rotator cuff tears. *The Journal of Bone & Joint Surgery*, 88(4):800–805, 2006.

Pope D. P., Croft P. R., Pritchard C. M., and Silman A. J.: Prevalence of shoulder pain in the community: The influence of case definition. *Annals of the Rheumatic Diseases*, 56(5): 308–312, 1997.

Renström P. and Hach T.: *Insertional tendinopathy in sports*. 2005.

Tétreault P., Krueger A., Zurakowski D., and Gerber C.: Glenoid version and rotator cuff tears. *J Orthop Res*, 22:202–207, 2004.

van der Helm F. C. T. and Veenbaas R.: Modelling the mechanical effect of muscles with large attachment sites: Application to the shoulder mechanism. *Journal of Biomechanics*, 24(12): 1151–1163, 1991.

Wong A. S., Gallo L., Kuhn J. E., Carpenter J. E., and Hughes R. E.: The effect of glenoid inclination on superior humeral head migration. *J Shoulder Elbow Surg*, 12:360–364, 2003.

Christoph Engelhardt

Rue Madeleine 2
1003 Lausanne
Switzerland
☎ *+41 77 44 95 800*
⊠ *christoph.engelhardt@gmx.net*
born 13.01.1984 in Mainz, Germany
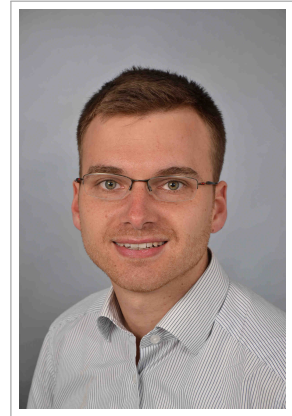
Studies

2011 – 2015   **Doctoral Studies**
Ecole Polytechnique Fédérale de Lausanne (EPFL), Lausanne, Switzerland.

PhD Thesis
"Effect of Anatomic Parameters on Degenerative Shoulder Diseases",
Prof. Dominique Pioletti, Laboratory of Biomechanical Orthopedics.

2004 – 2010   **Studies in Mechanical Engineering**
Karlsruhe Institute of Technology (KIT), Karlsruhe, Germany.
- ▶ major studies in product development and computational mechanics.
- ▶ participation in industrial product development projects

Diploma Thesis
"Microstructural Modelling of Shortfibre Reinforced Composites with Fibreclusters and Their Influence on the Effective Elastic Properties",
Prof. Thomas Böhlke, Institute of Engineering Mechanics, Chair for Continuum Mechanics.

Intermediate Diploma Thesis
"Development of a Tractor Accessory to Produce High Quality Wood Chips out of Wine Pruning",
Prof. Marcus Geimer, Institute for Automotive System Technology, Chair for Mobile Machinery.

2003   **School Leaving Examination**
Bischöfliches Willigis Gymnasium, Mainz.

Scientific Publications

2013   Ingram D., Engelhardt C., Farron A., Terrier A. and Muellhaupt P.: Moment Arms - A Key Element In Muscle Force Estimation., Journal of Computer Methods in Biomechanics and Biomedical Engineering, 2013, 18(5), 506-513.

2014   Engelhardt C., Camine V. M., Ingram D., Muellhaupt P., Farron A., Pioletti D. P. and Terrier A.: Comparison of an EMG-based and a stress-based method to predict shoulder muscle forces, Computer Methods in Biomechanics and Biomedical Engineering, 2015, 18, 1272-1279.

2015   Engelhardt C., Ingram D., Müllhaupt P., Farron A., Becce F., Pioletti D. P. and Terrier A.: Effect of Partial-Thickness Tear on Loading Capacities of the Supraspinatus Tendon: A Finite Element Analysis, Computer Methods in Biomechanics and Biomedical Engineering, accepted for publication.

2015   Ingram D., Engelhardt C., Farron A., Terrier A., Müllhaupt P.: Improving Anterior Deltoid Activity in a Musculoskeletal Shoulder Model, Computer Methods in Biomechanics and Biomechanical Engineering, accepted for publication.

Working Experience

2011 – 2015 **Research Associate**
Laboratory of Biomechanical Orthopedics, Lausanne, Switzerland.
- ▶ numerical modelling of the shoulder to investigate muscle coordination
- ▶ finite element analysis of biological soft tissues
- ▶ publication of results in international peer reviewed journals
- ▶ participation and presentation of the work on international conferences
- ▶ teaching assistance and supervision of master projects
- ▶ setup and maintenance of the laboratories IT infrastructure

2008 – 2010 **Student Assistant**
Institute for Engineering Mechanics, Chair for Continuum Mechanics, Karlsruhe, Germany.
- ▶ research in the field of the numerical modelling of short fibre reinforced composites
- ▶ teaching assistance in the introductory course on finite element methods
- ▶ supervising master students during practical works with Abaqus and Matlab

2007 – 2008 **Industry Internship**
Nief Plastique, Genas, France.
- ▶ internship in research and development department
- ▶ autonomous realization of CAD projects on injection die-cast parts

2006 – 2007 **Student Assistant**
Institute for Production Technology, Karlsruhe, Germany.
- ▶ research and development projects to improve the ease of maintenance of machine tools
- ▶ in cooperation with KSB in Pegnitz, Germany

2004 **Industry Internships**
SCHOTT AG, Mainz, Germany, and Römheld & Mölle, Mainz, Germany.

Social Activities

2000 – 2011 **Youth Leader and Instructor**
German Alpine Club DAV, Mainz and Karlsruhe, Germany.
- ▶ training of youth groups in sport climbing and mountaineering
- ▶ yearly education in mountaineering-specific topics and leadership competences
- ▶ planning and organising weekly meetings and holiday camps

2003 – 2004 **Civil Service**
German Red Cross Rescue Service, Mainz, Germany.
- ▶ training and service as a paramedic in the ambulance rescue service

Languages

German	native speaker
English	professional competences
French	professional competences
Chinese	beginner

IT Skills

Systems	administration of servers and workstations running under Windows and Linux
Software	Office, Latex, Matlab, Catia V5, Solidworks, Amira, Geomagic, Abaqus, Ansys, Comsol
Programing	C/C++, Fortran, Python, TCL, Bash

Personal Interest

Sports	hiking, skiing, paragliding, running
Music	playing guitar
Others	aeroplane model construction and flying, cooking, DIY